Master Thesis in Geosciences

Modelling of permafrost in Norway using two equilibrium models

Kjersti Gisnås

UNIVERSITY OF OSLO

FACULTY OF MATHEMATICS AND NATURAL SCIENCES

Modelling of permafrost in Norway using two equilibrium models

Master in Geosciences

Kjersti Gisnås

Thesis submitted in fulfillment of the requirements for the Degree of Master of Physical Geography, Geomatics and Hydrology

Department of Geosciences

University of Oslo

Blindern, Norway

01.06.2011

Title: ***Modelling of permafrost in Norway using two equilibrium models.***

Author: **Kjersti Gisnås.**

Supervisor(s): **Bernd Etzelmüller (UiO) – Thomas Vikhamar Schuler (UiO) – Chris Burn (Carleton University)**

Front page: “Juvvass” by Tobias F. Hipp.

This work is published digitally through DUO – Digitale Utgivelser ved UiO

http://www.duo.uio.no

It is also catalogued in BIBSYS (http://www.bibsys.no/english)

Abstract

The thermal regime of permafrost is likely to change significantly in response to the predicted climate warming. Degradation of permafrost may lead to destabilization of rock faces and steep slopes, and changes in surface hydrology. Knowledge about the spatial distribution and temperatures of permafrost is crucial to understand the associated geomorphological processes. In this study permafrost distribution is modelled on regional scale for mainland Norway, at 1km^2 resolution. Two equilibrium models developed for low-land Arctic permafrost are adjusted for Norway. This is the first time ground temperatures have been modelled on regional scale for Norway, by taking subsurface material-, vegetation- and snow cover properties into account. The models are forced with daily gridded air temperature, snow depth and snow water equivalent data for the period 1957 to 2010. The model results for 1981-2010 are in very good accordance with observed ground temperatures from boreholes and permafrost distribution in BTS-probability maps. This study demonstrates that such models are very applicable also for mountainous environments. Reconstructed air temperature series back to 10 000 B.P. were used to model historical permafrost distributions, with special emphasis on the Little Ice Age and Holocene Climatic Optimum. According to the model results approximately 6% of the total mainland area in Norway is presently underlain by permafrost. Estimated permafrost occurrence for the Little Ice Age is 15% , while permafrost survived Holocene Climatic Optimum in 1% of mainland Norway. In future simulations permafrost will be nearly absent (0.2%) with the predicted climate for 2071-2100 given the chosen A2 scenario.

Acknowledgements

The research presented in this thesis has been carried out at the department of Geosciences at the University of Oslo. The research work has been a part of the CRYOLINK project, with the goal of understanding and modelling the atmosphere-ground temperature regime in southern Norway. The work in this thesis has been done in cooperation with several people at the department.

In particular, I wish to express my gratitude to my main supervisor, Professor Bernd Etzelmüller for his continued encouragement, invaluable suggestions, erratic enthusiasm, extremely fast e-mail replies, somewhat refined sarcasm, and for including me on nice trips, fancy dinners and beer nights with the "big guys"! I would also like to include my gratitude to my co-supervisors, Thomas V. Schuler and Chris Burn. Thank you, Thomas for sharing your extensive MATLAB skills, and Chris for giving me a different perspective to my research.

Furthermore I want to thank my outstanding field assistants Tobias "bbq-king" Hipp and Sebastian Westermann for a great trip, with outstanding food and lots of fun. Tobias, you're shining like the sun in all kind of weather – awesome! And Sebastian, thank's for putting me together when I'm falling apart, and heal my wounds with old krembolle;) See you in Bakeriet in Lom!

I will also thank Herman Farbrot for great help with all sorts of field data, for hilarious e-mails, for making me believe I'm a MATLAB genius, and not at least; for an *unvergesslich* Kaizers concert in Vienna! Furthermore I would like to thank Karianne Lilleøren for interesting discussions about permafrost, rock glaciers and bowl fires, for giving me great support at EGU, introducing me to kleptomania, and best of all; to conference cigarettes!

Graham Gilbert, you deserve a chapter all by your self! This chapter is the only one you haven't corrected in this thesis, and thank's to you the thesis actually sounds quite scientific, and not like a drunken rant ;) I can't thank you enough!

Sebastian, thank's for help great with the thesis! Your feedback was invaluable, both for the quality of the thesis and for my personal understanding and knowledge.

Rune and Tobias; you are my two favorite MATLAB nerds! Your great help with the GUI, and in general any time me an MATLAB were not friends, is the reason why I still love this program deeply ;)...also thank's for all sarcastic comments from behind my back Rune, for lots of good coffee, and Tobi; for great company at the computer lab every single night during the last weeks of my master thesis work!

I would also thank Åse Manengen for always showing so much interest for my work; often more than I have myself! Thank's for great trips to Finnmark and Svalbard, and for brighten up my masterlife with several good breaks!

A special thought is devoted to my parents for a never-ending support!

Table of contents

1. Introduction 1

1.1 Permafrost - the global perspective 1

1.2 Previous permafrost mapping in Norway 2

1.3 Objectives 4

1.4 Thesis structure 5

2. Theoretical background 7

2.1 The climate – permafrost relationship 7

2.2 Mountain permafrost 8

2.2.1 Block fields 10

2.3 Permafrost modelling 12

2.3.1 Heat conduction theory 14

2.3.2 The Stefan Solution 14

2.3.3 The TTOP-model 16

2.3.4 Kudryavtsev's approach 20

3. Area of study 25

3.1 Geographical setting 25

3.2 Climate setting 27

3.3 Permafrost in Norway 29

4. Methodology 30

4.1 Input data 31

4.1.1 Meteorological data 31

4.1.2 Vegetation 34

4.1.3 Blockfield map 34

4.1.4 Subsurface material property data 36

4.2 The surface offset 39

4.2.1 Parameterization of *n*-factors - CryoGRID-ttop 39
4.2.2 Thermal effects of snow and surface vegetation cover – CryoGRID-mKA 43
4.3 The thermal offset 45
4.3.1 Parameterizing of soil property data 46
5. Model results 49
5.1 Present permafrost distribution in Norway 49
5.2 Active layer thickness and permafrost depth 54
6. Model evaluation and sensitivity 56
6.1 Evaluation of *MAGST* 56
6.1.1 MTD-loggers 56
6.2 Evaluation of *MAGT* 56
6.2.1 Borehole data 56
6.2.2 BTS-maps 58
6.2.3 Distribution of palsas, rock glaciers and ice cored moraines 62
6.3 Model sensitivity 62
6.3.1 Sensitivity to snow cover 62
6.3.2 Sensitivity in *MAGT* due to surface cover 64
6.3.3 Sensitivity to r_k 68
7. Examples of the application of CryoGRIDeq to past and future climate conditions 70
7.1 Holocene permafrost in Norway 70
7.2 Future permafrost in Norway 71
8. Discussion 75
8.1 Input data 75
8.1.1 The SeNorge-data 75
8.1.2 Block field map 77
8.1.3 Geological and vegetation maps 78
8.2 Parameterization and *n*-factors 79

8.2.1 *n*-factors 79
8.2.2 Thermal conductivity in the ground 81
8.2.3 Parameterization of blockfields 84
8.3 Evaluation of the CryoGRIDeq- models 86
8.3.1 Boreholes 86
8.3.2 BTS-evaluation 87
8.3.3 Rock glaciers, ice-cored moraines and palsas 88
8.4 TTOP vs. mKA 89
8.5 Subgrid variability 91
8.6 Present permafrost distribution in Norway 95
8.7 Scenarios – implications for future 95
9. Conclusions 98
10. References 101
11. Appendix contents I

List of Figures

Figure 1: Circum-polar permafrost distribution classified in continuous, discontinuous and isolated patches of permafrost occurrence (UNEP/GRID-Arendal 2007). The map is based on data from IPA (Brown et al. 1997) Norway, the area of study, is marked with a red circle. 1
Figure 2: The workflow of this thesis. 6
Figure 3: Vertical transect of idealized ground temperatures. Modified from Riseborough (2004). 8
Figure 4: The image shows the borehole, air/ground station and i-button installation at the top of Juvvass (Juv-BH1). The station is installed in a blockfield consisting of relatively small blocks with no vegetation cover. 10
Figure 5: Vertical transect of the atmosphere-ground relationship, divided into three layers. Modified from Riseborough (2004). 16
Figure 6: The modified Kudryavtsev's approach treats the thermal regime from atmosphere to ground as a system of different layer. The surface offset consists of a buffer layer including vegetation and snow cover, and soil organic horizon. 21
Figure 8: Left: Palsa mire in flat tundra-like landscape in Finnmark. Foto: Åse Manengen. Right: Alpine mountains in Jotunheimen. 26
Figure 7: Topographical map for mainland Norway, showing the Scandinavian mountain range reaching from southern to northern Norway. The range is a clear divide between the west coast and the more continental eastern parts of Norway (UNEP/GRID-Arendal 2001). 26
Figure 9: Precipitation (left) and air temperature (right) maps for last normal period in Norway, provided by SeNorge. 28
Figure 10: Left: mean annual maximum snow amount for last normal period (senorge.no 2010). Right: Köppens climate classification for Norway (met.no 2010c). 28
Figure 11: Flow chart for the TTOP-model implementation. 32
Figure 12: Flow chart showing the mKA-model implementation. 33
Figure 13: Average thermal conductivity values and variation within each class (Angst 2010). 37
Figure 14: Input data: a) CORINE 2000 vegetation map reclassified, b) blockfield map produced from Landsat TM-images, c) bedrock density and d) bedrock thermal conductivity derived from NGU petrophysical data. 38
Figure 15: CRYOLINK field installations. 41
Figure 16: Correlation of nF-factors and seasonal mean snow water equivalent measured at the CRYOLINK air/ground and i-button stations. The trendline is y = 0.72 - 0.16ln(x). 42

Figure 17: Permafrost distribution in Norway over the normal period 1981-2010, modelled with CryoGRID-ttop. Mean annual ground temperatures (MAGT) below zero degrees centigrade are given in blue colors, and indicate permafrost areas. Red colors are used for non-permafrost areas. The green color shows areas of mires with MAGT below zeros; these are areas of potential palsa mires. 51
Figure 18: Maps showing permafrost at the CRYOLINK key sites modelled with the TTOP-model (left) and the mKA-model (right). Legend is equivalent to Figure 17.....52
Figure 19: West - east transects showing permafrost occurrence distributed on elevation and distance from the west coast. Upper transect shows Jotunheimen including Glittertind and Galdhøpiggen, and crosses over Ringebufjellet towards east. The lower transect crosses inner parts of Troms and Finnmarksvidda. 53
Figure 20: MAGST (a and b), ALT (c and d) and permafrost depth (e and f) modelled with the TTOP-model for a chosen area in Troms and Finnmark (left) and central southern Norway (right). 55
Figure 21: TTOP (left) and mKA (right) MAGT values compared to BTS probability maps based on BTS measurements published earlier in Isaksen et al. (2002) and Heggem et al. (2005) for selected sites in southern Norway. Juvvass: a and b. Dovre: c and d. Elgåhogna: e and f. Sølen: g and h. Only areas with MAGT below 0°C are included.....60
Figure 22: Scatter plots for measured and modelled MAGST. Measured values are based on 74 MTD-loggers, and are plotted along the x-axis. Modelled values are plotted on the y-axis, for the TTOP-model in the left plot (a) and for the mKA-model to the right (b).....61
Figure 23: Left: Distribution of potential palsa mires modelled with the TTOP-model for 1981-2010. Right: Mapped palsa bogs based on several studies both at UiO (Sollid and Sørbel 1974, Sollid and Sørbel 1998)and NINA, Norsk institutt for naturforskning (Hofgaard 2003). 61
Figure 24: The permafrost map for southern Norway compared to mapped intact and relict permafrost landforms, including rock glaciers and ice cored moraines. 63
Figure 25: The correlation between intact rock glaciers/ice cored moraines and permafrost is very good for all areas of such landforms in southern Norway; a) Romsdalen, b)Dovre, c) Jotunheimen, and d) Rondane. The colorbar is the same as in Figure 24.....63
Figure 26: Sensitivity of MAGT in relation to snow depth and continentality. The graph shows the deviation in MAGT due to a 20 cm uncertainty in annual mean snow depth.....64
Figure 27: The figure shows the variation of n-factors in each surface class. The central mark is the median, and the edges of the boxes are the 25th and 75th percentiles. The whiskers

extend to the most extreme data points the algorithms considers not to be outliers. Outliers are plotted individually. 67
Figure 28: Sensitivity of MAGT due to change in rk when nT = 1 (hard lines) and nT = 0.85 (dotted lines). Dark colors are sensitivity in continental areas with 1000 TDD. Light grey line shows sensitivity when TDD = 580 °C day year^{-1}. 69
Figure 29: Relation between maximum snow water equivalent and freezing n-factors. The trend line is y = 1,026 - 0,213ln(x). 73
Figure 30: Paleo reconstruction of previous permafrost distributions in southern Norway during Holocene. 73
Figure 31: MAGT modelled with the TTOP-model for the future scenario 2071-2100, based on downscaled IPCC emission scenario A2 temperatures and maxSWE. 74
Figure 32: Meteorological stations distributed on height above sea level. TM is temperature stations, RR is precipitation stations. The brown line indicates the altitudinal distribution of topography (Tveito 2009). 77
Figure 33: nF-snow depth relation developed from CRYOLINK i-button and air/ground stations. IX
Figure 34: nF-snow depth relation developed from numerical simulations by Smith and Riseborough(2002). IX
Figure 35: The plots show the difference in MAGT between the two models distributed on altitude. Each surface cover class is plotted individually. XIII
Figure 36: Difference in MAGT between the two models is distributed on altitude and subsurface material class. The plots are numbered with respect to subsurface material classes from Table 4. XV

List of Tables

Table 1: Cross-referance table for the validation of the blockfield classification shown in Appendix C.3. 35
Table 2: n-factor parameterization used in the CryoGRID-TTOP model. 42
Table 3: Thermal diffusivity and height related to the different vegetation classes in the CORINE2000 vegetation map. The data are provided by the Geophysical Institute in Fairbanks. 45
Table 4: Heat capacity and thermal conductivity values in thawed and frozen ground, in addition to volumetric water content of the ground are assigned to the different subsurface material classes in the NGU-map. 47
Table 5: Distribution of permafrost presented as a fraction of total area, and subsurface material classes expressed as a fraction of total permafrost area. Values are based on the TTOP-model run for 1981-2010 (Figure 17). 50
Table 6: Measured and modelled MAGT from the two models for all TSP and CRYOLINK boreholes in Norway are shown in the table below. The difference in temperature is shown in the two right columns. 57
Table 7: The table shows ΔMAGT between vegetation classes in a) a continental climate, and b) a maritime climate. r_k within each class is fixed, and snow depth and degree days are fixed within each climatic setting. Sensitivity to vegetation classes increases with continentality, and the classes of highest sensitivity varies much from continental to maritime setting. 65
Table 8: Average n-factors (Avg) for each surface class based on air/ground stations (upper) and MTD-logger (lower) are given in the table below. Std is the standard deviation in nT/nF within each surface class. 67
Table 9: Uncertainty of MAGT temperatures due to inter-class variation in n-factors. 68
Table 10: Climate adjustments for the little ice age and Holocene maximum based on Lilleøren et al. (in prep). 71
Table 11: nF-factors related to descretized maxSWE, based on the relationship in Figure 29. 72
Table 12: Conductivity values applied in the TONE-model. 82
Table 13: The table shows the r_k-values at each borehole estimated with the TTOP-model from borehole data, a 1D-model and the CryoGRID-models. 83
Table 14: Data from the six CRYOLINK-sites located in blockfields, measuring air and ground surface temperatures, in addition to mean seasonal snow depth. 85

Table 15: The table shows permafrost occurrence during LIA and today distributed on subsurface material type. 96
Table 16: Area underlain by permafrost in Holocene Climatic Optimum and 2071-2100 distributed on subsurface material type. Values are km^2 area of permafrost.....97
Table 17: Average snow densities and snow depths measured during the CRYOLINK foeld work 4th to 7th of March 2011. The data are used to relate nF-factors to snow water equivalent.....X

List of variables and constants

Variables	Notation	Units
Freezing degree days	FDD	°Cyr^{-1}
Thawing degree days	TDD	°Cyr^{-1}
Annual air temperature amplitude	Aa	°C
Annual mean air temperature	$AMAT$	°C
Correction to Aa accounting for snow cover/vegetation effect	$\Delta A_{sn/v}$	°C
Correction to Ta accounting for snow cover/vegetation effect	$\Delta T_{sn/v}$	°C
Mean annual ground surface temperature	$MAGST$	°C
Mean annual ground temperature	$MAGT$	°C
Annual mean snow depth	$AMSD$	m
Thermal offset	ΔT_k	°C
Active layer thickness/seasonal frost depth	Z_{al}	m
Surface thawing n-factor	nT	
Surface freezing n-factor	nF	
Ratio of conductivities in thawed and frozen ground (K_t/K_f)	r_k	
Depth	z	m
Temperature	T	°C
time step	t	
Volumetric heat capacity	C	Jm^{-3} K^{-1}
Volumetric heat capacity in thawed/frozen state	$C_{t/f}$	Jm^{-3}K^{-1}
Volumetric heat capacity of snow cover	C_{sn}	Jm^{-3}K^{-1}
Volumetric effective heat capacity	C_{eff}	Jm^{-3}K^{-1}
Specific heat capacity	c	Jkg^{-1}K^{-1}
Thermal conductivity of the ground	K	Wm^{-1}K^{-1}
Thermal conductivity in thawed ground	K_t	Wm^{-1}K^{-1}
Thermal conductivity in frozen ground	K_f	Wm^{-1}K^{-1}
Thermal conductivity of snow cover	K_{sn}	Wm^{-1}K^{-1}
Volumetric water content in the ground	θ_w	fraction of 1
Volumetric unfrozen water content in the ground	θ_u	fraction of 1
Density	ρ	kg m^{-3}
Density of snow cover	ρ_{sn}	kg m^{-3}
Height of vegetation cover	H_v	m
Seasonal average snow depth	H_{sn}	m
Thermal diffusivity of vegetation in thawed/frozen state	D_{vt}/ D_{vf}	m^{2}s^{-1}
Volumetric latent heat of fusion	L	Jm^{-3}
Period of temperature wave	τ	s
Scaling factor, 86400 (from days to seconds)	S	
Air/ground surface/permafrost surface	*a/gs/ps*	
Snow	*sn*	
Vegetation	*v*	
Water	*w*	
Thawing/freezing	*t/f*	

1. Introduction

1.1 Permafrost - the global perspective

Permafrost is defined as ground that remains at or below 0°C for at least two consecutive years (French 2007). 24% of the land surface area of the northern hemisphere is occupied by permafrost (Zhang et al. 2000), whereas the largest extents are found in Siberia, Canada and Alaska (French 2007). Permafrost does mainly occur in arctic regions as latitudinal permafrost, but can also be found at high altitudes as mountain permafrost, such as in the Alps and in the Scandinavian mountains. This study investigates the distribution of permafrost in Norway, situated in the continuous to discontinuous permafrost zone (Figure 1).

Figure 1: Circum-polar permafrost distribution classified in continuous, discontinuous and isolated patches of permafrost occurrence (UNEP/GRID-Arendal 2007). The map is based on data from IPA (Brown et al. 1997). Norway, the area of study, is marked with a red circle.

During the last decades a large number of studies have shown evidences of a substantial global warming, with the most pronounced increase in Arctic areas (Hanssen-Bauer and Førland 1998, Førland and Hanssen-Bauer 2003, Hinzman et al. 2005, Comiso et al. 2008,

Overland et al. 2008). As a result there are reported evidence for warming permafrost temperatures and thickening of the active layer in many regions (Romanovsky and Osterkamp 1997, Osterkamp 2005), including the Nordic area (Isaksen et al. 2001, Harris et al. 2003, Isaksen et al. 2007, Christiansen et al. 2010).

An accelerated future warming trend is predicted by general circulation models (GCMs), and the Intergovernmental Panel on Climate Change (*IPCC*) projects that the global air temperature is likely to rise by 1.1 – 6.4°C during the next century (IPCC 2007), with the highest increase in Arctic and sub-Arctic areas (Kattsov and Källén 2005). As a result, active layer depth is expected to increase and the spatial distribution of permafrost to decrease (Nicolsky et al. 2007, Lawrence et al. 2008, Zhang et al. 2008a). Results from a 1D heat flow model applied at 13 borehole sites in Norway projects a substantial warming of permafrost at all sites until 2100, resulting in talik development and a upward shift in the lower limit of permafrost of 200 meters or more (Hipp et al. 2011).

Permafrost has an influence on geomorphological processes (e.g.Berthling and Etzelmüller 2011) and on geotechnical properties of the ground (Haeberli 1992, Gruber et al. 2004). There has lately been an increased focus on the connection between destabilization of steep rock slopes and warming of discontinuous permafrost in high-relief mountain areas (Gruber et al. 2004, Isaksen et al. 2011). Because ground temperatures are close to 0°C in these areas, permafrost is particularly vulnerable to climate perturbations. Furthermore, permafrost plays a primary role in the cryosphere through its influence on energy exchanges, carbon budgets and hydrology, and thereby also the global climate system. Ground temperatures modulate the decomposition of organic material and in turn the release of greenhouse gasses (GHG). About one half of the world's total soil carbon stock and twice the atmospheric carbon pool is stored in the upper 3 meters of the permafrost (Schuur et al. 2008). An increase in active layer thickness and a degradation of permafrost will thaw large amounts of previously frozen material that has been accumulated over millennia, resulting in a massive release of methane. Thus, knowledge of the spatial distribution of ground thermal regime and the age of permafrost is essential to understand past, present and future permafrost dynamics in Norway.

1.2 Previous permafrost mapping in Norway

Early in the 20th century Reusch (1902) suggested that permafrost was present in the Scandinavian mountains. However, direct evidence for the thickness of permafrost was not

obtained until 1941 when a 70 meter thick layer of permafrost was found during drilling in the Abisko region, Northern Sweden (Ekman 1957). Beginning in the 1980s, geophysical methods provided evidence of extensive permafrost to depths of 50 meters in both Sweden and Norway (King 1986). During the International Polar Year (IPY) large monitoring campaigns was initiated in Norway (Christiansen et al. 2010). The TSP Norway "Permafrost Observatory Project: A Contribution to the Thermal State of Permafrost in Norway and Svalbard" had field campaigns in Troms and Finnmark, northern Norway. 25 new boreholes was established, where 13 was in permafrost. As a contribution to the monitoring in southern Norway, the CRYOLINK project (Permafrost and seasonal frost in Southern Norway: understanding and modelling the atmosphere-ground temperature) was initiated in august 2008. Three new altitudinal borehole transects, with a total number of 13 boreholes was drilled. In addition a high number of ground surface temperature loggers and stations measuring air and ground surface temperatures and snow depth were installed.

Recently, several new methods for monitoring and mapping mountain permafrost in Europe have been developed by the European Union PACE Project (Permafrost and Climate in Europe) (Harris et al. 2001b). These geotechnical and geophysical methods were subsequently used to map and monitor the permafrost in Europe (Hauck et al. 2000, Isaksen et al. 2001, Isaksen et al. 2002, Vonder Muhll et al. 2002, Hauck et al. 2004). Prior to this, mapping of permafrost on regional scale (>100m) was by empirical-statistical models, where permafrost occurrence from BTS measurements (basal temperature of snow cover, (Haeberli 1973)) were related to topoclimatic factors such as elevation and mean annual air temperature (*MAAT*) (Etzelmüller et al. 1998, Etzelmüller et al. 2001a, Etzelmüller et al. 2001b, Isaksen et al. 2002, Heggem et al. 2005). These approaches included only a limited number of parameters (*MAAT*/elevation) and provided only an indication of the presence or absence of permafrost. More sophisticated permafrost modeling approaches (e.g.Nelson and Outcalt 1987, Smith and Riseborough 1996, Stendel and Christensen 2002, Sazonova and Romanovsky 2003, Sushama et al. 2006, Lawrence et al. 2008, Zhang et al. 2008b) have yet not been applied on large spatial scales in Norway. Juliussen et al. (2007) tested an equilibrium model for two mountains in Femundsmarka, southern Norway. The equilibrium model (the TTOP-model,) was originally developed for an Arctic lowland environment with a homogeneous topography (Smith and Riseborough 1996). In contrast, the mountain permafrost in Norway is situated in more heterogeneous topography, and therefore has a larger variation in the surface micro-climate (Riseborough et al. 2008). Juliussen et al.

concluded that the TTOP-model has potential for mapping of mountain permafrost, but requires adjustments for specific areas of study.

1.3 Objectives

The purpose of this project is to quantify the distribution and temperature of permafrost in Norway at a regional scale. The basic hypothesis of this research is that the equilibrium models initially developed for low-land Arctic permafrost are also applicable in mountainous terrain such as is present in Scandinavia. This hypothesis is supported by the fact the Scandinavian mountains are dominated by paleic surfaces and more gentle slopes in relation to e.g. the Alps (Etzelmüller and Frauenfelder 2009), and therefore topographic-derived heterogeneities may have a lower importance. We addressed this hypothesis by:

1) developing *n*-factors adapted for mountain permafrost (Chapter 4.2.1).
2) producing a map of blockfield distribution in Norway, based on classification of Landsat images (Chapter 4.1.3).
3) producing a map (1 km^2) of the conductivity ratio of the ground in frozen and thawed states (Chapter 4.1.4).
4) implementation of two already established equilibrium models; the TTOP-model and the mKA-model, for mainland Norway with 1 km^2 resolution (Chapter 4).
5) modify the models to deal with the convective heat exchange in blockfield areas (Chapter 4.2.1 and 4.3.1).

The models are evaluated for sensitivity and ability to reproduce mountain permafrost. The models will be run for four different scenarios; the Holocene Climatic Optimum and the Little Ice Age with reconstructed air temperature series from Lilleøren (in prep), last normal period (1981-2010) and an equilibrium situation for 2071-2100 with air temperatures projected in the IPCC A2 emission scenario. The relative ages of the permafrost is analyzed in connection to areas vulnerable for climate warming. Analysis of ground thermal response to historical and future air temperature variation have recently been done by 1D modelling for 13 borehole locations in Norway (Hipp et al. 2011). The spatially distribution scenarios presented in this thesis are a new step towards a better understanding of the ground thermal responses to climate change. This understanding is of importance for geomorphological process patters and landscape development (Etzelmüller et al. 2003, Etzelmüller 2011).

1.4 Thesis structure

This thesis describes the implementation of permafrost equilibrium models for mainland Norway. Chapter 2 introduces the processes that determine the ground thermal regime, and provides a theoretical description of mountain permafrost, which is the permafrost type of particular importance for Norway. The last part of Chapter 2 contains an overview of the two models implemented in this study. Chapter 3 gives an overview of climatic, geographic and permafrost setting for Norway.

The basic workflow of this thesis starts at Chapter 4 with a description of input data and parameterization. An overview of the general workflow is given in Figure 2. The complete model run with a user interface is included in Appendix F. A new blockfield map for Norway has been produced and Chapter 4.1 contains a brief description of this classification routine. Validation, in addition to the model run is included in Appendix C.

Model results containing spatially distributed mean annual ground temperatures, mean annual ground surface temperatures, active layer depths and permafrost depths for mainland Norway are presented in Chapter 5. An extensive list of maps is included in Appendix E. The results are evaluated with observed ground temperature data from boreholes, ground surface temperatures from data loggers, BTS-maps and maps of permafrost landforms. This evaluation is presented in the first part of Chapter 6, while the sensitivity of the TTOP-model is examined in Chapter 6.3.

The models are forced with reconstructed climatic data series back to 10 000 B.P. with 250 years intervals. The model runs for the Little Ice Age and Holocene Climatic Optimum are presented in Chapter 7.1. The models are also run for a future scenario for 2071-2100, based on the SRES A2 emission scenario. These results are presented in Chapter 7.2. A discussion of the model performance and further implications of the results are given in Chapter 8.

Abstracts, poster and oral presentation from publications at two conferences, respectively EUCOP2010 and EGU2011, are included in Appendix A. Appendix A, and C to F are included on a CD attached to the thesis.

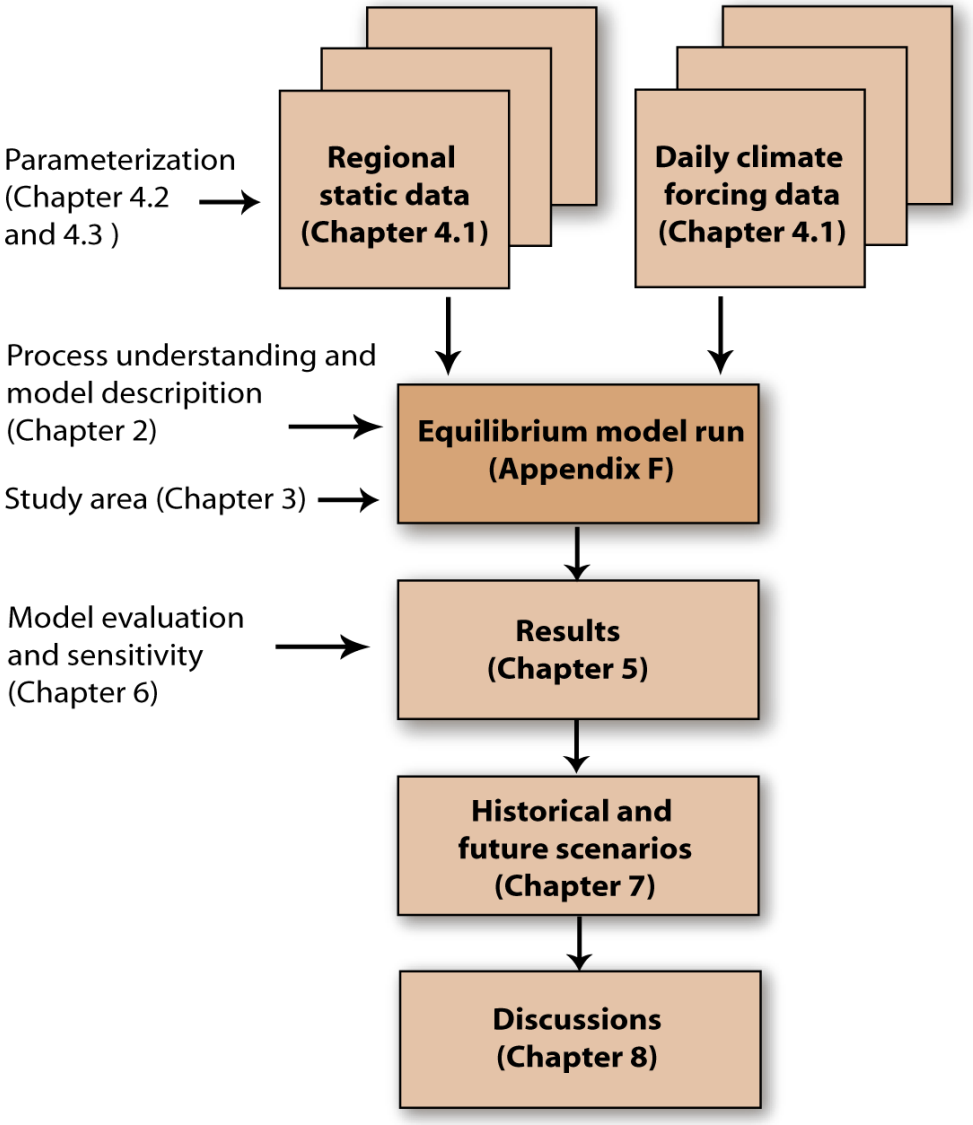

Figure 2: The workflow of this thesis.

2. Theoretical background

2.1 The climate – permafrost relationship

Ground temperatures are a result of atmospheric processes, terrain, thermal properties of the ground, and the geothermal heat flux. The annual variation of air temperature may be generalized to a sine curve, where the amplitude and period varies with latitude, climatic setting (e.g. maritime or continental) and large-scale topography. The annual temperature amplitude at the ground surface may be damped compared to the air, due to shading and evaporation in summer, and effects of snow cover in winter (Figure 3). The difference between air and ground surface temperatures is called the surface offset.

Deeper in the ground, the temperature amplitude is further damped, depending on the thermal diffusivity of the ground material. The depth where the annual temperature variation is negligible is "the depth of zero annual amplitude". The top of permafrost, called the permafrost table, is where the ground remains at or below 0°C for two or more consecutive years. The active layer is the ground above permafrost that thaws and refreezes annually. Normally, mean annual temperature decreases with depth in the active layer due to different conductivities of the ground material in frozen and thawed states. This difference is related to the subsurface material water content, since the thermal conductivity of ice is approximately four times higher than that of water. The temperature difference between the ground surface and mean annual ground temperature (*MAGT*) is called the thermal offset.

Below the depth of zero annual amplitude the ground temperature increases due to the geothermal heat flow when the system is in equilibrium. The base of permafrost is identified by the depth at which the temperature of the ground again warms above 0°C, illustrated in Figure 3.

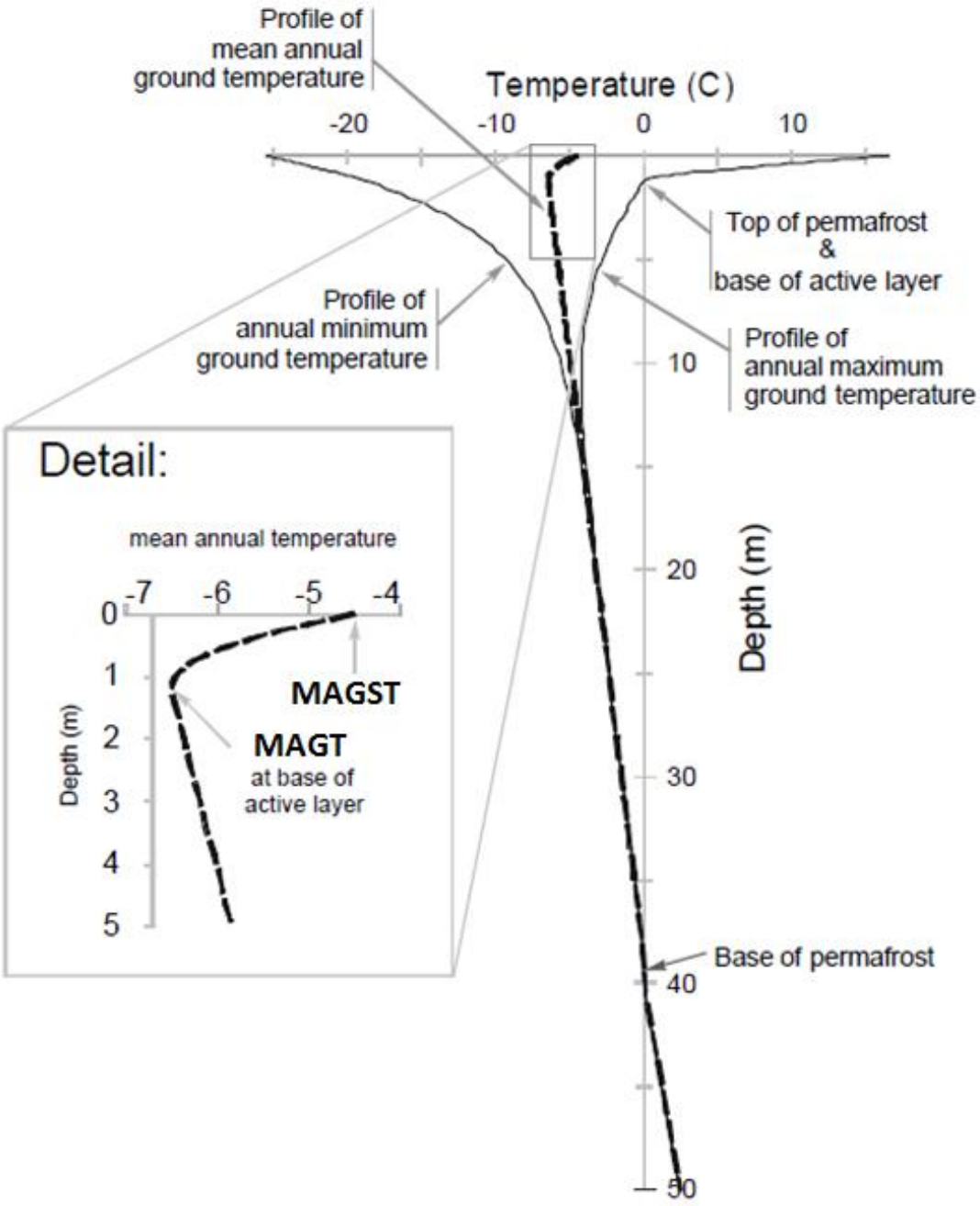

Figure 3: Vertical transect of idealized ground temperatures. Modified from Riseborough (2004).

2.2 Mountain permafrost

Mountain permafrost, simply defined as permafrost in mountainous areas, results from the influence of mountain topography on the factors governing the ground thermal regime (Haeberli et al. 1993). The dominating characteristic of alpine permafrost is the extreme

spatial variability, resulting from variance in topography, elevation, slope, aspect, curvature and roughness. Variation in these factors results in significant variability in the surface micro-climate due to changes in long-wave radiation, short-wave radiation and turbulent fluxes (Gubler et al. 2011, Hasler et al. 2011). Furthermore, there is commonly a large variation in subsurface material composition and thickness – influencing the ground's thermal properties. Spatial variability is also observed in water availability, affected by contributing area, subsurface material and surface shape. Mountain areas drain quickly; hence the subsurface material moisture content is commonly lower in alpine environments than in the Arctic lowlands. Variation in snow cover further serves to characterize alpine environments and occurs in response to variable surface micro-climates, precipitation patterns, wind drift and snow avalanches (Gruber and Haeberli 2009). Measurements in mountain areas are also both logistically difficult and expensive; hence the amount of data available is often sparse (Gruber and Haeberli 2009). Significant variability in ground thermal regimes combined with the great expenses and difficulties of obtaining field measurements makes mapping of mountain permafrost inherently problematic.

The relevance of mountain permafrost is partially derived from the effect it has on sediment-transport mechanisms. The physical stability of steep mountain sides is highly sensitive to thermal changes, as thawing reduces the strength of both ice-rich sediment and frost-jointed bedrock (Davies et al. 2001, Gruber and Haeberli 2007). Ice-rich permafrost undergoes thaw consolidation during thawing, leading to increased pore-water pressure and instability (Harris et al. 2001a). Warming of bedrock slopes can reduce the strength of ice-bonded joints and can also lead to increased groundwater movement resulting in a rise in pore-water pressure. Both of these effects result in the destabilization of slopes (Harris et al. 2001a). Since the permafrost temperatures in most parts of Norway are only a few degrees below 0°C, a slight increase in surface temperatures may lead to widespread degradation of permafrost and correspondingly am increase the magnitude and frequency of natural hazards such as rock avalanches and debris flows (Haeberli 1992, Haeberli et al. 1993, Haeberli et al. 1997, Isaksen 2007, Gruber and Haeberli 2009). The impact of such mass wasting events is frequently amplified in Norway due to the tsunami effect generated by rock falls and avalanches into narrow fjords. These waves may rise up to 62 meters above sea level, and during the last 100 years 170 people have been killed by tsunamis generated by rock avalanches (Braathen et al. 2004, Blikra et al. 2005). Recent studies indicate a relationship

between the ground thermal regime and the stability of these avalanche prone rock walls in the Norwegian mountains, particularly in northern Norway (Isaksen et al. 2011).

2.2.1 Block fields

Mountain permafrost occurs in a wide range of surface materials and surface cover types. In many instances combinations of these factors lower the altitudinal limit of permafrost relative to the climatic limits. Indeed, the lowest active permafrost landforms in discontinuous mountain permafrost are typically found in coarse blocky materials, here after termed blockfields (Harris and Pedersen 1998). Blockfields are one of the most prominent surface covers in Norwegian alpine mountains (Figure 4), making them crucial for permafrost distribution in these areas. Blockfields exert a cooling influence on ground temperatures, producing a negative thermal anomaly (Juliussen and Humlum 2008, Gruber and Haeberli 2009). This anomaly was first recognized at the beginning of the 20th century (Balch 1900). Few studies had examined the relative ground temperatures of blockfields compared to surrounding fine-grained sediments until the 1990's (Harris and Pedersen 1998). Recently the thermal regime of blockfields have been studied in southern Norway (Juliussen and Humlum 2008). There are several reasons for the negative thermal anomaly in blockfields, and four of these are summarized and discussed by Harris and Pedersen (1998):

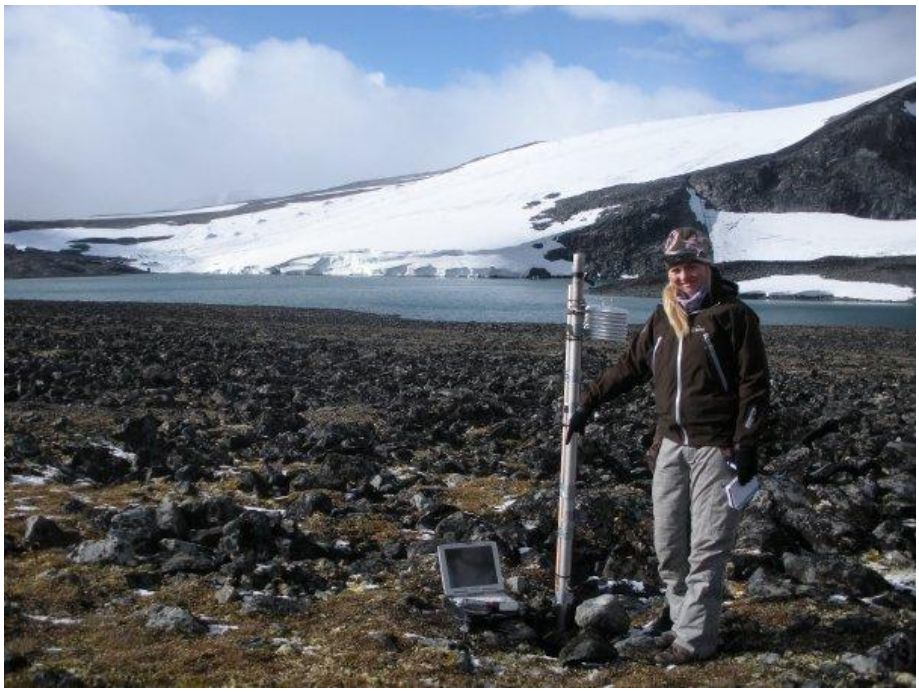

Figure 4: The image shows the borehole, air/ground station and i-button installation at the top of Juvvass (Juv-BH1). The station is installed in a blockfield consisting of relatively small blocks with no vegetation cover.

I. The Balch effect

The Balch effect, first introduced by Balch (1900), occurs because colder air is denser than warmer air. The density differences result in the displacement of warm air by cooler air in the pore spaces between rocks in blockfields. This process can only operate where large connecting spaces intersect the blocks, and where snow cover is limited.

II. The chimney effect

The chimney effect is a special case of the Balch effect, achieved in sloping blockfields. Cold air entering the blockfield through holes in the snow cover during winter is advected down slope due to density differences. Warmer air is displaced upslope and escapes through funnels. The result is a positive thermal anomaly in the upper part of the slope and a negative anomaly in the lower part.

III. Continuous air exchange with the atmosphere.

In areas without continuous winter snow cover, instantaneous warming and cooling of the blocky debris deposits has been observed to a considerable depth in response to changes in the air temperature. This results from a continuous air exchange with the atmosphere along the bare surface of the block field. The effect is enhanced in windy situations in steep slopes.

IV. Summer time evaporation/sublimation of water/ice in the blocky deposit.

During summer periods, water and ice in the blocky debris evaporate and sublimate removing latent heat from the surrounding environment and cooling the blocky debris.

The first three effects occur as a consequence of air convection. Indeed, Juliussen and Humlum (2008) demonstrated that the convection in the pore spaces in between the rocks is less important than initially presumed. They present a fifth hypothesis explaining the negative temperature anomaly with the higher effective thermal conductivity of rocks protruding through the snow cover (Juliussen and Humlum 2008). Blockfields have a higher surface roughness than the snow cover, often resulting in a limited or discontinuous snow cover. They also emphasize the effect of ice in the pore volumes during winter season, resulting in

zero curtain effect lasting up to a month in spring. The ice layer is also likely to increase the effective thermal conductivity in the blockfield during winter.

Harris and Pedersen (1998) found mean annual ground temperatures in blockfields to be 4-7°C colder than at adjacent sites with finer-grained soils, based on measurements at the Plateau Mountain, South Western Alberta and in the Kunlun Shan, China. They also observed that a thin block cover gives the same negative thermal anomaly effect as a thicker block cover. Measurements in southern Norway (Juliussen and Humlum 2008) show a negative temperature anomaly of only 1.3-2.0°C.

2.3 Permafrost modelling

The two main categories of mountain permafrost distribution models today are regionally calibrated empirical-statistical models and physically based process-oriented models (Riseborough et al. 2008, Harris et al. 2009).

Empirical-statistical distributed permafrost models relate documented permafrost occurrences to topo-climatic factors, such as elevation, slope and aspect, mean annual air temperature (*MAAT)* and solar radiation (Hoelzle 1996, Etzelmüller et al. 2001a, Wright et al. 2003, Heggem et al. 2005). These models have been criticized for being grey boxes with topo-climatic factors selected according to their relative influence on the total energy balance exchange (Harris et al. 2009). They also assume a steady-state condition and neglect effects of a three dimensional topography on heat fluxes in the ground. However, such models are easily applied, require only limited input parameters, and are relatively reliable if they are well calibrated locally or regionally.

Physically based process-oriented models give a more detailed reconstruction of the energy fluxes between the atmosphere and the permafrost, treating all the factors of the surface energy budget explicitly. Therefore they require large amounts of precise input data. They are particularly well suited for sensitivity studies with respect to interactions and feedbacks involved with climate-change scenarios (Harris et al. 2009).

Process-based permafrost models can be categorized based on temporal, spatial and thermal criteria (Riseborough et al. 2008). Temporally, models can either define equilibrium permafrost condition (equilibrium models), or model the transient evolution from an initial state to a current or future state (transient models). Simple thermal models can calculate the

presence or absence of permafrost, active layer depth (Z_{al}) or MAGT. These models are frequently based on empirical-statistical relations or equilibrium models using transfer functions between air and ground temperatures. Numerical models may define longer term progression of a deep-ground temperature profile (transient modelling), and is a more complex representations of the ground thermal regime (Riseborough et al. 2008). After the GCM's showed the impacts of the predicted climate changes during the next century, there has been an increased focus on transient permafrost modeling. Today there are two main directions in transient permafrost modelling; (1) the so called *post-processing method* (Nicolsky et al. 2007) where regional, national and global permafrost models of different levels of sophistication are forced with output from GCMs, and (2) the integration of permafrost models in coupled general GCMs. The main problem with the post-processing approach is that the feedback from the ground is not included in the GCM. In addition, the coarse resolution of the GCM's does not represent the permafrost processes satisfactory. This is improved by using downscaled regional climate models (RCMs) with a higher resolution, to force the permafrost model. The post-processing approach is often used to run equilibrium models, and the transient evolution of steady-state conditions can be reproduced. However, the model will not give any information about when the steady-state situation will occur because of the great lag between air temperatures and ground temperatures. Still with these limitations studies show satisfactory results using relatively simple equilibrium models (Sushama et al. 2006, Riseborough 2007). The more sophisticated fully coupled GCMs give a more direct modeling of the permafrost dynamics (e.g.Lawrence and Slater 2005). However, it has been problematic to obtain good results with this method, due to shallow soil columns, absence of an organic layer on the surface, coarse resolution and errors in the climate model. These issues have partly been solved in the latest implementations (e.g. Lawrence et al. 2008), but also these results show that these models still have a way to go before they reproduce present and future permafrost situation in an acceptable way.

Spatially, ground temperature can be modelled at one-dimension at a single point location, in two dimensions over transects, or geographically over a larger area. The spatial resolution should vary with the scale of implementation, from continental to regional or local scale, and the relative importance of climate, topography and ground conditions varies respectively (Harris et al. 2009). Spatial resolution should match the scale of variation in the area of implementation. Mountain permafrost is characterized by large variability and it is therefore

questioned whether a regional model can reproduce a permafrost distribution in mountainous areas (Harris et al. 2001b, Riseborough et al. 2008, Harris et al. 2009).

2.3.1 Heat conduction theory

The heat flow equation under transient conditions forms the basis for all geothermal models, and can be written as:

$$C_{eff}\frac{\partial T}{\partial t} = \frac{\partial}{\partial z}\left(K\frac{\partial T}{\partial z}\right) \quad (2.1)$$

The equation defines the temperature T (°C) at a given depth z (m) in the ground for a certain time step t, given in seconds. C_{eff} is volumetric effective heat capacity of the ground (J m^{-3}) and K is thermal conductivity (W $m^{-1}K^{-1}$).

When the ground undergoes freezing and thawing, release and absorption of latent heat of fusion is the dominant factor in heat flow (Williams and Smith 1989). This is usually accounted for by subsuming its effect in the volumetric effective heat capacity parameter (*Ceff*) (Riseborough et al. 2008):

$$C_{eff} = \sum x_i \rho_i c_i + L(\partial\theta_u/\partial T) \quad (2.2)$$

θ_u is the volumetric unfrozen water content of the subsurface material, T is the temperature of the ground (°*C*) and L is the volumetric latent heat of fusion (J m^{-3}). The volumetric heat capacity is summed over each component, i, of the ground (ice, solid earth material, water, etc.). x is the volume fraction of the component, ρ the density (kg m^{-3}) and c the specific heat capacity (J kg^{-1}).

2.3.2 The Stefan Solution

The most widely used analytical equation in permafrost models is the Stefan approximation for the moving phase change boundary. Assuming an initial thermal condition of the ground close to 0°C, and small diffusive effects relative to the movement of the thawing/freezing front, the boundary can be simplified to the Stefan solution. The Stefan solution is widely

used for active-layer characterization (Nelson et al. 1997, Shiklomanov and Nelson 2003, Heggem et al. 2006), and can be written as:

$$Z_{al} = \sqrt{\left[\frac{K}{\theta_w L}\right]\left[DD_{gs}\right]} \tag{2.1}$$

Z_{al} is the depth of the thawing or freezing front in meters and θ_w is the ground surface materials moisture content. DD_{gs} is degree days at the ground surface, which is often used instead of a step change in temperature when the formula is applied for field use (Lunardini 1981). A freezing or thawing degree day index integrates negative (*FDD*) or positive (*TDD*) daily temperatures respectively, and can be written as (Klene et al. 2001):

$$DD = S\int_0^{t_s} T - T_F dt \tag{2.2}$$

T_F is the freezing temperature of water (0°C), T is the daily mean temperature in the air or at the ground surface, t_s is the duration of the thawing/freezing season and *S* is a scaling factor from days to seconds. Thawing degree days (*TDD*) are used together with thermal conductivity of thawed ground (K_t) to calculate active layer thickness in ground underlain by permafrost. Freezing degree days (*FDD*) and thermal conductivity in frozen ground (K_f) are used to calculate the seasonal frost depth in non-permafrost areas. Permafrost will exist when seasonal thaw does not melt all of the frozen ground. Therefore, the occurrence of permafrost can be defined based on freezing and thawing indexes using a simplified version of Stefan solution where the ground temperature regime only dealing with the amount of energy transferred into the ground from the ground surface (Carlson 1952):

$$K_f * FDD_S > K_t * TDD_S \tag{2.3}$$

Conductivity values for frozen (K_f) and thawed (K_t) ground are given in $Wm^{-1}K^{-1}$. FDD_{gs} and TDD_{gs} are ground surface freezing and thawing degree days (°C day $year^{-1}$).

2.3.3 The TTOP-model

The TTOP-model (Smith and Riseborough 1996) is an equilibrium model of the climate-permafrost relationship combining a model for the thermal offset (Romanovsky and Osterkamp 1995) with *n*-factors linking air temperatures to the ground surface. The vertical atmosphere-ground temperature regime is characterized by a three layer system; air temperature, ground surface temperature and temperature at the top of permafrost (*MAGT*) (Figure 5). Ground surface temperatures are linked to air temperatures through transfer functions (*n*-factors), while mean annual ground surface temperatures (*MAGST*) and *MAGT* are linked by an analytical model using the effect of seasonal subsurface thermal property variations.

The model was first designed and implemented on continental scale to evaluate the conditions controlling the limits and continuity of the permafrost in the Canadian Arctic (Smith and Riseborough 2002). It was also implemented at regional scale (1 km^2) for the Mackenzie River Valley, Northern Canada. These results were calibrated with 154 boreholes along the Norman Wells Pipeline, and show good agreement with the currently available information on permafrost distribution and thickness (Wright et al. 2003).

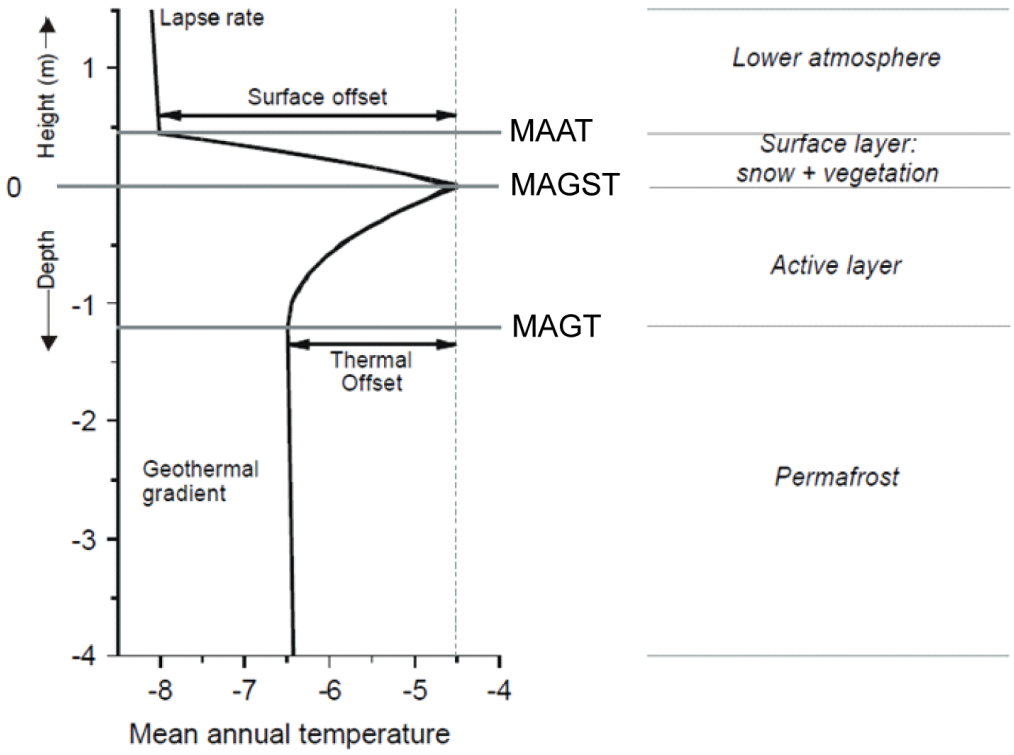

Figure 5: Vertical transect of the atmosphere-ground relationship, divided into three layers. Modified from Riseborough (2004).

The surface offset - The surface offset is defined as the difference between mean annual air temperatures (*MAAT*) and mean annual ground surface temperatures (*MAGST*). Ground surface temperatures are normally used as the upper boundary in ground surface temperature models. However, they have a much larger spatial variability than air temperatures, and only a limited amount of measured ground temperatures exists. Most air temperatures are measured at a standard height (2 m) above the ground (met.no 2010a). *n*-factors are transfer functions that link the ground surface temperature to the air temperatures. They are computed on seasonal basis using freezing and thawing indices.

$$nF = \frac{FDD_S}{FDD_A} \tag{2.4}$$

$$nT = \frac{TDD_S}{TDD_A} \tag{2.5}$$

The beginning and end of the freezing and thawing seasons must be defined in order to calculate seasonal based degree days. There is often a lag between changes in air and ground surface temperature due to the higher heat capacity of the surface (Riseborough 2004). The second problem is the variability around the freezing point in both ends of the season, especially in air temperature. Third, the ground surface temperature may remain at 0°C longer than the air temperature during the freeze back period in the fall, caused by the zero curtain effect when the active layer freezes back. No clear definition is given for how the seasons are defined. Most studies cited in this thesis use the surface temperature to define the seasons because of its lower temperature variability (Taylor 1995, Klene et al. 2001, Juliussen and Humlum 2007), while others do not define how the degree days are calculated (Jorgenson and Kreig 1988). In previous implementations of the TTOP model from the Mackenzie valley region, Canada (Wright et al. 2003), mean annual air temperature is converted to thawing and freezing degree days by integration of a sinusoidal annual temperature wave with amplitude of 23°C. Therefore the air temperatures have a clear transition between the seasons which are used to define freezing and thawing seasons (Wright et al. 2003).

The impact of vegetation on the summer surface cover is parameterized by *nT*-factors. *nT* is close to unity because the vegetation cover in most permafrost areas is sparse; in particular in areas of mountain permafrost. *nT* normally varies between 0.8 and 1.2 depending on the type

of surface cover and subsurface material properties (Jorgenson and Kreig 1988, Taylor 1995, Klene et al. 2001, Karunaratne and Burn 2004). *nF* parameterizes the winter surface offset, and is related to snow-cover thickness. The connection between air and ground surface temperatures is highly variable during the winter season, and *nF* ranges from as low as 0.15 at sites with thick snow cover and up to unity at sites with no or very limited snow cover (Jorgenson and Kreig 1988, Taylor 1995, Klene et al. 2001, Karunaratne and Burn 2004). The *nF* does also vary with the active layer water content because of the release of latent heat during freezing. The amount of freezing degree days in permafrost areas are much larger than the amount of thawing degree days, and therefore the model is more sensitive to changes in *nF*.

n-factors were originally used for engineering purposes (Lunardini 1978), but have later been used for natural environments (Jorgenson and Kreig 1988, Taylor 1995, Klene et al. 2001, Juliussen and Humlum 2007). Lunardini (1978) states that *n*-factor values are of limited value unless the site for which it is applied is very close to the site of calculation. They are however widely used because of their simplicity compared to alternative methods.

The thermal offset - The thermal offset (ΔT_k) is defined as the difference between *MAGST* and *MAGT* (Goodrich 1978, Burn and Smith 1988, Smith and Riseborough 1996):

$$\Delta T_k = MAGT - MAGST \tag{2.6}$$

The thermal offset relates to the different thermal conductivities in frozen (K_f) and thawed (K_t) ground. Thermal conductivity of ice is approximately four times larger than water, and therefore the thermal offset highly depends on the subsurface materials moisture content. When water is present in the ground, the heat transfer out of frozen ground to the air in winter will differ from the heat transfer from the air into the ground through the thawed active layer in summer. This implies progressively colder temperatures down through the active layer, and makes it possible to maintain permafrost also when the mean annual ground surface temperature is above 0°C.

Kudryavtsev (1974) presented a relation for the maximum annual depth of thaw propagation and the mean annual temperature at the base of the active layer (described in Chapter 2.3.4). Based on Kudryavtsev's model, Romanovsky and Osterkamp (1995) presented a formula for *MAGT* together with an analytical proof. Independently, Smith and Riseborough (1996)

determined the same relationship for *MAGT*, based on a numerical geothermal simulation model. To simplify the equation the thermal conductivity ratio can be defined as r_k:

$$r_k = \frac{K_t}{K_f} \tag{2.7}$$

and the thermal offset (ΔT_k) can be written:

$$\Delta T_k = \frac{TDD_s(r_k - 1)}{\tau}, K_t TDD_s \leq K_f FDD_s \tag{2.8}$$

$$\Delta T_k = \frac{FDD_s(1 - r_k)}{\tau}, K_t TDD_s > K_f FDD_s \tag{2.9}$$

Subsurface material properties influencing the r_k-factor are examined in Riseborough (2004), both with empirical and theoretical thermal conductivity models. Riseborough (2004) showed that the geometric mean gives the overall best estimate of bulk conductivity in mixtures with a wide range of porosities (Riseborough 2004). The geometric mean is widely used to calculate thermal conductivity for mixed soils, and has been studied by Johansen (1975):

$$K = \prod_{i=1}^{n} K_i^{x_i} \tag{2.10}$$

Bulk thermal conductivity (K) is calculated as the product of thermal conductivity (K) of each soil constituent (*i*) raised to the power of the respective volume fraction (x), where n is the number of soil constituents.

The relation has no physical basis, but is considered valid for saturated soils (Johansen, 1975). Riseborough (2004) shows that r_k is a reasonably reliable function of soils moisture content for saturated, unsaturated and organic soils, and the geometric mean gives the overall best estimate for all soil types. However, the uncertainty in conductivity estimates of unsaturated soils is greater at lower soil moisture contents (Riseborough 2004). The TTOP-model assumes a constant r_k, and does not include the effect of unfrozen water. Mineral soils range in r_k from 0.6 to 0.9, depending on the water content. The greatest range in r_k values is found in organic soils varying from 0.3 in saturated soils to near 1.0 for dry organic soil (Smith and Riseborough 2002). r_k for bedrock is close to 1.0, and therefore bedrock has negligible thermal offset.

The TTOP-model

By including the *n*-factors in the model for the thermal offset, the mean annual ground temperature at the top of the permafrost can be derived from air temperatures. *MAGT* is calculated by the following equation in the TTOP-model:

$$MAGT = \frac{(r_k * nT * TDD_a) - (nF * FDD_a)}{\tau}, K_t TDD_s \leq K_f FDD_s \qquad (2.11)$$

$$MAGT = \frac{(nT * DDT_a) - (\frac{1}{r_k} * nF * DDF_a)}{\tau}, K_t TDD_s > K_f FDD_s \qquad (2.12)$$

Equation 2.13 defines temperature at the top of permafrost, while equation 2.14 defines the temperature at bottom of seasonally frozen ground. *nT* and *nF* are scaling factors between air and ground surface indexes during respectively thawing and freezing season (see equation 2.10 and 2.11). r_k is the ratio between thermal conductivity in thawed (K_t) and frozen (K_f) ground. τ is the period (365 days).

2.3.4 Kudryavtsev's approach

Kudryavtsev's approach (Kudryavtsev et al. 1974) is an alternative model for estimation of maximum annual thaw/freeze depth and the temperature at the base of the active layer. The air temperature is assumed to be a sine curve:

$$T(t) = T_a + A_a \sin(\frac{2\pi}{\tau} t) \qquad (2.13)$$

For simplicity *MAGT* is termed T_a in this chapter. A_a is the seasonal air temperature amplitude, τ is the period of the sine wave (one year) and t is the time. By using the Fourier temperature wave propagation theory in a medium with phase transitions, such as frozen ground (Sazonova and Romanovsky 2003), Kudryavtsev found a formula for *MAGT* by estimating the dampening of the air temperature through a surface buffer layer and the active layer (Figure 6). The buffer layer includes vegetation cover, snow cover and soil organic horizon. This also led to a formula for the active layer thickness (Z_{al}).

A modified Kudryavtsev's approach (*mKA*) was presented by Sazonova and Romanovsky (2003) and implemented at a regional scale in the GIPL1-model (Geophysical Institute Permafrost Laboratory, University of Alaska, Fairbanks; Sazonova & Romanovsky (2003) over two transects in Alaska and Siberia. The mKA-model provides a physical representation of the surface offset, treating the complex system of snow cover, vegetation and soil organic horizon as a set of individual layers with different physical properties. Air temperature is represented as a seasonal range of temperature variations (A_a) and the mean annual air temperature (T_a).

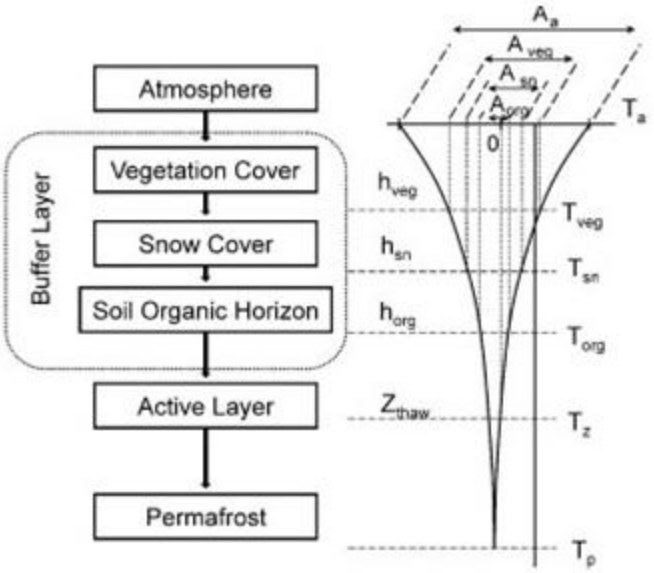

Figure 6: The modified Kudryavtsev's approach treats the thermal regime from atmosphere to ground as a system of different layer. The surface offset consists of a buffer layer including vegetation and snow cover, and soil organic horizon.

Snow cover - The thermal effect of the snow cover on the mean annual air temperature (ΔT_{sn}) and amplitude (ΔA_{sn}) during the winter season is calculated as follows:

$$\Delta A_{sn} = \Delta A \times 0.5 \times \frac{\tau_1}{\tau}, \tag{2.14}$$

$$\Delta T_{sn} = \Delta A_{sn} \times \frac{2}{\pi}, \tag{2.15}$$

τ_1 is the length of the winter season and ΔA is defined as:

$$\Delta A = A_a(1 - \frac{1+\mu}{\sqrt{s}}) \quad (2.16)$$

μ is described in equation 2.20-2.23, and s is the mean thermal effect of the snow cover calculated from the following equation:

$$s = e^{2H_{sn}\sqrt{\frac{\pi C_{sn}}{\tau K_{sn}}}} + 2\mu\cos\left(2H_{sn}\sqrt{\frac{\pi C_{sn}}{\tau K_{sn}}}\right) + \mu^2 e^{-2H_{sn}\sqrt{\frac{\pi C_{sn}}{\tau K_{sn}}}} \quad (2.17)$$

H_{sn} is the seasonal average snow depth (m), C_{sn} is the average snow heat capacity in $Jm^{-3}K^{-1}$, and K_{sn} is the average snow thermal conductivity ($Wm^{-1}K^{-1}$). The contrast in thermal properties between the snow cover and the underlying ground is characterized by the dimensionless parameter μ, ranging from -1 to 1. This parameter reflects the influence the underlying ground material has on the insulating effect of the snow cover, and is defined as

$$\mu = \frac{\sqrt{K_{sn}C_{sn}} - \sqrt{K_f C_{eff}}}{\sqrt{K_{sn}C_{sn}} + \sqrt{K_f C_{eff}}}. \quad (2.18)$$

C_{eff} is the effective heat capacity of the substrate below the snow cover ($Jm^{-3}K^{-1}$), and is defined as:

$$C_{eff} = C_f \frac{\alpha - \beta}{(\alpha - \beta) - \ln\frac{\alpha+1}{\beta+1}} \quad (2.19)$$

The C_f is the heat capacity of frozen ground ($Jm^{-3}K^{-1}$). The two dimensionless parameters α and β reflects the ratio of sensible and latent heat (Sazonova and Romanovsky 2003).

$$\alpha = \frac{2A_a C_f}{L} \quad (2.20)$$

$$\beta = \frac{2|T_a|C_f}{L} \quad (2.21)$$

The temperature at the top of vegetation (T_{vg}) cover can thus be calculated as:

$$T_{vg} = T_a + \Delta T_{sn} \quad (2.22)$$

$$A_{vg} = A_a - \Delta A_{sn} \quad (2.23)$$

Vegetation cover – The thermal effect of the surface vegetation cover is calculated from thermal diffusivity and height of the vegetation. The vegetation model is separated into the winter cooling period (ΔA_1) and the summer warming period (ΔA_2):

$$\Delta A_1 = \left(A_{vg} - T_{vg}\right) \times \left(1 - e^{-H_{vg}\sqrt{\frac{\pi}{D_{vf}2\tau_1}}}\right) \tag{2.24}$$

$$\Delta A_2 = \left(A_a - T_a\right) \times \left(1 - e^{-H_{vg}\sqrt{\frac{\pi}{D_{vt}2\tau_2}}}\right) \tag{2.25}$$

H_{vg} is the height of vegetation cover in meters, D_{vf} and D_{vt} is thermal diffusivity of the vegetation cover in frozen and thawed states respectively and τ_1 and τ_2 is the length of the winter and summer seasons respectively. The vegetation effect on the seasonal temperature amplitude (ΔA_v) and the mean annual temperature (ΔT_v) is calculated as:

$$\Delta A_v = \frac{\Delta A_1 \tau_1 + \Delta A_2 \tau_2}{\tau} \tag{2.26}$$

$$\Delta T_v = \frac{\Delta A_1 \tau_1 - \Delta A_2 \tau_2}{\tau} \times \frac{2}{\pi} \tag{2.27}$$

This result in a relation for temperature (T_{gs}) and seasonal amplitude (A_{gs}) at the ground surface expressed as:

$$T_{gs} = T_{vg} + \Delta T_v \tag{2.28}$$

$$A_{gs} = A_{vg} - \Delta A_v \tag{2.29}$$

Thermal offset – Kudryavtsev (1981) gave an analytical equation to estimate the temperature at the top of permafrost, *MAGT*. The equation for *MAGT* (T_{ps}) can be written as follows:

$$T_{ps} = \frac{0.5T_{gs}\left(K_f + K_t\right) + A_{gs}\frac{K_t - K_f}{\pi} \times \left[\frac{T_{gs}}{A_{gs}} arcsin\left(\frac{T_{gs}}{A_{gs}}\right) + \sqrt{1 - \frac{\pi^2}{A_{gs}^2}}\right]}{K^*} \tag{2.30}$$

This relation was formally derived in Romanovsky and Osterkamp (1995). They also derived an alternative way to estimate the same physical relation, based on ground surface thawing

(TDD_{gs}) and freezing (FDD_{gs}) indices together with thermal conductivity values for thawed (K_t) and frozen (K_f) ground. The formula for estimating the thermal offset is the same as Smith and Riseborough (1996) derived from numerical simulations, presented in Chapter 2.3.3, Equation 2.10 and 2.11. Using this formula, *MAGT* (T_{ps}) can be calculated as follows:

$$T_{ps} = T_{gs} + \Delta T_k \tag{2.31}$$

Kudryavtsev (1974) has also provided a semi-empirical formula for the depth of seasonal thawing or freezing (Z_{al}). This formula assumes homogeneous ground properties and does not take unfrozen water into account. It has been shown that the Kudryavtsev's approach gives a higher accuracy for Z_{al} and *MAGT* than the Stefan solution (Romanovsky and Osterkamp 1997), and allow for estimation of permafrost temperatures within 0.5°C. The equation can be written as (Romanovsky and Osterkamp 1997):

$$Z_{al} = \frac{2\left(A_{gs} - T_{ps}\right) * \sqrt{\frac{KPC_t}{\pi}} + \frac{\left(2A_{ps}CZ_c + L * Z_c\right) * L\sqrt{\frac{K\tau}{\pi C}}}{2A_{gs}CZ_c + \left(2A_{ps}C + L\right) * \sqrt{\frac{K\tau}{\pi C}}}}{2A_{ps} * C + L} \tag{2.32}$$

where

$$A_{ps} = \frac{A_{gs} - T_{ps}}{\ln\left[\frac{A_{gs} + L/2C}{T_{ps} + L/2C}\right]} - \frac{L}{2C} \tag{2.33}$$

and

$$Z_c = \frac{2\left(A_{gs} - T_{ps}\right) * \sqrt{\frac{K * \tau * C}{\pi}}}{2A_{ps}C + L} \tag{2.34}$$

Z_{al} is the depth of freezing or thawing (m), A_{gs} is the amplitude at the ground surface (°C), T_{gs} the mean annual ground surface temperature(°C); K and C are the thermal conductivity and volumetric heat capacity of the ground (W m^{-1} $°C^{-1}$ and J m^{-3} $°C^{-1}$); P is the period of the temperature cycle (1 year, expressed in seconds) and L is the volumetric latent heat of fusion (J m^{-3}).

3. Area of study

3.1 Geographical setting

Norway is situated on the northwestern part of the Scandinavian Peninsula, Northern Europe. Mainland Norway stretches from 58°N to north of 71°N and from 5°E to 31°E. Oxygen isotope studies of deep sea sediment cores shows that Norway probably has been glaciated more than 40 times during Quaternary (Vorren and Mangerud 2007). However, because of the erosional impacts of the Scandinavian ice cap, which exceeded 3000 m in thickness, terrestrial evidence is only found for the last major glaciation. The last glacial maximum occurred during late Weichsel (17 000 – 21 000 B.P.), and by 8 500 B.P. the country was largely ice free. Most sediment such as clay, sand and moraine were deposited during the last ice advance and the subsequent retreat. The land is still rising due to isostatic uplift, and is dominated by mountainous terrain intersected by deep fjords. The Scandinavian mountain range reaches from the very southern end of Norway, northwards dividing the eastern and western parts of southern Norway. It turns eastwards south of Trondheim until it reaches the Swedish border (Figure 7). The mountain range in Southern Norway includes mountainous regions such as Hardangervidda, Rondane, Jotunheimen, Reinheimen, Trollheimen and Dovre. The Scandinavian mountains cross back into Norway in the north with the alpine region of Lyngsalpene. Further north, the mountain range gradually decreases in elevation, reaching sea level at the Barents Sea. All the previous mentioned mountain areas contain peaks higher than 1600 meters. The highest mountain in Norway is Galdhøpiggen (2469m) located in Jotunheimen. This gives a large variety in topography and type of landscape; from lower altitude plaines and mountain plateaus containing large areas of palsa mires in Northern Norway (Figure 8, left), to alpine mountain areas in Jotunheimen (Figure 8, right).

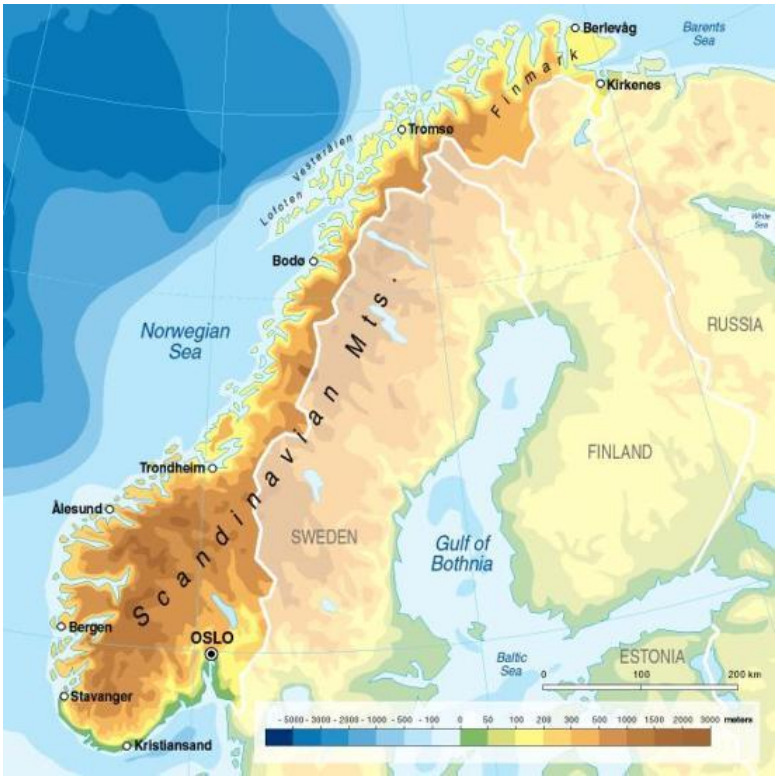

Figure 7: Topographical map for mainland Norway, showing the Scandinavian mountain range reaching from southern to northern Norway. The range is a clear divide between the west coast and the more continental eastern parts of Norway (UNEP/GRID-Arendal 2001).

Figure 8: Left: Palsa mire in flat tundra-like landscape in Finnmark. Foto: Åse Manengen. Right: Alpine mountains in Jotunheimen.

3.2 Climate setting

Norway borders the North Sea to the southwest, the Norwegian Sea to the northwest and the Barents Sea to the north. To the east, borders are shared with Sweden, Finland and Russia. This coastal setting together with the Scandinavian mountain range heading north-south plays a decisive role in the regional climate. Locations at latitudes ranging from 58°N to 71°N normally have a cool continental to subarctic climate. Norway's climate is moderated by the Gulf Stream bringing warm water up along the coast of Norway and is characterized as marine-temperate. Climate on the west coast is dominated by frontal and orographic weather systems (met.no 2010b). Cyclones developing along the polar front zone tend to create a sharp transition layer between warm, moist air in the south, and cold, dry air in the north. Frontal precipitation is generated when the warm air masses are lifted above the colder air masses. When moist air masses are brought from the Atlantic Ocean to the west, they are forced up the steep mountains at the west coast of Norway generating large amounts of orographic precipitation. A rain shadow is created on the eastern side of the mountains, explaining the much drier climate typical for eastern Norway. Air masses coming from the south and east of Norway mainly bring drier air. Thus, there is a steep precipitation gradient going east-west, ranging from as low as 278 mm/yr in southeastern Norway (Øygarden, Oppland) and up to above 4000 mm/yr in southwestern Norway (see Figure 9, left) (senorge.no 2010). Air temperatures in Norway are highly dependent on elevation, but also on the distance to the sea. Northern Norway has in particular a clear east-west gradient in air-temperatures (Figure 9, right).

According to Köppens Climate Classification most of the west coast of Norway has a warm-temperate, maritime climate, eastern parts of Southern Norway, Trøndelag and Finnmark has a cold-continental climate, and the high mountain areas and southern parts of Finnmark have an arctic tundra climate (Figure 10, right) (met.no 2010c).

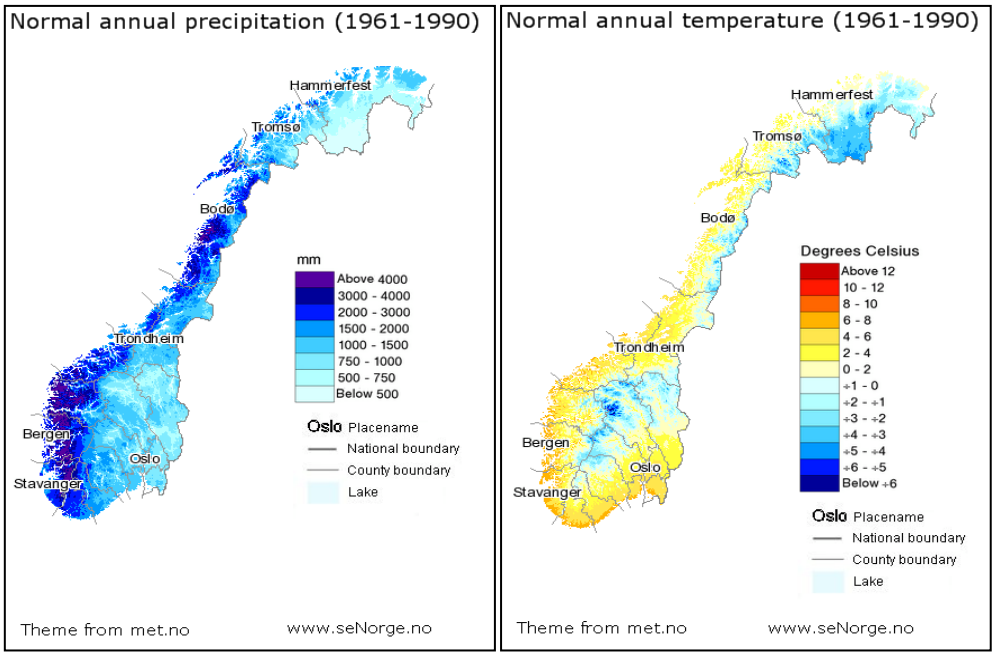

Figure 9: Precipitation (left) and air temperature (right) maps for last normal period in Norway, provided by SeNorge.

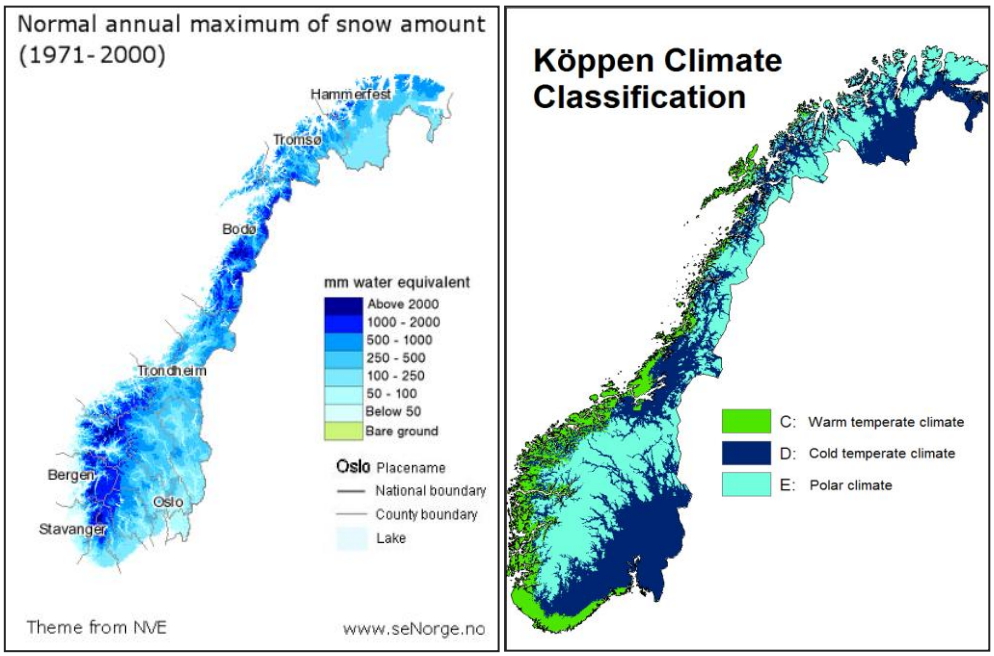

Figure 10: Left: mean annual maximum snow amount for last normal period (senorge.no 2010). Right: Köppens climate classification for Norway (met.no 2010c).

3.3 Permafrost in Norway

Permafrost is mainly found as mountain permafrost in Norway (Heggem et al. 2005). Several studies of ground temperature have been conducted in Southern Norway, resulting in a detailed picture of the permafrost distribution in specific areas. Air temperature, determined by elevation, are the most important factors controlling the distribution of permafrost in Norway, in contrast to the Alps where topographic expositions is of high importance (Isaksen et al. 2002). Studies from the Jotunheimen and Dovre areas, based on BTS measurements, imply a lower limit of possible permafrost at 1460 m a.s.l. and 1490 m a.s.l., respectively (Isaksen et al. 2002). However, because of topographic effects, snow conditions and surface characteristics, permafrost is found at lower elevations. Borehole measurements show permafrost down to 1350 m a.s.l. on Dovre (Sollid et al. 2003). In the Femunden region, central-eastern Norway the altitudinal limit of mountain permafrost is 1100-1300 m a.s.l., which is the lowest permafrost limit in southern Scandinavia (Heggem et al. 2005). Regional-scale permafrost mapping based on meteorological data (*MAAT*) and field measurements (Etzelmüller et al. 1998, Etzelmüller et al. 2003) indicates a lower limit of permafrost at 1600 m a.s.l. in western Norway and 1300 m a.s.l. in eastern, more continental parts of Norway.

Fewer studies have been undertaken in northern Norway. Gridded mean annual air temperature (*MAAT*) maps indicate a similar altitudinal gradient for discontinuous permafrost limit also in northern Norway, ranging from above 1000 m a.s.l. at the coastal sites, and decreasing down to below 400 m a.s.l. in eastern, more continental parts (Etzelmüller et al. 2008, Isaksen et al. 2008). In the Gaissane mountains permafrost is widespread above 350-450 m a.s.l. (Farbrot et al. 2008). Permafrost is widespread in Finnmark in areas with *MAAT* < -3°C, but sporadic permafrost can also be found below treeline at palsa mires or at local exposed sites where snow does not accumulate (Isaksen et al. 2008).

4. Methodology

Many different attempts with varying degree of sophistication have been made to model the climate – permafrost relationship. The CryoGRIDeq-models consist of the implementation of the TTOP-model (Smith and Riseborough 1996) and the modified Kudryavtsev's approach (mKA) (Sazonova and Romanovsky 2003). Both models are equilibrium models of the climate-permafrost relationship defining the temperature at the top of permafrost from air temperature data. The vertical atmosphere-ground temperature regime is treated as a three layer system in both models, consisting of (1) air temperature, (2) ground surface temperature and (3) temperature at the top of permafrost/base of seasonally frozen ground (*MAGT*). The parameterization of the thermal offset in both models are based upon the Kudryavtsev model, utilizing the difference in thermal conductivity in frozen and thawed ground (Kudryavtsev et al. 1974, Romanovsky and Osterkamp 1995). The main difference between the models is the implementation of the surface offset. The TTOP-model includes seasonal *n*-factors derived from vegetation and snow cover distribution to summarize the surface energy exchange (Lunardini 1978). Correspondingly, the mKA utilizes a more physically based parameterization of the snow- and vegetation cover.

The CryoGRIDeq-models are operated on 1km^2 resolution for mainland Norway, and forced with operationally gridded air temperature, snow depth and snow water equivalent data from the period 1957-2010, provided by SeNorge (www.senorge.no). The models are implemented according to the equations described in Chapter 2.3.3 and 2.3.4, and all scripts are written in MATLAB. The general implementation processes are shown in the flow charts in Figure 11, and the total program code with a user interface are included in Appendix F. The models are adjusted for a mountain permafrost environment, primarily using field data from the CRYOLINK project including air-ground stations measuring temperature, boreholes with temperature loggers, BTS-measurements, and ground surface temperature loggers. These data are mainly used for developing *n*-factors. Subsurface material map and conductivity data provided by the Geological Survey of Norway (NGU) are used to produce a map for r_k-values (Olesen et al. 2010). Blockfields are studied in particular, and a new map of blockfield distribution for Norway is made from classification of Landsat images, using spectral analysis. The TTOP-model is modified to deal with the negative thermal anomaly in blockfields, based upon field data from the CRYOLINK project and previous studies of thermal regimes in blocky terrain. Different algorithms are used for permafrost and non-

permafrost areas, and a modified Stefan solution by Carlson (1952), presented in equation 2.6, are used to determine the general thermal state of the ground. Both models calculate annual mean temperatures at the permafrost table temperatures (AMGT) and average these over the period of study.

4.1 Input data

4.1.1 Meteorological data

Gridded 1km^2 air temperatures, snow depth (*SD*) and snow water equivalent (*SWE*) data are provided by SeNorge, a web service for freely available meteorological data developed by the Norwegian Meteorological Institute (met.no), Norwegian Water and Energy Directorate (NVE) and Norwegian Mapping Authority. Versions 1.1 of the gridded datasets are used in this thesis (Mohr 2009). Air temperatures and precipitation grids are produced by met.no, from 24-hour mean temperature and accumulated precipitation at 2 meters height. Data are collected at temperature and precipitation stations distributed all over Norway. The number of stations in use varies from every time the interpolation algorithm is run; in 2004 the total number of precipitation and temperature stations was 630 and 150, respectively (Engeset et al. 2004). All data are de-trended using a DEM based on the DTED elevation model from Statens Kartverk (Berge 2009). This DEM has a horizontal resolution of 100 meters (Mohr 2009). A lapse rate of -0.0065 °Cm^{-1} is used. Precipitation data, corrected for systematic losses from wind, are used to produce a precipitation map from triangulation. Precipitation is expected to increase with 10%/100m from 0m to 1000m elevation, and with 5%/100m above 1000m elevation. Precipitation at temperatures below 0.5°C is accumulated as snow in the model, and snow water equivalent (*swe*) data are calculated directly from precipitation and temperature data. Snow depth data are produced from *swe*, using an algorithm taking snow melt, snow accumulation and change in density and height with time into account. The snow map data are produced by NVE (Engeset et al. 2004).

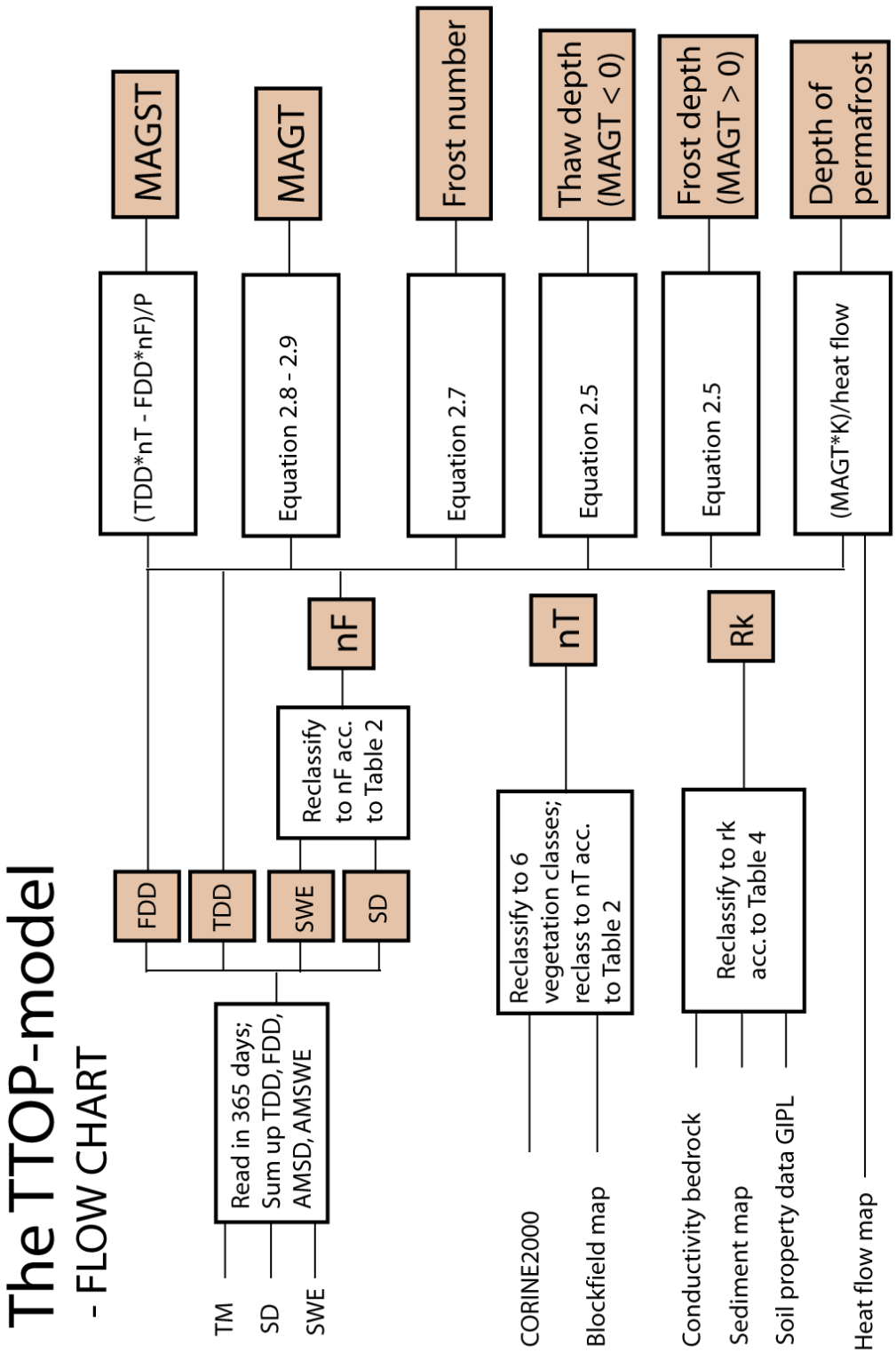

Figure 11: Flow chart for the TTOP-model implementation.

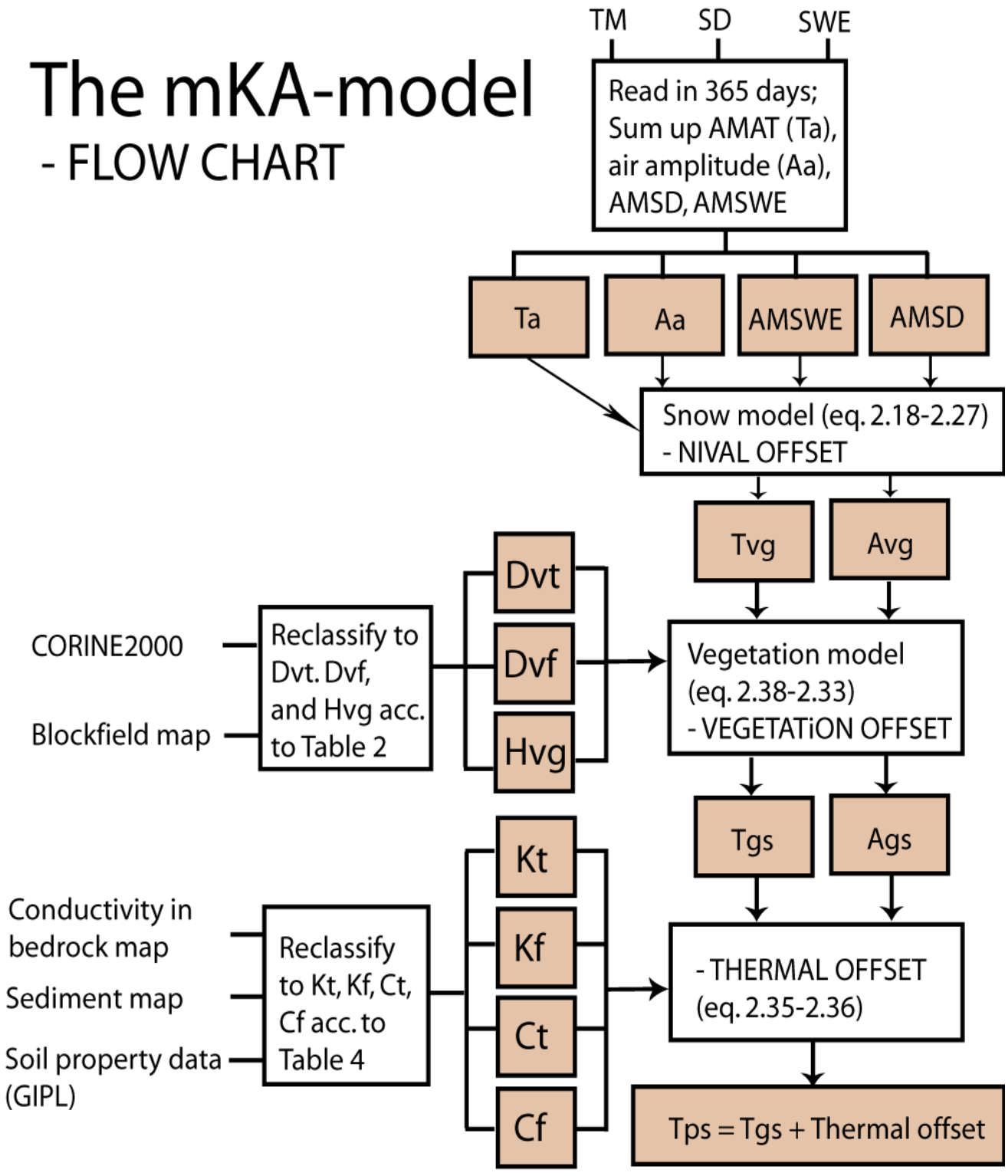

Figure 12: Flow chart showing the mKA-model implementation.

4.1.2 Vegetation

Vegetation is represented with the Norwegian CORINE Land Cover (CLC) 2000 map (Heggem and Strand 2010). CLC is a seamless European land cover vector database. CLC2000 for Norway was completed by the Norwegian Forest and Landscape Institute (Institutt for skog og landskap) in 2008, produced from existing national land cover datasets wherever available. The land cover map has been reclassified to 5 land cover classes (Figure 14) a); (1) forest, (2) vegetated, (3) barren ground (4) mires and (5) no data (permanent water/ice bodies and urban areas).

4.1.3 Blockfield map

Blockfields are poorly mapped by existing land cover and subsurface material maps for Norway. Blockfield maps are therefore produced from Landsat images covering mainland Norway. A complete list of Landsat images is provided in Appendix C.1. The unique spectral signature of open block fields is utilized and open block fields are successfully separated from bedrock and other land cover types. Five bands from Landsat 4-5 (TM) were used; band3 (0.63-0.69 µm), band4 (0.76-0.90 µm), band5 (1.55-1.75 µm), band6 (10.40-12.50 µm) and band 7 (2.08-2.35 µm), downscaled to 240m resolution before classification. Areas of block fields are classified based on the following three variables:

- Variable 1 = 100 * ((band3 + band5) /2) / band4)
- Variable 2 = 6 * ((atand (100 / (band6 – band7)) -30)
- Variable 3 = band5 – band3

Areas of block field will cluster around the point [150 70 230] and class membership was defined as a function of Euclidic distance from this centre point. The final 240m block field map has been validated against a digitized 1:100 000 Quaternary Geological map for the area Trollheimen-Sunndalsfjella-Oppdal (Sollid et al. 1980). 99 validation points were chosen at random locations (Appendix C.3), giving an overall accuracy (number of correctly classified pixels out of the number of reference pixels) of 93%. Producer's accuracy is a measure of how well the reference data pixels are classified, while the user's accuracy is the probability that a pixel classified into a category actually represents the category on the ground (Table 1).

Table 1: Cross-referance table for the validation of the blockfield classification shown in Appendix C.3.

	Classification data			
Reference data	***Blockfield***	***Not blockfield***	**Row total**	**Producer's accuracy**
Blockfield	9	4	13	**69 %**
Not blockfield	3	83	86	**97%**
Column total	12	87	99	
User's accuracy	**75 %**	**95%**		
Errors of Commission	*25 %*	*5%*		

There is a significant difference in the total number of pixels in the two classes (1) blockfield and (2) not blockfield. Indeed, when random reference pixels are generated, there might be a skewed distribution of the representation from the two classes. The $\hat{k}$ statistic is a measure of the difference between the actual agreement between the reference data and a random classifier. Thus, it gives an indicator of the extent to which the percentage correct values of an error matrix are due to "true" agreements versus "chance" agreements. The $\hat{k}$–value approaches 1 when true agreement approaches 1 and chance agreement approaches 0 (Lillesand et al. 2008). $\hat{k}$ can be defined as

$$\hat{k} = \frac{observed\ accuracy - chance\ agreement}{1 - chance\ agreement} \tag{3.1}$$

and is calculated as

$$\hat{k} = \frac{N \sum_{i=1}^{r} x_{ii} - \sum_{i=1}^{r} (x_{i+} * x_{+i})}{N^2 - \sum_{i=1}^{r} (x_{i+} * x_{+i})} \tag{3.2}$$

where
r = number of rows in the error matrix
xii = number of observations in row i and column i (on the major diagonal)
xi_+ = total of observations in column i (shown as marginal total to right of the matrix)
x_+i = total of observations in row i (shown as marginal total at bottom of the matrix)
N = total number of observations included in matrix

The $\hat{k}$ for the agreement between the observed and classified pixels at the 99 points chosen for validation in the Trollheimen, is 0.68. This gives an indication that the classification is 68% better than a classification resulting from chance. At some of the validation points, blockfields were classified from the Landsat images, but not in the Quaternary map. When interpreting these areas more closely with aerial photos from "Norge i bilder", it turns out that the satellite classification was correct at almost all sites. This suggests that the blockfield map actually gives a better classification than available large scale maps in some areas. The final blockfield map is shown in Figure 14, b) and on larger scale in Appendix C.4 and C.5.

4.1.4 Subsurface material property data

28 000 point measurements of petro-physical data such as bedrock density and thermal conductivity in bedrock have been provided by the Norwegian Geological Survey (NGU) (Olesen et al. 2010). Maps of bedrock class (Sigmond 2002) and subsurface material (Thoresen 1991) for Norway are also provided by NGU. The map of subsurface materials is included in Appendix D.8. Point measurement data are assigned to bedrock classes, and average density and thermal conductivity values for each class are calculated. Variation of thermal conductivity values within each bedrock class is shown in Figure 13 (Angst 2010). Density and thermal conductivity of dry sediments are calculated by subtracting an estimated percentage value from the underlying bedrock, due to a higher pore volume in sediments (Angst 2010). The final density and thermal conductivity maps for bedrock are shown in Figure 14, c and d.

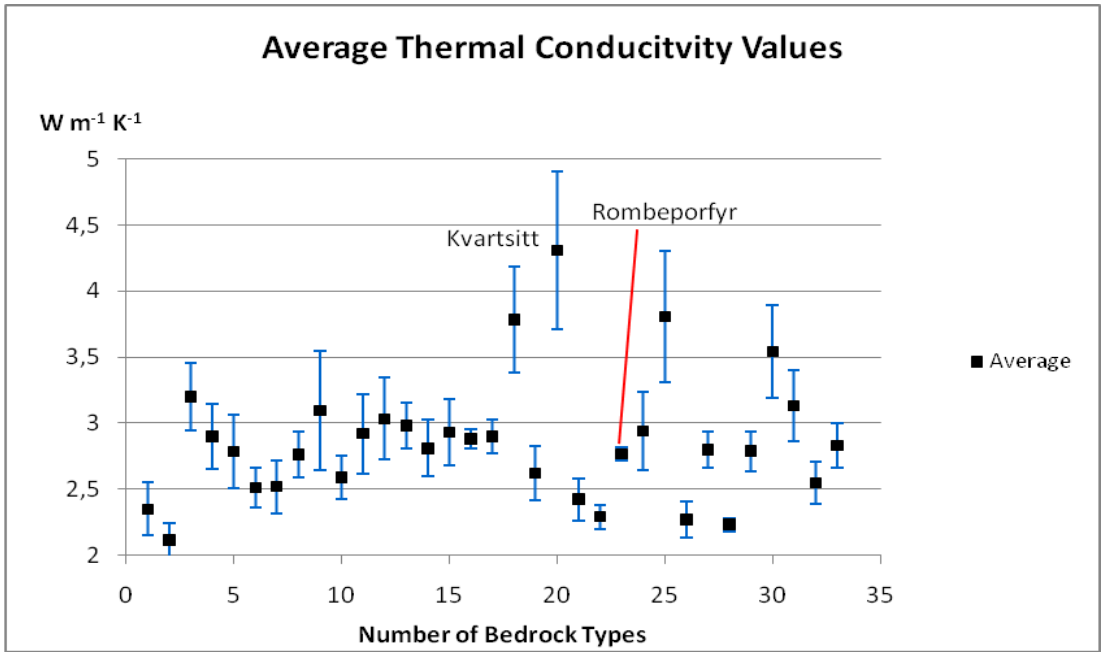

Figure 13: Average thermal conductivity values and variation within each class (Angst 2010).

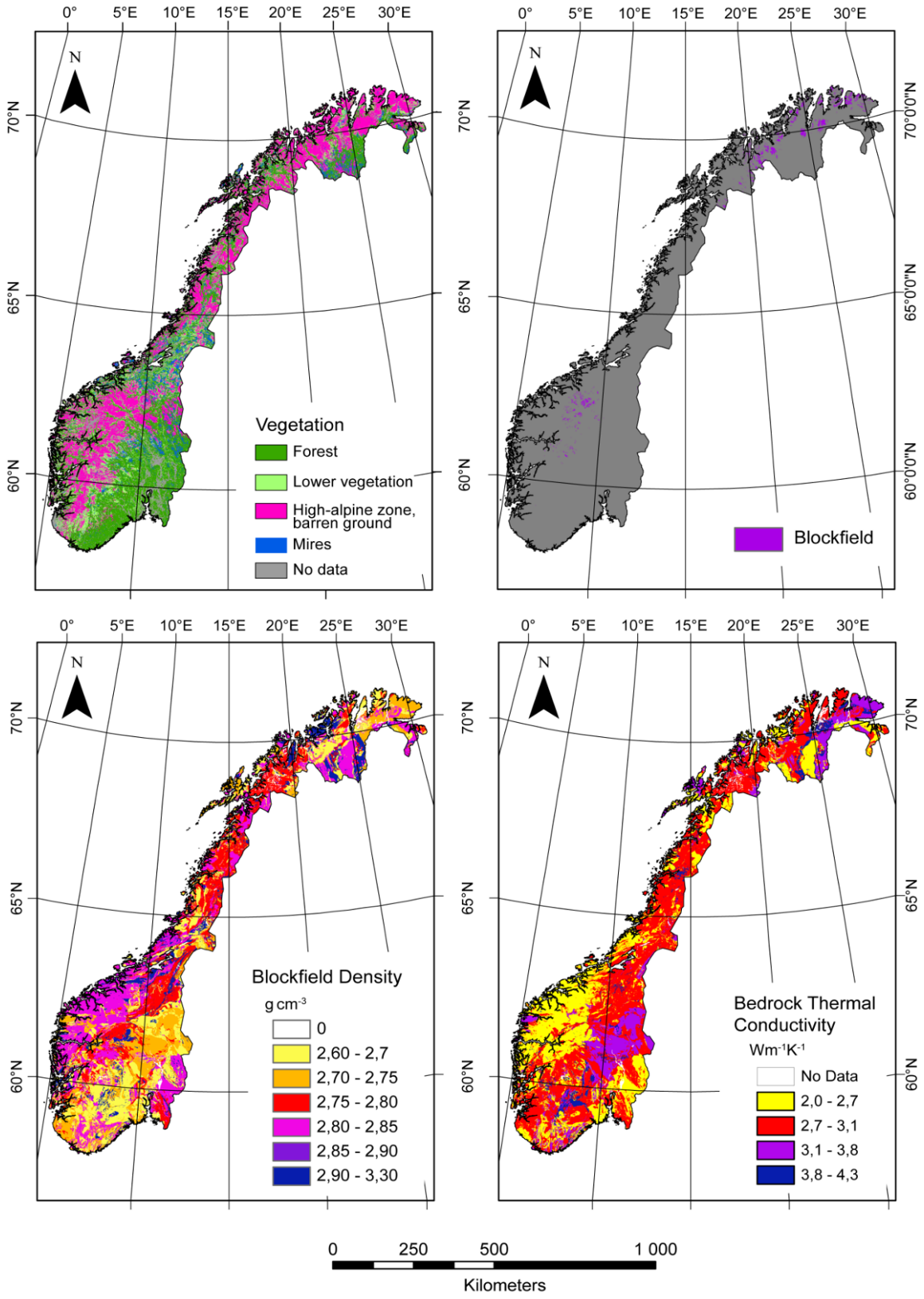

Figure 14: Input data: a) CORINE 2000 vegetation map reclassified, b) blockfield map produced from Landsat TM-images, c) bedrock density and d) bedrock thermal conductivity derived from NGU petrophysical data.

4.2 The surface offset

4.2.1 Parameterization of *n*-factors - CryoGRID-ttop

During the CRYOLINK project 17 air/ground-stations measuring daily air and ground surface temperature have been installed to relate certain vegetation cover classes to accurate *n*-factors (Figure 15) (Farbrot et al. submitted). In addition, air and ground temperature data from one PACE borehole are included in the parameterization of *n*-factors. The sites are classified on the basis of vegetation cover and assigned to the five land cover classes in the land cover map (Figure 14, a). Data from more than 300 miniature temperature data loggers distributed all over Norway (Figure 15) measuring daily ground surface temperatures are also available. These can be used for *n*-factor estimation by connecting them to operationally gridded air temperature data (see Chapter 6.3.2). However, this is difficult and should be done with care, since the sub-grid variability for most areas are large. Therefore, only MTD-loggers representing the average snow situation of the surrounding area are included. The 18 air/ground-stations are all installed on barren ground and lower vegetation. Barren ground includes blockfield and bedrock. Site specific temperature measurements in forests and on mires in Norway are sparsely distributed and consist only of data from MTD-loggers. Therefore, air/ground temperature studies carried out in Canada (Taylor 1995, Karunaratne and Burn 2004) and Alaska (Jorgenson and Kreig 1988, Klene et al. 2001) are used as a supplement to determine *n*-factors for these surface cover classes (Appendix B.1). The parameterization of *n*-factors is given in Table 2. A map showing the spatial distribution of nT-factors is included in Appendix D.6. A map of *nT* for the last normal period (1981-2010) is included in Appendix D.5.

***nF* – factors** - Ground surface temperatures in areas with barren ground (including bedrock, blockfields and not vegetated areas) are closely related to mean annual snow depth. 13 *i*-button stations were installed during the CRYOLINK project, measuring daily snow depth next to the air/ground-stations (Figure 15) (Hipp 2010). Since only snow depth is measured at the *i*-button stations, density and height of the snow were measured at all stations 4^{th} -7^{th} March 2011. Density values calculated for each location are presented in Appendix B.2. The snow height was close to maximum when the measurements were conducted and the snow pack was still dry. Under the assumption that inter annual snow density variations are minor, snow density measured in 2011 was used to relate the snow depths measured in 2008/2009 and 2009/2010 to snow water equivalent (*swe*). Based on these data a relation between *swe*

and *nF* is established (Figure 16), and is used to parameterize *nF*-factors for areas of barren ground (Table 2).

Snow depths above treeline are typically overestimated in the SeNorge snow maps. This is partly due to inversion effects occurring in certain regions, since the snow depth maps are derived from *swe* and air temperature data. Nevertheless, the total amount of snow in a grid cell is normally well reproduced in SeNorge (Engeset et al. 2004). To account for wind drift effects resulting in redistribution of snow over the edges of mountain summits and filling hollows in the terrain (Pomeroy and Gray 1995, Pomeroy et al. 1997), snow depth above treeline for areas with barren ground is reduced by 20%. One of the main thermal effects in blockfields are the high thermal conduction through rocks penetrating the snow cover (see Chapter 1), and therefore the isolating effect of the snow is significantly reduced in cases with a discontinuous snow cover. The degree of snow cover discontinuity is determined by the relation between surface roughness (mainly the size of the boulders) and thickness of the snow cover. The variation of surface roughness in block fields are unknown, and a constant *nF* of 0.85 is assigned to block fields of annual mean snow depth (*AMSD*) of less than 0.35m.

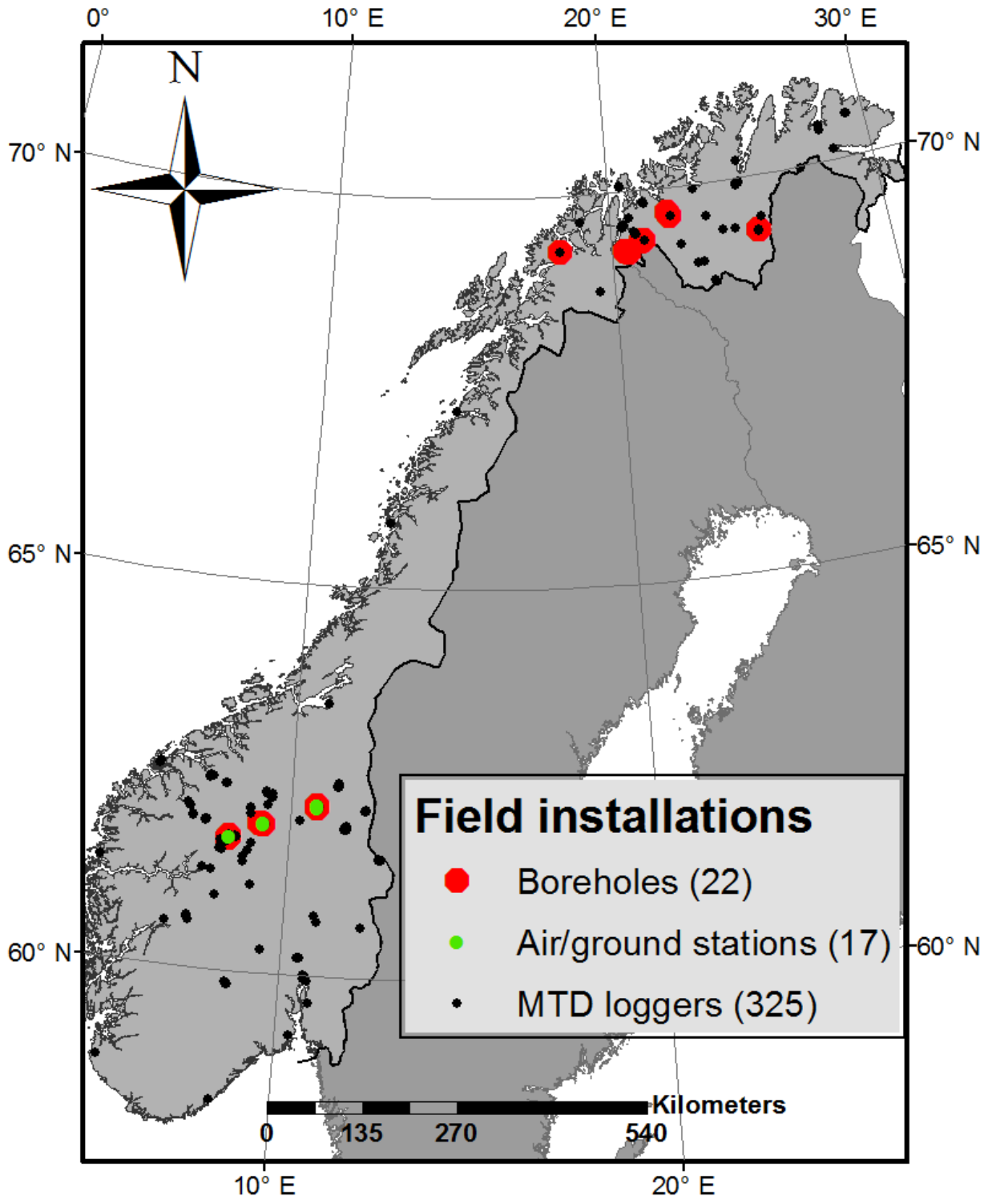

Figure 15: CRYOLINK field installations.

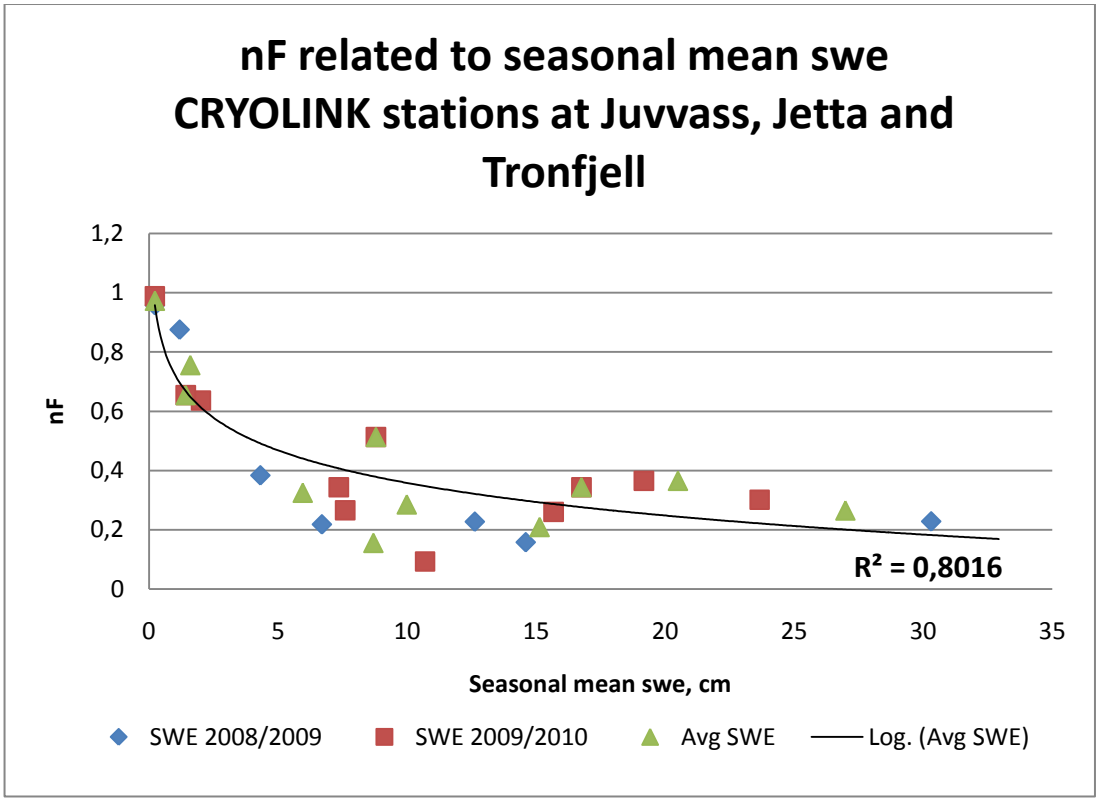

Figure 16: Correlation of nF-factors and seasonal mean snow water equivalent measured at the CRYOLINK air/ground and i-button stations. The trendline is *y = 0.72 - 0.16ln(x).*

Table 2: n-factor parameterization used in the CryoGRID-TTOP model.

	***AMSD* (cm)**	**Forest**	**Vegetated**	**Mires**	**Blockfield**	**Barren Ground**
nT	all	0.9	1.00	0.85	1.00	1.00
nF	all	0.3	0.3	0.60		
	< 5				0.85	0.95
	5 - 10				0.85	0.7
	10 - 15				0.85	0.6
	15 - 25				0.85	0.5
	25 - 35				0.85	0.4
	35 - 45				0.37	0.37
	45 - 55				0.35	0.35
	55 - 65				0.33	0.33
	> 65				0.3	0.3

4.2.2 Thermal effects of snow and surface vegetation cover – CryoGRID-mKA

In CryoGRID-mKA the effect of snow cover during winter season and thermal effect of vegetation cover during winter and summer seasons are treated separately.

Snow effect – The effect of snow cover on air temperature amplitude (ΔA_{sn}) and air temperature (ΔT_{sn}) is calculated as follows (Sazonova and Romanovsky 2003):

$$\Delta A_{sn} = A_a \left(1 - e^{-2H_{sn}\sqrt{\frac{\pi C_{sn}}{\tau K_{sn}}}}\right) * \frac{\tau_1}{\tau} \tag{4.1}$$

$$\Delta T_{sn} = \frac{2}{\pi} \Delta A_{sn} \tag{4.2}$$

A_a is the mean annual air temperature amplitude, H_{sn} is the height of snow cover, C_{sn} is the heat capacity of snow cover, K_{sn} is thermal conductivity of snow cover and τ and τ_1 is the length of the year and the winter season respectively. Height, density and thermal conductivity are derived from annual mean snow depth and snow water equivalent data based on the gridded snow SeNorge data. As in the TTOP-model, annual mean snow depth above treeline is reduced by 20%. Specific heat capacity of the snow cover does not vary in space in the model, and is assigned a constant value of 2009 $Jkg^{-1}K^{-1}$(Hock 2005). Volumetric heat capacity (C_{sn}) is calculated from the mass heat capacity and average density of the snow cover. Average snow density (ρ_{sn}) is calculated as:

$$\rho_{sn} = \frac{AMSWE}{AMSD} * \rho_w \tag{4.3}$$

based on annual mean snow water equivalent (*AMSWE*), annual mean snow depth (*AMSD*) and density of water (ρ_w).

Snow depths in forested areas are higher than average, and the snow density are lower. This is due to very little wind drift, and therefore little packing of the snow (Dingman 2002, Lied and Kristensen 2003). The snow data from SeNorge are not adjusted due to forest and

vegetation cover. Forested areas will in general have a lower density, and are therefore reduced by 20% in the CryoGRID-mKA model. This is validated with values from birch forests in Finnmark. Finnmark is known to have widespread permafrost in all non-forested areas (Isaksen et al. 2008). Birch forests are restricted to non-permafrost areas (e.g. Pèwè 1966, Dingman and Koutz 1974, Fukui et al. 2008), and are therefore used to adjust the reduction of snow density in the model. Conductivity values (K_{sn}) are calculated from density values using the empirical relationship between snow density and conductivity described by Sturm et al. (1997):

$$K_{sn} = 0.138 - 1.01\rho_{sn} + 3.233{\rho_{sn}}^2 \{0.156 \leq \rho \leq 0.6\} \quad (4.4)$$

$$K_{sn} = 0.023 + 0.234\rho_{sn} \{\rho < 0.156\} \quad (4.5)$$

where ρ_{sn} is snow density given in g cm^{-3} and K_{sn} is thermal conductivity of the snow cover given in Wm^{-1}K^{-1}.

Vegetation effects – The thermal effects of surface vegetation cover during winter (τ_1) and summer (τ_2) are estimated from height (H_{vg}, m) and thermal diffusivity in frozen (D_{vf}, m^{2}s^{-1}) and thawed (D_{vt}, m^{2}s^{-1}) states of the surface vegetation cover. The dampening of the air temperature amplitude (ΔA_v) and the air temperature (ΔT_v) due to surface vegetation cover are calculated as follows (Sazonova and Romanovsky 2003):

$$\Delta A_v = \frac{\Delta A_1 \tau_1 + \Delta A_2 \tau_2}{\tau} \quad (4.6)$$

$$\Delta T_v = \frac{\Delta A_1 \tau_1 - \Delta A_2 \tau_2}{\tau} \frac{2}{\pi} \quad (4.7)$$

τ is the period of the annual temperature cycle expressed in seconds. ΔA_1 and ΔA_2 is calculated as follows:

$$\Delta A_1 = \left(A_{vg} - T_{vg}\right) * \left(1 - e^{-H_{vg}\sqrt{\frac{\pi}{D_{vf} 2\tau_1}}}\right) \quad (4.8)$$

$$\Delta A_2 = (A_a - T_a) * \left(1 - e^{-H_{vg}\sqrt{\frac{\pi}{D_{vt} 2\tau_2}}}\right) \quad (4.9)$$

Diffusivity data for surface vegetation has been provided by the *Geophysical Institute Permafrost Laboratory, University of Alaska, Fairbanks (GIPL)*. Diffusivity data and

height of vegetation were assigned to vegetation classes in the CLC2000 vegetation map. Diffusivity and height for each vegetation class are given in Table 3.

Table 3: Thermal diffusivity and height related to the different vegetation classes in the CORINE2000 vegetation map. The data are provided by the Geophysical Institute in Fairbanks.

	Vegetation class	Height (H_{vg}, m)	Diffusivity thawed (D_{vt}, 10^{-6} m^2s^{-1})	Diffusivity frozen (D_{vf}, 10^{-6} m^2s^{-1})
211	Agriculture	0.15	1.55	1.55
231	Fields and meadows	0.15	1.55	1.55
242	Mixed cultivated land	0.15	1.55	1.55
243	Sparse cultivation	0.15	1.55	1.55
311	Deciduous forest	0.13	1.48	1.52
312	Coniferous forest	0.01	1.06	0.11
313	Mixed forest	0.14	0.65	1.74
322	Shrubs	0.15	1.55	1.55
324	Clearcut forest	0.25	1.87	1.02
331	Beach and sand dunes	0	0	0
332	Bedrock	0	0	0
333	Sparsely vegetated areal	0.15	1.55	1.55
411	Wetlands	0.10	0.12	0.68
412	Mires	0.10	0.12	0.68
423	Tidal plaines	0	0	0
	Blockfield	0	0	0

4.3 The thermal offset

Similar algorithms are used to model the thermal offset in the two equilibrium models. While the mKA-model uses thermal conductivity in thawed (K_t) and frozen (K_f) states directly, the TTOP-model utilizes the ratio of thermal conductivity in thawed and frozen ground (r_k). Both models are based on the same conductivity data. In addition the mKA-model uses volumetric heat capacity of frozen ground (C_f) as input data. A map showing the spatial distribution of r_k-values is included in Appendix D.7.

The subsurface material data is a combination of the petrophysical dataset provided by NGU, sediment property data provided by University of Alaska, Fairbanks *(GIPL),* and data from the literature. The thermal conductivity values for thawed and frozen states, estimated from the NGU data, are calculated as geometric mean of thermal conductivity in dry sediment and water (0.57 $Wm^{-1}K^{-1}$) and ice (2.1 $Wm^{-1}K^{-1}$) respectively. Approximate water contents are

assigned to each subsurface material class. Sediment thermal conductivity and heat capacity data from GIPL are also assigned to the different classes in the subsurface material cover map. The different physical property values are described below.

4.3.1 Parameterizing of soil property data

Bedrock – thermal conductivity values for dry bedrock are provided from NGU and are illustrated in Figure 14, c. Bedrock has very low water content, estimated to be 1%. This will give r_k–values close to unity. Because of solar radiation at bedrock during the summer season, there are very high *nT*-factors at bedrock sites (up to 1.6). Since bedrock is included in the barren ground class containing all areas without vegetation, the very high thermal offset could not be reproduced in the *nT*-factor. Instead, the r_k for bedrock is increased by 5%. This adjustment has no physical basis, and in further improvements of the model bedrock should be treated as a separate surface cover type with a higher *nT*. C_f has a constant value of 2.0×10^6 $Jm^{-3^\circ}K^{-1}$.

Blockfields and weathered material – The thermal regime in blockfields is not controlled by thermal conductivity primarily, and a model including all heat transfer effects through openwork blockfield is too complex to include in a regional model. The depth of the openwork blockfield and the proportion of the active layer controlled by non-conductive heat transfer vary to a high degree, and are difficult to map. The boreholes drilled in blockfields during the CRYOLINK project show blockfield depths of 1-3 meters (Farbrot et al. submitted). In most cases the active layer or freezing depth are greater than this. Normally there is a gradual, vertical transition from boulders to bedrock within blockfields. Areas of blockfields in the blockfield map described in Chapter 4.3.3 are therefore assigned average thermal conductivity values based on conductivity values of the underlying bedrock, with 0.1% water content. C_f is assigned a value of $2.16*10^6$ $Jm^{-3^\circ}K^{-1}$.

Sediment classes and moraine deposits – all sediment classes in the subsurface material map provided by NGU are allocated thermal conductivity and heat capacity values from GIPL (Table 4). Areas of thin sediment cover are given bedrock values adjusted for slightly higher water content.

Table 4: Heat capacity and thermal conductivity values in thawed and frozen ground, in addition to volumetric water content of the ground are assigned to the different subsurface material classes in the NGU-map.

	Sediment class	Ct *10^{-6} ($Jm^{-3}K^{-1}$)	Cf *10^{-6} ($Jm^{-3}K^{-1}$)	K_t ($Wm^{-1}K^{-1}$)	K_f ($Wm^{-1}K^{-1}$)	ϑ_w	R_k
11	Glacier till, thick	2.2	2.0	1.52	1.87	0.36	**0.81**
14	Ablation moraine	2.3	1.8	1.47	2.13	0.33	**0.69**
15	Glacier till, marginal moraine, very thick	2.2	2.0	1.52	1.87	0.36	**0.81**
16	Drumlin	2.0	2.0	1.91	1.92	0.21	**1.00**
21	Glacial-fluvial, terraces	2.2	1.8	1.54	1.86	0.52	**0.96**
30	Glaciolacustrine, glacial river	2.0	1.9	1.97	2.05	0.25	**0.74**
40	Sea, fjord deposits, marine	2.3	1.8	1.41	1.97	0.35	**0.72**
41	Sea, fjord deposits, marine	2.3	1.8	1.41	1.97	0.35	**0.72**
42	Marine beach deposits	2.2	1.8	1.46	1.73	0.42	**0.84**
43	Marine beach deposits	2.2	1.8	1.46	1.73	0.42	**0.84**
54	Flod deposits	2.1	1.7	1.65	1.99	0.40	**0.83**
60	Aeolian deposits	2.1	2.0	1.98	2.01	0.10	**0.99**
73	Weathering material, block fields, coarse material	2.4	1.9	1.96	2.16	0.17	**0.91**
80	Gravitational material, not specified	2.1	2.0	1.83	2.15	0.31	**0.85**
81	Gravitational material, below steep slopes	2.5	1.9	1.96	2.16	0.17	**0.91**
82	Gravitational material, below steep slopes	2.5	1.9	1.96	2.16	0.17	**0.91**
	Thin sediment classes:						
12	Glacier till, thin	2.2	2.0	2.13	2.35	0.08	**0.90**
55	Flod deposits, thin	2.1	1.7	1.78	2.04	0.1	**0.87**
72	Weathering material, thin	2.4	1.9	2.20	2.29	0.03	**0.96**
88	Gravitational material, thin	2.4	1.9	1.40	1.36	0.03	**0.99**
	Organic material:						
90	Organic material, mires	4.0	1.6	0.6	1.1		**0.55**
100	Organic material, thin	4.0	1.6	2.0	2.7	0.2	**0.76**
	Bedrock:						
130	Bedrock, no sediment cover if larger areas	2.0	2.1	From NGU data		0.1	**1.05**
140	Bedrock, no sediment cover if larger areas	2.0	2.1	From NGU data		0.1	**1.05**
	Blockfields:	2.0	2.16	From NGU data		0.1	**0.95**

Organic material – Data for organic materials are based on values from Williams and Smith (1989). Areas classified as mires in the subsurface material map are assigned thermal conductivity values of 0.6 and 1.1 $Wm^{-1}K^{-1}$, and volumetric heat capacity of 4 and $1.6*10^6$ $Jm^{-3}°K^{-1}$ in thawed and frozen states, respectively. The water content is 0.2 (Table 4). Areas

of a thin layer of organic materials are assigned similar heat capacities, but higher thermal conductivity values of 2.0 and 2.7 $Wm^{-1}K^{-1}$ are used.

The calculated conductivity values are compared to conductivity values measured in 28 boreholes distributed over northern and southern Norway (Christiansen et al. 2010, Farbrot et al. submitted) as well as to the conductivity values used in the TONE model implemented for the Mackenzie River Valley in Canada (Wright et al. 2003). These comparisons are described in Chapter 6.3.3.

5. Model results

Results from the TTOP-model and the modified Kudryavtsev's model implemented for Norway are presented in this chapter. An equilibrium scenario over the last normal period, 1981-2010, is chosen to describe the present day permafrost situation. Chapter 5.1 contains an overview of the contemporary state of permafrost in Norway, modelled with the two CryoGRIDeq-models. Special emphasis is given to the CRYOLINK and TSP key sites; Finnmarksvidda (Iskoras), inner Troms, Tronfjell and Jotunheimen, containing extensive field data. An extensive list of maps is included in Appendix D, containing the three normal periods since 1960; 61-90, 71-00 and 81-10 (D.1-4).

5.1 Present permafrost distribution in Norway

The equilibrium situation over the last normal period, 1981-2010 is presented in Figure 17. Total permafrost area is 20 614 km^2, corresponding to 6.4% of the Norwegian mainland area (Table 5). 34% of the permafrost area is in till, 23% in blockfields, 19% in mires and 17% in bedrock. A small proportion of these permafrost areas contain vegetation. Figure 24 depicts a large area of permafrost in Troms and Finnmark, and a smaller area of permafrost in the mountains of Southern Norway; Jotunheimen and Rondane. The permafrost in Troms, Gaissane and southern Norway are primarily mountain permafrost. More lowland permafrost is scattered all over Finnmarksvidda, and there is also large areas of potential palsa mires. In southern Norway the palsa mires are mainly found on Dovre and in the mountains on each sides of Gudbrandsdalen. The equivalent map modelled with the mKA-model is included in Appendix D.4.

Figure 18 a) to h) depict selected key sites; two in northern Norway and two in southern Norway. The key sites are chosen with respect to borehole locations in the CRYOLINK and TPS projects. The relative temperature distribution pattern is very similar between the two models for all areas, but the mKA-model gives more extreme temperatures with overall colder *MAGT* at higher elevated areas and warmer in lower areas. This results in a larger total area of permafrost.

Table 5: Distribution of permafrost presented as a fraction of total area, and subsurface material classes expressed as a fraction of total permafrost area. Values are based on the TTOP-model run for 1981-2010 (Figure 17).

	km²	%
Area mainland Norway	323782	
Total permafrost area	20614	6.4 %
Total permafrost area, mires excluded	16605	5.1 %
Subsurface material classes:		
Till (11,15,21)	6990	33.9 %
Blockfields	4659	22.6 %
Mires (90)	4009	19.4 %
Bedrock (12,72,130,140)	3597	17.4 %
Ablation moraine (14)	672	3.3 %
Weathering material (73,81,82)	671	3.3 %
Marine deposits (30,41)	13	0.1 %
Organic material, thin (100)	3	0.0 %
Vegetation classes:		
Barren ground	13793	66.9 %
Mires	6515	31.6 %
Forest	272	1.3 %
Lower vegetation	34	0.2 %
No data	0	0.0 %

A clear difference between western and eastern permafrost limits can be observed from transects crossing Jotunheimen in Southern Norway (Figure 19, upper). Both Galdhøpiggen and Glittertind have a degrading permafrost limit towards the eastern side of the mountains. The Jotunheimen area has a lower permafrost limit of approximately 1700 meters a.s.l. on the western side, and 1400 meters a.s.l. on the eastern side. Lower permafrost is mapped down to 1200 meters on Ringebufjellet, and in Femundsmarka, southeastern Norway, permafrost occurs down to 900m a.s.l. A similar east-west permafrost gradient is found in northern Norway (Figure 19, lower). The altitudinal limit for continuous permafrost is 1200 meters a.s.l. at Sommerfjellet in Troms and 700 meters on the eastern side of the mountains in Finnmark. On Finnmarksvidda the transect shows sporadic permafrost down to 400 meters. None of the areas mapped as permafrost in these transects are located on mires.

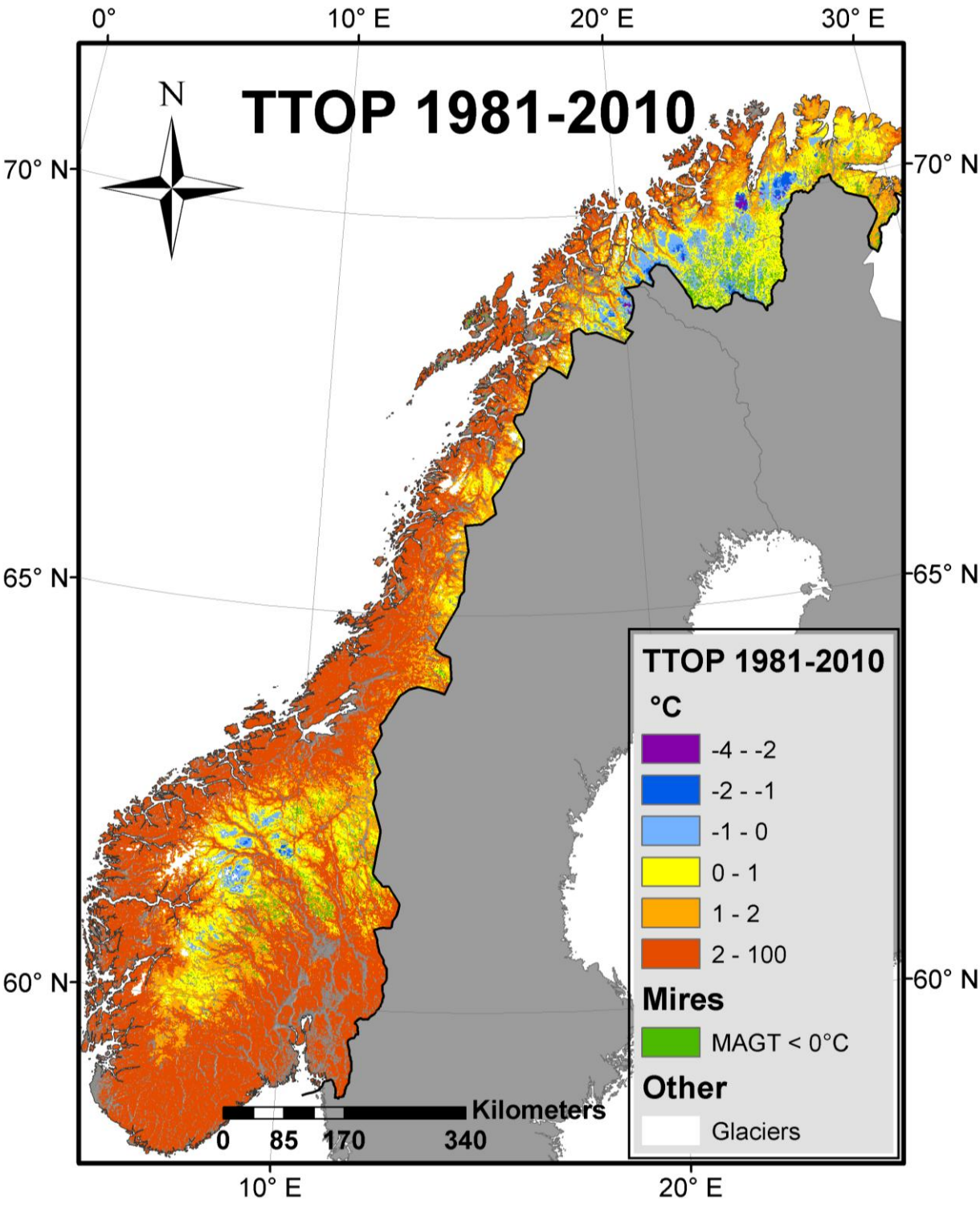

Figure 17: Permafrost distribution in Norway over the normal period 1981-2010, modelled with CryoGRID-ttop. Mean annual ground temperatures (MAGT) below zero degrees centigrade are given in blue colors, and indicate permafrost areas. Red colors are used for non-permafrost areas. The green color shows areas of mires with MAGT below zero; these are areas of potential palsa mires.

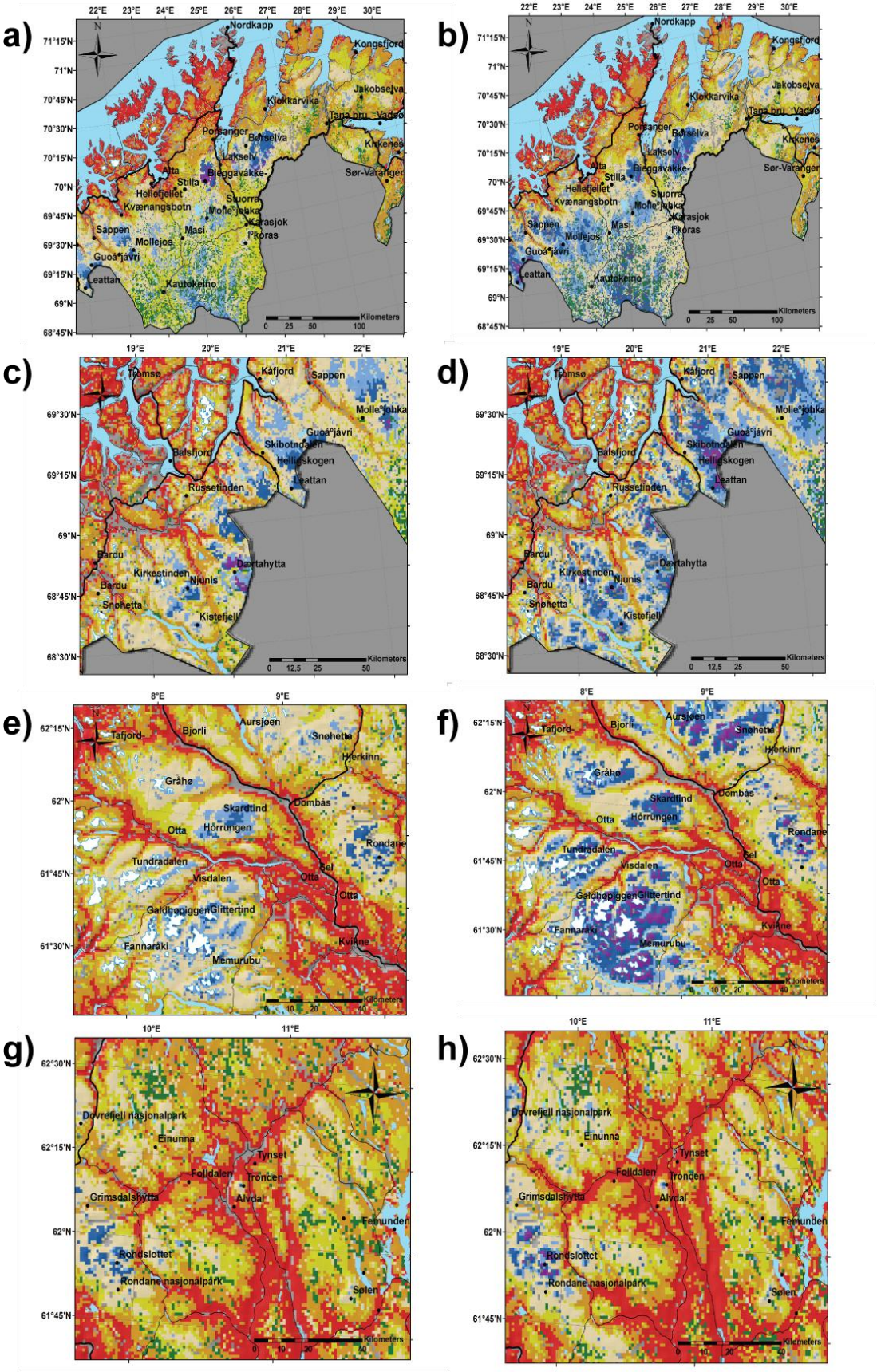

Figure 18: Maps showing permafrost at the CRYOLINK key sites modelled with the TTOP-model (left) and the mKA-model (right). Legend is equivalent to Figure 17.

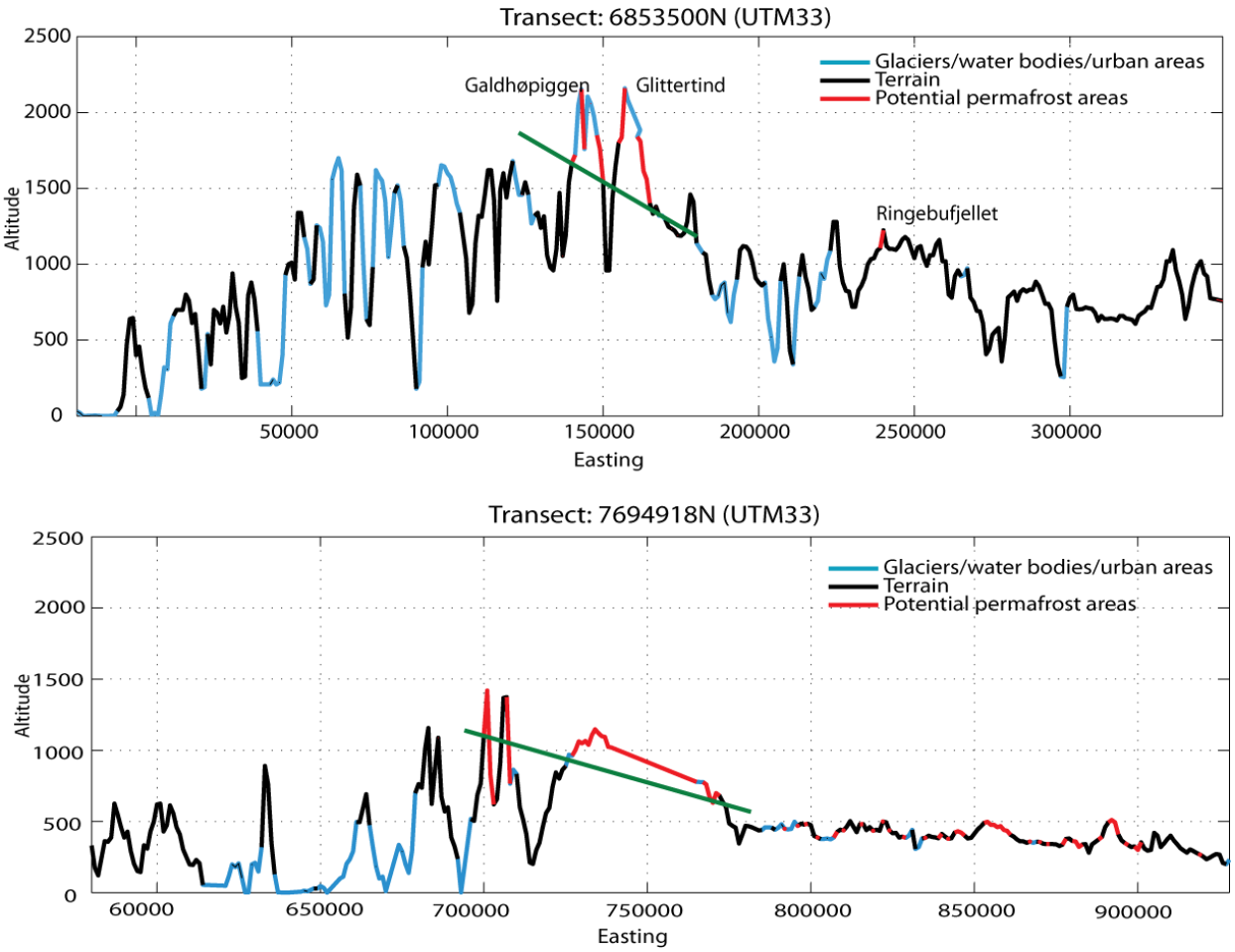

Figure 19: West - east transects showing permafrost occurrence distributed on elevation and distance from the west coast. Upper transect shows Jotunheimen including Glittertind and Galdhøpiggen, and crosses over Ringebufjellet towards east. The lower transect crosses inner parts of Troms and Finnmarksvidda.

5.2 Active layer thickness and permafrost depth

In addition to *MAGT*, several other characteristics of permafrost can be determined from the CryoGRIDeq-models:

***MAGST* -** Mean annual ground surface temperature, which is necessary to produce the *MAGT* has been determined for northern and southern Norway, as illustrated in Figure 20 a and b. Areas with *MAGST* < 0°C has light blue to purple colors. These areas correspond relatively well with the modelled permafrost areas, but there are exceptions. In some areas the ground temperatures are warmer, while in other areas the thermal offset is large so that there are still permafrost with *MAGST* > 0°C.

ALT - The active layer thickness (ALT) and the seasonal frost depth (SFD) can be calculated based on ground surface temperatures and conductivity data in the ground surface layer, here estimated using the Stefan solution presented in Chapter 2.3.2. ALT and SFD is here combined in one map (Figure 20, c and d), where ALT is given in positive values (red), while SFD is given in negative values (blue). All depths are given in meters. ALT varies from 0.5 to 2 m in areas with organic material, while ALT depths down to 10 m are estimated for blockfield and bedrock areas. Estimated depth of seasonal frost is mainly in the range of 0 to 4 meters. However, some areas, such as the Varanger peninsula in Finnmark, have a remarkably deeper frost penetration (Figure 20, c). This is attributed to very cold winter temperatures combined with a dry climate, and can additionally be explained by the high quartz content in the ground.

Permafrost depth –Permafrost depth for a ground thermal regime in equilibrium state is estimated from *MAGT*, thermal conductivity in bedrock and geothermal heat flux. Permafrost depth, based on *MAGT* from the period 1981-2010, is presented in Figure 20, e and f. This illustration does not necessarily reflect present ground temperature regimes, but describes an equilibrium situation with present surface temperatures. Permafrost depth for most areas varies between 10 and 75 meters. However, in some regions (Gaissane in Finnmark, Njunis in Troms and Rondane in Southern Norway) the depth of permafrost reaches over 200 meters. At Juvvass in Jotunheimen the model estimates a permafrost depth of 75 meters.

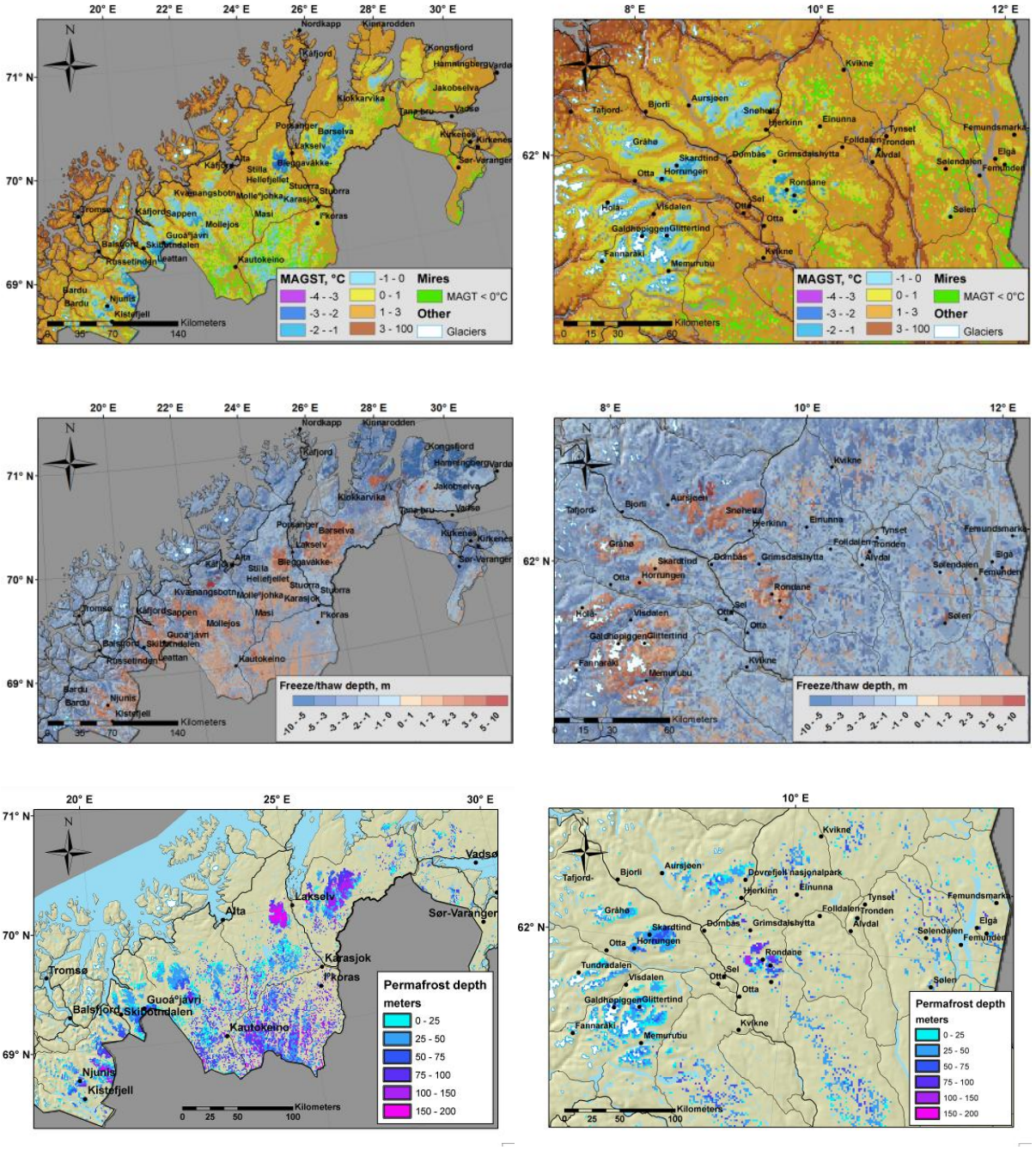

Figure 20: MAGST (a and b), ALT (c and d) and permafrost depth (e and f) modelled with the TTOP-model for a chosen area in Troms and Finnmark (left) and central southern Norway (right).

6. Model evaluation and sensitivity

Results from the two models have been compared to different sources of data; (1) *MAGST* from miniature temperature data (MTD) loggers, (2) *MAGT* from borehole data, (3) BTS-maps for the key sites, and (4) distribution maps of palsa mires and permafrost landforms (Chapter 6.1 - 6.4). The model sensitivity of both CryoGRIDeq-models is examined with respect to meteorological factors and ground thermal properties (Chapter 6.5).

6.1 Evaluation of *MAGST*

6.1.1 MTD-loggers

MAGST is compared to data from 74 MTD-loggers distributed throughout Norway (Figure 15). In this instance, the use of point measurements for validation is problematic because of high sub-grid variability, even at resolutions of 1km^2. Similar validation issues are also observed when considering *MAGST*, mainly due to large variations in snow depth and ground water content. These problems have been overcome by including only MTD-loggers representing the general snow cover thickness of the grid cell and similar vegetation cover. Scatter plots between measured and modelled *MAGST* are shown in Figure 22, a) and b). Both the TTOP-model and the mKA-model show a strong correlation between measured and modelled *MAGST* (both with R^2 of 0.75). The mKA-model has, in general, lower and more extreme *MAGST*, while the TTOP-model tends to smooth out the temperature variations. This is likely due to less vegetation classes in the TTOP-model combined with snow depth values discretized to *nF*-classes.

6.2 Evaluation of *MAGT*

6.2.1 Borehole data

Measured and modelled *MAGT* from borehole locations all over Norway are presented in Table 6. The overall correlation between the TTOP-model and the measured data is relatively good, having a RMS of 0.75°C and a R^2 of 0.45. The mKA-model has a larger RMS due to overall colder temperatures. However, at some locations the mKA-model is warmer; such as at the Doverpals site, Lavkavagge BH1 and Trond BH3. The mKA additionally tends to give

warmer temperatures for mires. This is also the case for blockfields, which are not modelled explicitly in the mKA-model.

Table 6: Measured and modelled MAGT from the two models for all TSP and CRYOLINK boreholes in Norway are shown in the table below. The difference in temperature is shown in the two right columns.

	Measured *MAGT*	TTOP	mKA	Error TTOP	Error mKA
Abo BH1	-0.42	0.23	0.01	0.65	0.43
Abo BH2	1.05	0.70	0.58	-0.35	-0.46
BH31/PACE31	-2.39	-0.92	-1.87	1.47	0.52
Dovrepals	-0.36	-0.51	-0.07	-0.15	0.30
Guol BH1	-0.06	0.04	-0.48	0.10	-0.42
Guol BH2	0.00	-0.06	-0.61	-0.06	-0.61
Guol BH3	0.89	-0.09	-0.35	-0.98	-1.24
IskBH1	-0.25	-0.87	-1.20	-0.62	-0.95
IskBH2	-0.26	-0.87	-1.20	-0.60	-0.94
Jet-BH1	-0.43	0.48	0.46	0.91	0.89
Jet-BH2	0.96	0.53	0.35	-0.44	-0.62
Jet-BH3	1.34	1.33	1.31	-0.01	-0.03
Juv-BH1	-1.92	-0.95	-1.83	0.97	0.09
Juv-BH2	-0.55	-0.95	-1.83	-0.41	-1.29
Juv-BH3	-0.36	-0.27	-0.77	0.09	-0.41
Juv-BH4	-0.61	-0.27	-0.77	0.34	-0.16
Juv-BH5	0.89	-0.27	-0.77	-1.16	-1.66
Juv-BH6	0.78	0.88	0.17	-0.90	-1.61
Kistefjellet	0.69	0.90	0.74	0.21	0.05
Lavka BH1	0.34	0.29	0.03	-0.05	-0.31
Lavka BH2	1.64	1.37	0.41	-0.26	-1.23
Lavka BH3	1.60	1.09	--	-0.51	--
NoBH1	0.80	1.69	1.75	0.89	0.95
NoBH2	-0.06	0.51	0.26	0.58	0.32
NoBH3	-0.91	0.51	0.26	1.43	1.17
Tro-BH1	0.01	-0.32	-0.65	-0.32	-0.66
Tro-BH2	0.77	-0.32	-0.65	-1.09	-1.42
Tro-BH3	1.25	0.10	0.13	-1.15	-1.12
RMS				**0.75**	**0.90**
R^2				**0.45**	**0.28**

6.2.2 BTS-maps

MAGT modelled from the two CryoGRIDeq-models are compared to BTS-maps from Juvvass, Dovre (Isaksen et al. 2002), Tronfjell (CRYOLINK), Sølen and Elgåhogna (Heggem et al. 2005) (Figure 21, a-g). These are CRYOLINK key sites with well known permafrost patterns due to several MTD-loggers, BTS-measurements and boreholes. The BTS-maps are based on a high number of BTS-measurements taken over repeated winter seasons. All figures show a colder temperature regime modelled with the mKA-model, while both models have a very similar distribution pattern. The slightly warmer TTOP-model shows a very good correlation with the BTS-probability maps both for Juvvass and at Dovre. In the eastern and continental areas in Femundsmarka, containing the key sites Elgåhogna and Sølen, the mKA-model reproduces the permafrost pattern better than the TTOP-model. Both models have problems reproducing the permafrost distribution in this area, especially at Elgåhogna, and both models are warmer than the BTS-map. The very cold scattered grid cells correlates well to the distribution of mires. It is likely that some of the mires might contain permafrost, but in general the modelled distribution of cold mires in this area is too large. One reason why the permafrost pattern is not reproduced at Elgåhogna is that the large areas of openwork blockfields at the mountain are not mapped in the blockfield map. The TTOP-model uses an *nF*-factor of 0.7, indicating a shallow snow cover, and limited vegetation cover. This suggests that the permafrost distribution is limited to blockfields in this area.

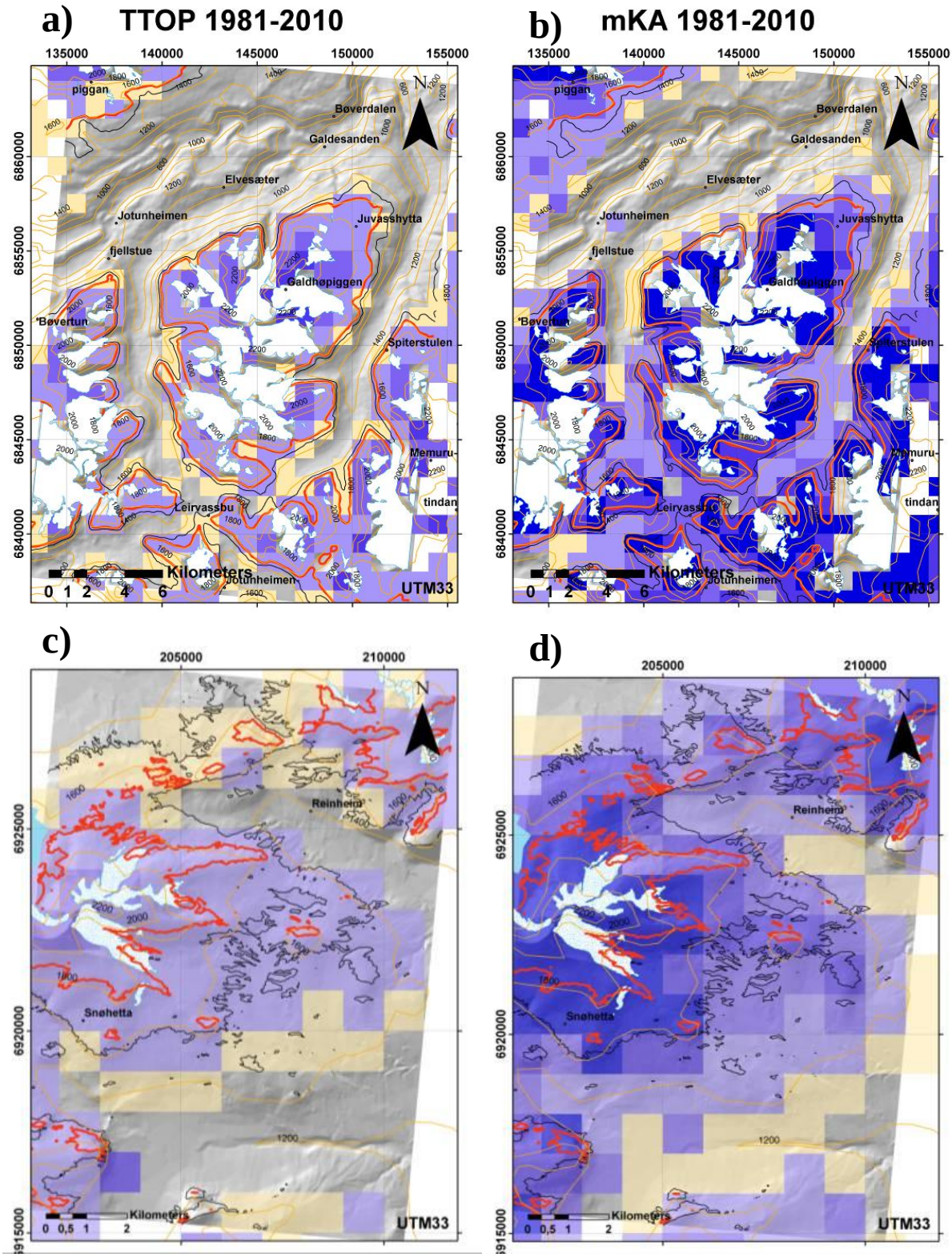
a) TTOP 1981-2010
b) mKA 1981-2010
c)
d)
piggan
Bøverdalen
Galdesanden
Elvesæter
Jotunheimen
Juvasshytta
fjellstue
Galdhøpiggen
Bøvertun
Spiterstulen
Memurutindan
Leirvassbu
Reinheim
Snøhetta
Kilometers
UTM33

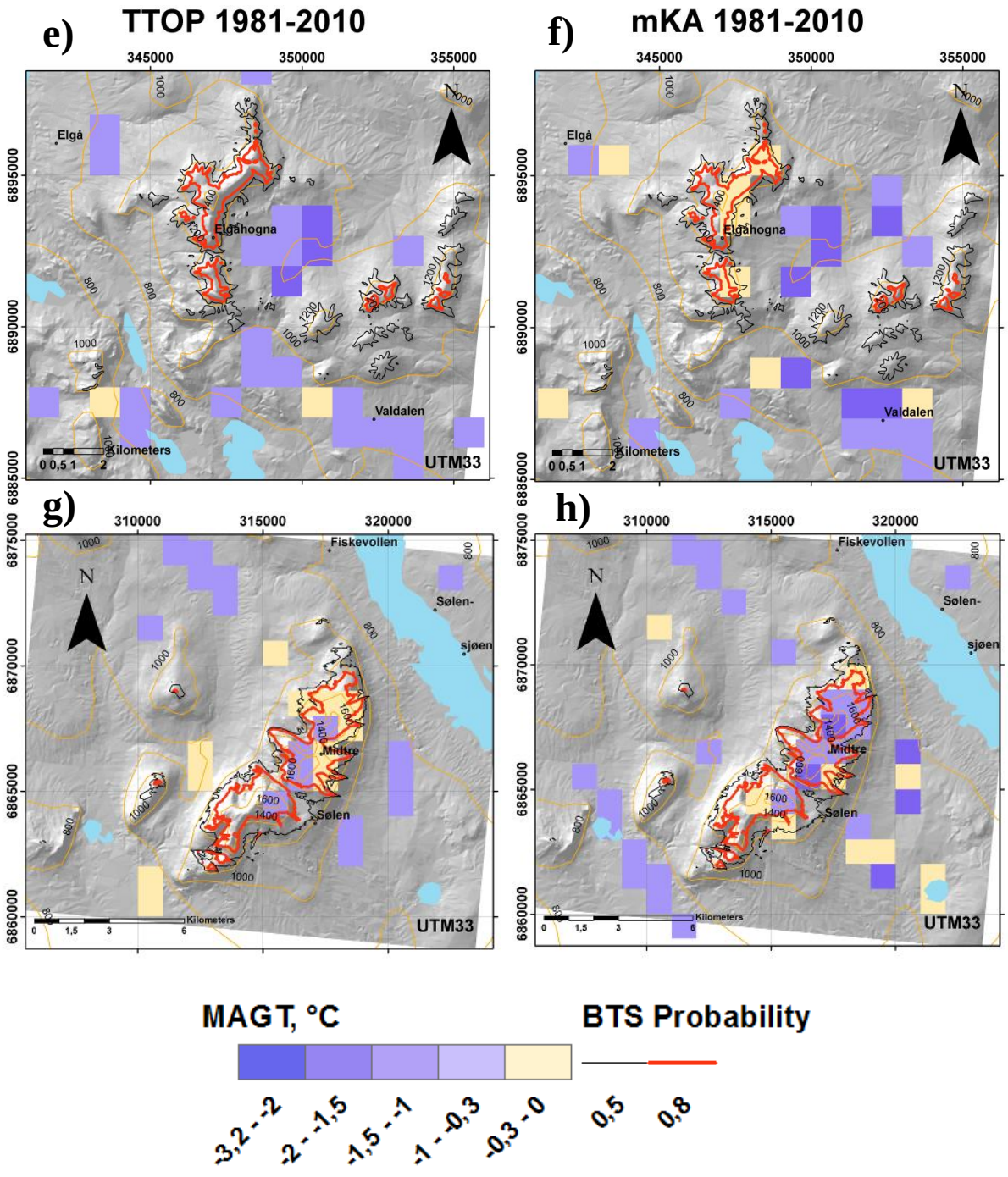

Figure 21: TTOP (left) and mKA (right) MAGT values compared to BTS probability maps based on BTS measurements published earlier in Isaksen et al. (2002) and Heggem et al. (2005) for selected sites in southern Norway. Juvvass: a and b. Dovre: c and d. Elgåhogna: e and f. Sølen: g and h. Only areas with MAGT below 0°C are included.

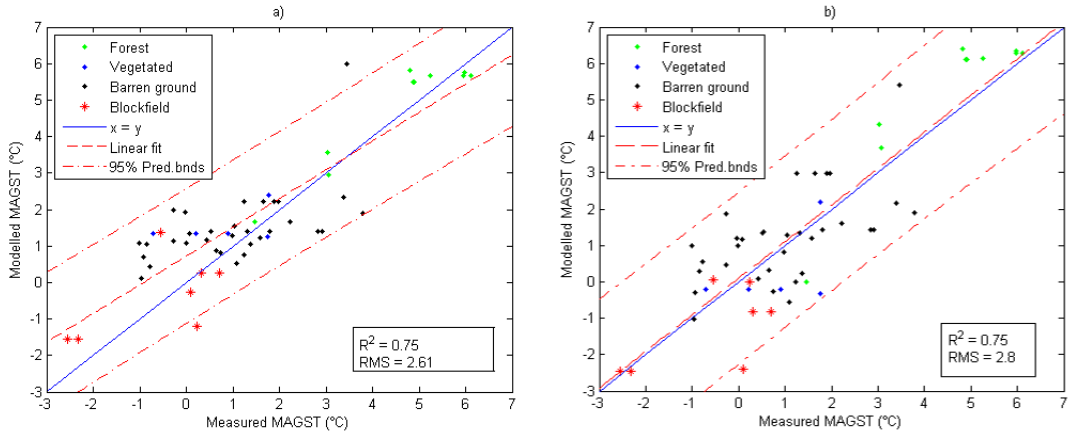

Figure 22: Scatter plots for measured and modelled MAGST. Measured values are based on 74 MTD-loggers, and are plotted along the x-axis. Modelled values are plotted on the y-axis, for the TTOP-model in the left plot (a) and for the mKA-model to the right (b).

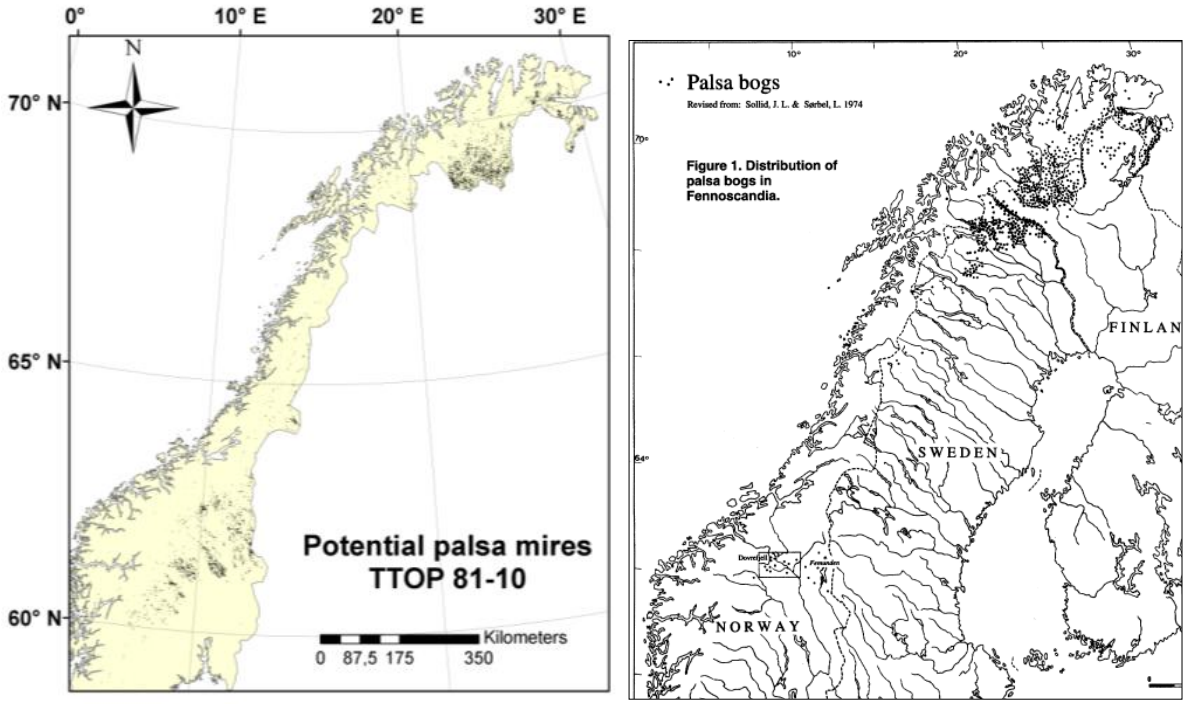

Figure 23: Left: Distribution of potential palsa mires modelled with the TTOP-model for 1981-2010. Right: Mapped palsa bogs based on several studies both at UiO (Sollid and Sørbel 1974, Sollid and Sørbel 1998) and NINA, Norsk institutt for naturforskning (Hofgaard 2003).

6.2.3 Distribution of palsas, rock glaciers and ice cored moraines

Based on a study of permafrost landforms (Lilleøren and Etzelmüller in prep), the correlation between the permafrost distribution mapped with the TTOP-model and permafrost landforms such as rock glaciers and ice cored moraines for Southern Norway are interpreted. The permafrost map for 1981-2010, with permafrost landforms included (Figure 24), shows a clear correlation between intact permafrost landforms (dark blue, green and red circles) and present permafrost distribution (blue colors) in the Jotunheimen and Horrungane area.

Figure 23, left shows the distribution of mires with *MAGT* below 0°C, which can be considered to be areas of potential palsa mires. The map shows a large concentration of palsa mires on Finnmarksvidda and along the Russian border. This is consistent with the map by Sollid and Sørbel (1974) (Figure 23, right), which is based on field observations.

6.3 Model sensitivity

In the following chapter the TTOP-model is examined for sensitivity due to changes in snow cover thickness, variation in vegetation cover and alteration in the thermal conductivity of the ground.

6.3.1 Sensitivity to snow cover

MAGT is most sensitive to changes in snow depth in areas of shallow snow cover, especially less than 20cm annual mean snow depth (*AMSD*), see Figure 26. Few areas in Norway have *AMSD* of less than 20cm (Appendix D.10). Considering permafrost areas, only Finnmarksvidda has less than 20cm *AMSD*. A belt in Finnmark and Troms has 20-30 cm of snow, while no permafrost areas with barren ground in southern Norway have less than 30cm *AMSD*. Continental areas with long, cold winters, and thus a high number of freezing degree days are the most sensitive areas to variations in snow cover (Figure 26). These areas often coincide with regions of a thin snow cover, where a variation in *AMSD* of 20cm will result in a 3°C change in *MAGT*. However, the topography is more homogenous in these areas, resulting in less spatial variation in snow depth. Assuming an annual mean snow depth variation of 20cm, the contribution from snow to the total uncertainty in *MAGT* is less than Δ1°C for most continental areas, and less than Δ0.6°C for more maritime areas.

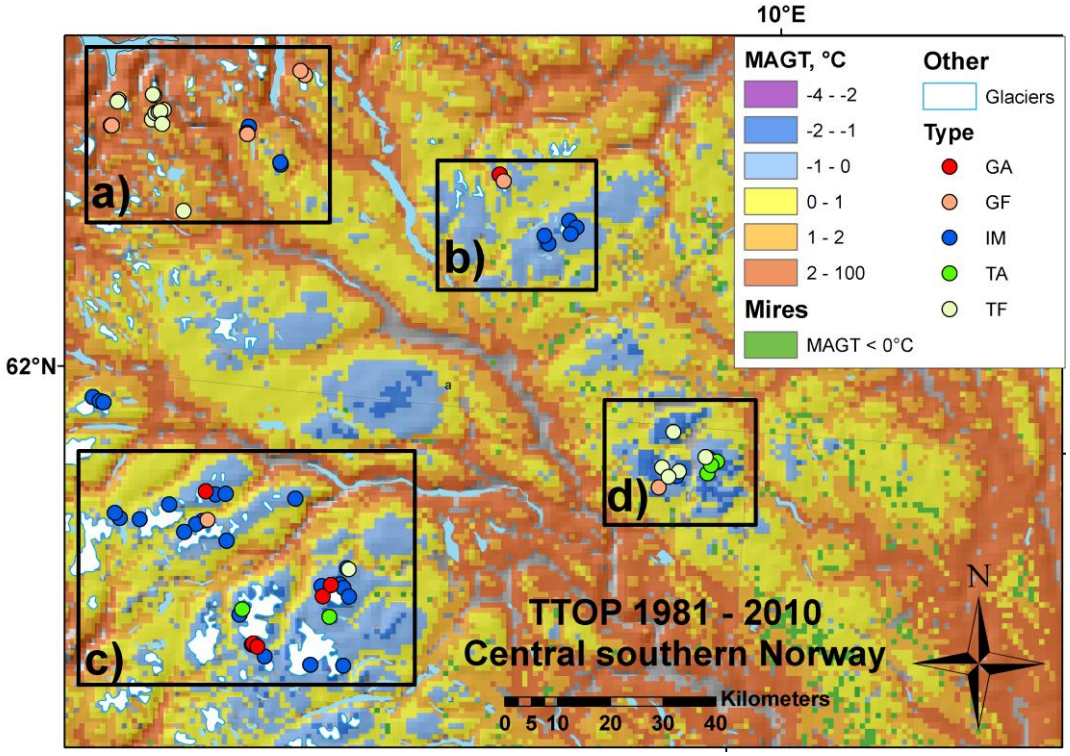

Figure 24: The permafrost map for southern Norway compared to mapped intact and relict permafrost landforms, including rock glaciers and ice cored moraines.

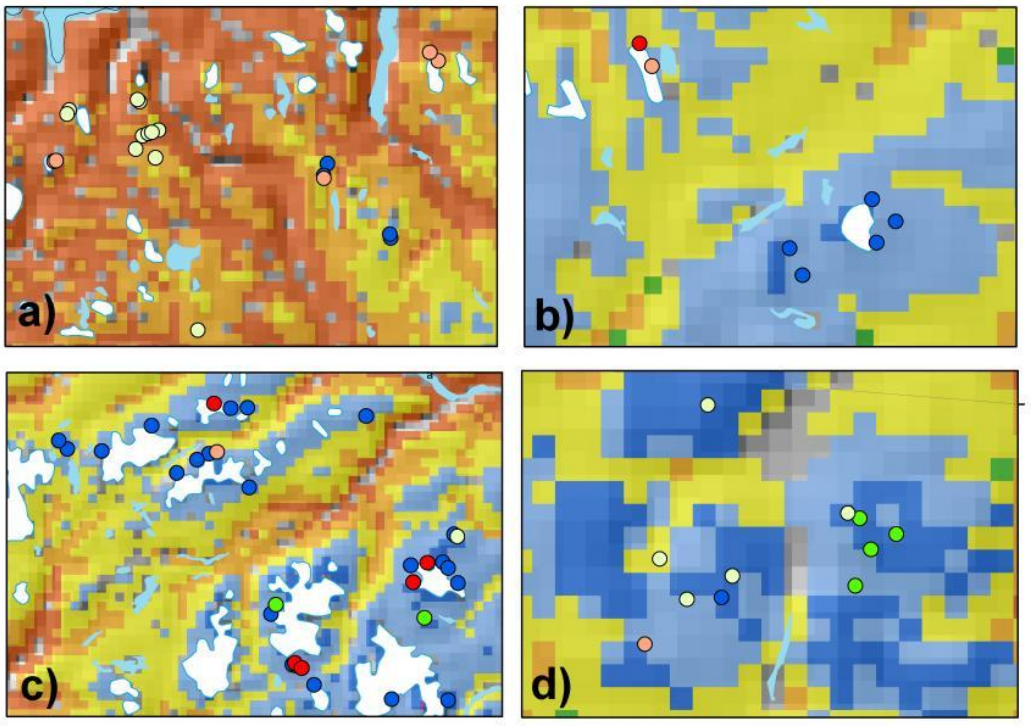

Figure 25: The correlation between intact rock glaciers/ice cored moraines and permafrost is very good for all areas of such landforms in southern Norway; a) Romsdalen, b)Dovre, c) Jotunheimen, and d) Rondane. The colorbar is the same as in Figure 24.

The total variation in *AMSD* within a grid cell will often be larger than 20cm, especially in areas with heterogeneous topography where snow accumulates in hollows (Hauck et al. 2004). Because of lateral heat flow, the ground temperature at a certain depth will be influenced by temperatures from a horizontal area at the ground surface with a diameter corresponding to the depth. When the snow patches are small (diameter< active layer thickness) they are of less importance to *MAGT*.

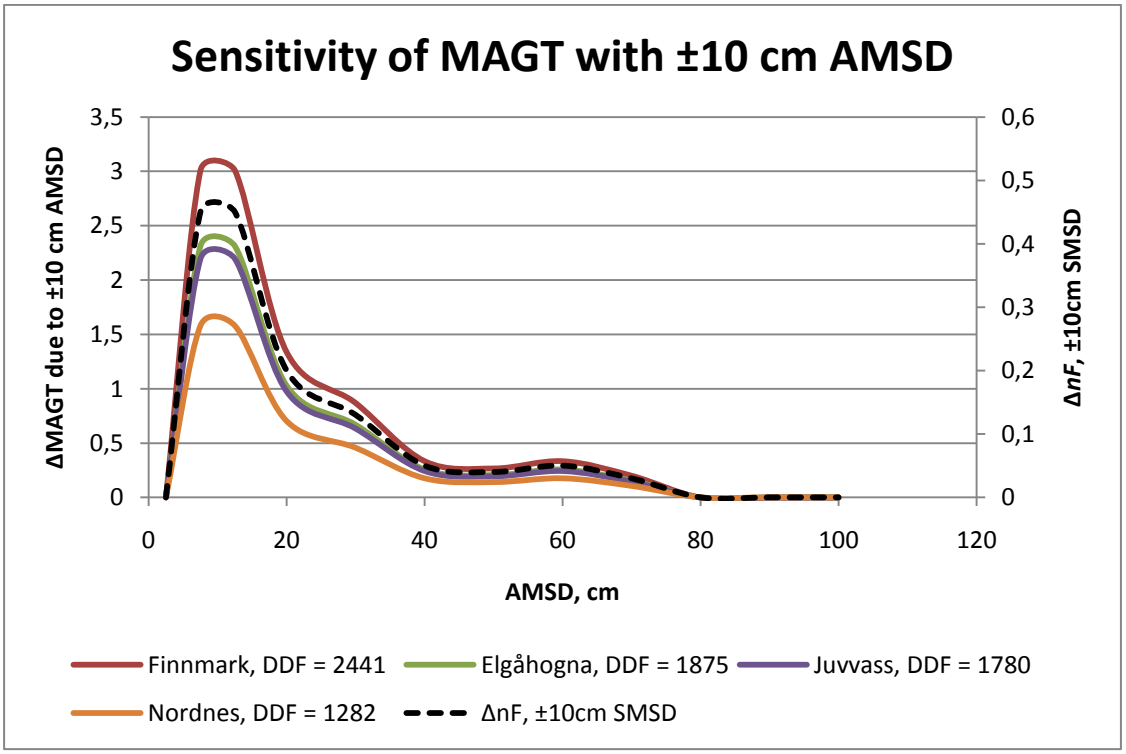

Figure 26: Sensitivity of MAGT in relation to snow depth and continentality. The graph shows the deviation in MAGT due to a 20 cm uncertainty in annual mean snow depth.

6.3.2 Sensitivity in *MAGT* due to surface cover

The sensitivity of *MAGT* due to vegetation can be divided in two groups. First, the sensitivity between vegetation classes related to wrong vegetation classification and sub-grid mixing of vegetation classes, here called inter-class variations. Second, the sensitivity to variation in *nT* within each vegetation class, called intra-class variation. Both inter- and intra variations are discussed below.

The sensitivity of *MAGT* due to change in surface cover is primarily related to *nT*-factors. However, *nF* for forest, lower vegetation, and mires are also determined by the surface cover,

and there is also a relationship between type of surface cover and the thermal conductivity of the active layer.

Inter-class variation - Sensitivity in *MAGT* due to inter-class variation are examined in Table 7, a) and b). The table shows the deviation in *MAGT* between vegetation classes, when *nF* and r_k-values are fixed within each vegetation class. Table 7 a) shows sensitivity in a continental area with *TDD* = 1000°C days year^{-1}, and *AMSD* of 20cm, while table b) shows sensitivity in a more maritime climate with *TDD* = 580°C days year^{-1},, and a *AMSD* of 50cm. Sensitivity of *nT* is related to r_k, where a lower r_k will give lower sensitivity of *nT*. r_k for bedrock, blockfield and mires are fixed values in the model, while r_k in forests and areas of lower vegetation vary with subsurface material. In this sensitivity study, r_k for forest and lower vegetation is fixed to the average r_k-value in permafrost areas of each class. By comparing Table 7 a) and b) it is clear that the sensitivity of *nT* is much higher in continental climates, due to the higher number of both thawing and freezing degree days and thus higher energy exchange. For continental areas, such as Finnmarksvidda, the largest deviation in *MAGT* (Δ 3.6°C) is reached between areas of forest and lower vegetation and areas of no vegetation. This is due to the large effect of vegetation cover during winter season. The deviation in *MAGT* between non-vegetated classes is within Δ2.0°C. For more maritime climates the sensitivity is much reduced. Inter-class mixing for all classes give a deviation in *MAGT* of less Δ0.4°C except for the mires class, which has a deviation of around Δ2.0°C.

Table 7: The table shows ΔMAGT between vegetation classes in a) a continental climate, and b) a maritime climate. r_k within each class is fixed, and snow depth and degree days are fixed within each climatic setting. Sensitivity to vegetation classes increases with continentality, and the classes of highest sensitivity varies much from continental to maritime setting.

a)	Barren ground	Blockfields	Mires	Forest	Vegetated
Barren ground	0.0	2.0	1.6	1.3	1.6
Blockfields	2.0	0.0	0.4	3.3	3.6
Mires	0.4	0.4	0.0	2.9	3.2
Forest	3.3	3.3	2.9	0.0	0.3
Vegetated	3.6	3.6	3.2	0.3	0.0
b)	**Barren ground**	**Blockfields**	**Mires**	**Forest**	**Vegetated**
Barren ground	0.0	0.2	1.8	0.2	0.4
Blockfields	0.2	0.0	2.0	0.0	0.2
Mires	2.0	2.0	0.0	2.0	2.1
Forest	0.0	0.0	2.0	0.0	0.2
Vegetated	0.2	0.2	2.1	0.2	0.0

Intra-class variation is related to variation of *n*-factors inside each vegetation class. The intra-class sensitivity is more difficult to quantify. Parameterization is done based on several field observations, and there is a range in measured *n*-factors for the different classes. The variations in measurements from air/ground stations and MTD-loggers coupled to gridded air temperature data from SeNorge are illustrated in Figure 27 and Table 8. Only MTD-loggers representing the average snow cover of the corresponding grid cell are included in the statistics.

nT for all classes have a lower variation than *nF* in both A/G-stations and ground surface MTD-logger data. The average values for each class is nearly identical in the two data sets (Table 8). In general the barren ground class has the largest variation. This is particularly apparent when considering *nF*. The high variation in *nF* is in accordance with the theory that the surface offset during summer is controlled by snow cover in non-vegetated areas. The larger variation in *nT* for barren ground, ranging from 1 to 1.25 (ΔnT of 0.25) within the 25th to 75th percentiles might be a result of direct sunlight on the temperature logger, as exposure is harder to avoid in areas of barren ground. Considering the fact that barren ground includes both sediment covered areas, bedrock and blockfields, the variation is minor. *nT* values for forest, vegetation and mires are very consistent, with less than 0.1 variation in *nT*. This is less than expected, as these classes are anticipated to have a larger variation in soil moisture than the barren ground class. The variation in *nF* is larger for lower vegetation than for forest, because snow cover will have a greater effect on the thermal offset and also because there is a larger range of vegetation densities within the class. 50% of the *nF*-values for lower vegetation are in the range of 0.3 to 0.5 at the air/ground stations, and from 0.1 to 0.5 in the ground surface MTD-logger data. It might be considered to relate *nF* for lower vegetation to snow depth on the basis of the present data, however no clear relationship is observed. ΔnF for mires are within 0.15.

Uncertainty of MAGT due to variation of *n*-factors within each surface cover class is listed in Table 9 - *TDD* are 580 °C day year^{-1}, and FDD are 1750 °C day year^{-1}. Uncertainty due to intra-class variations in *nT* are very low for all classes (<0.32°C), while higher for *nF*; up to 1.44°C for lower vegetation.

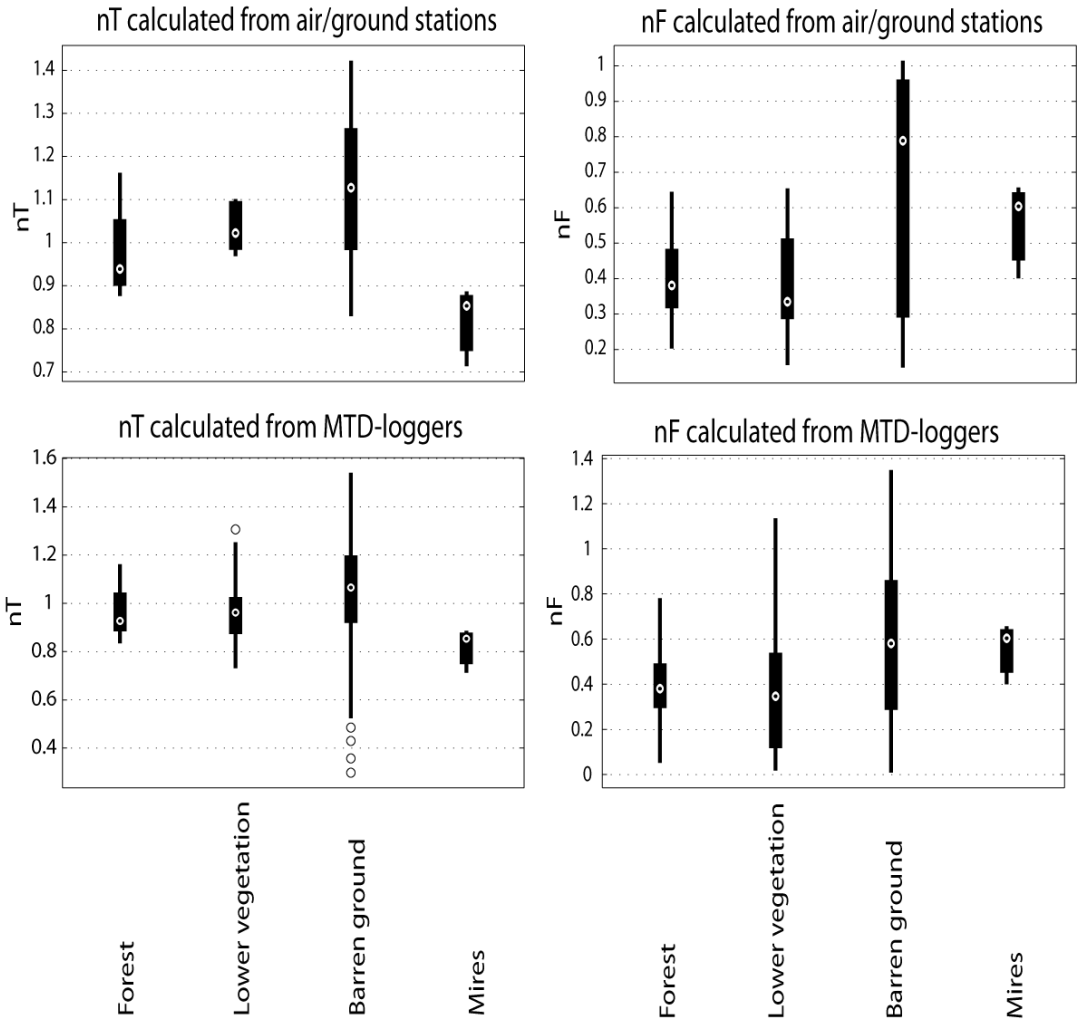

Figure 27: The figure shows the variation of n-factors in each surface class. The central mark is the median, and the edges of the boxes are the 25th and 75th percentiles. The whiskers extend to the most extreme data points the algorithms considers not to be outliers. Outliers are plotted individually.

Table 8: Average n-factors (Avg) for each surface class based on air/ground stations (upper) and MTD-logger (lower) are given in the table below. Std is the standard deviation in nT/nF within each surface class.

	Air/ground stations				
		Forest	**Lower vegetation**	**Barren ground**	**Mires**
nT	*Avg*	0.99	1.03	1.13	0.82
	Std	0.11	0.06	0.18	0.09
nF	*Avg*	0.40	0.38	0.66	0.55
	Std	0.13	0.18	0.34	0.14
	MTD loggers				
nT	*Avg*	0.96	0.97	1.03	0.82
	Std	0.11	0.15	0.25	0.09
nF	*Avg*	0.40	0.36	0.58	0.55
	Std	0.20	0.26	0.33	0.14

Table 9: Uncertainty of MAGT temperatures due to inter-class variation in n-factors.

	Δ*nT*	**Δ*nF***	**Δ*MAGT* due to *nT***	**Δ*MAGT* due to *nF***
Barren ground	0.25		0.32	
Mires	0.1	0.2	0.09	0.72
Forest	0.1	0.2	0.14	0.96
Vegetated	0.1	0.3	0.14	1.44

6.3.3 Sensitivity to r_k

The ratio between thermal conductivity in thawed and frozen ground is defined as r_k. Thus, the sensitivity of the thermal offset is determined by the water content. Thermal conductivity values are calculated taking the geometric mean of the conductivity of the constituents. This gives thermal conductivity values closely related to water content. Bedrock and blockfields have a r_k-value close to 1.0 due to very low water content (<3%), which exhibits minor spatial and temporal variation. Sediments have higher and more varying water contents, resulting in r_k-values ranging from 0.7 to 1 depending on the type of sediments. Water content will vary more in space in relation to topography, aspect and sediment, and therefore higher sub-grid variabilities in r_k for sediments than for bedrock are expected. The water content in mires varies both spatially and temporally, r_k in mires must be expected to vary from 0.3 to 0.8 (Smith and Riseborough 2002). In the model mires have a fixed water content of 30% corresponding to an r_k of 0.55. This implies that the uncertainty in r_k for mires is very high.

Sensitivity of *MAGT* due to change in r_k is examined in Figure 28 for areas with nT =1 (barren ground and vegetation). Forested areas and blockfields have nT = 0.9, decreasing the sensitivity of r_k. However, this is not studied further here. The dark grey line shows sensitivity in areas with warm summers (*TDD* = 1000°C day year^{-1}) and the light grey line in areas of cooler summers (*TDD* = °C day year^{-1}). The graph shows a linear relationship between change in r_k and change in *MAGT*, where $\Delta MAGT \approx 2.74 * \Delta r_k$. Variation in r_k for bedrock is less than 0.1, introducing an uncertainty in *MAGT* of 0.27°C and 0.16°C for warm and cold summers respectively. Maximum variation in r_k for sediments are in the range of 0.7 to 1.0, giving a maximum variation in *MAGT* of 0.82°C and 0.48°C for warm and cold summers. Mires have a lower nT of 0.85, and are illustrated with dotted lines. Assuming a

maximum r_k-variation of 0.5 in mires implies a maximum variation in *MAGT* of 1.16°C and 0.68°C for cold and warm summers, respectively.

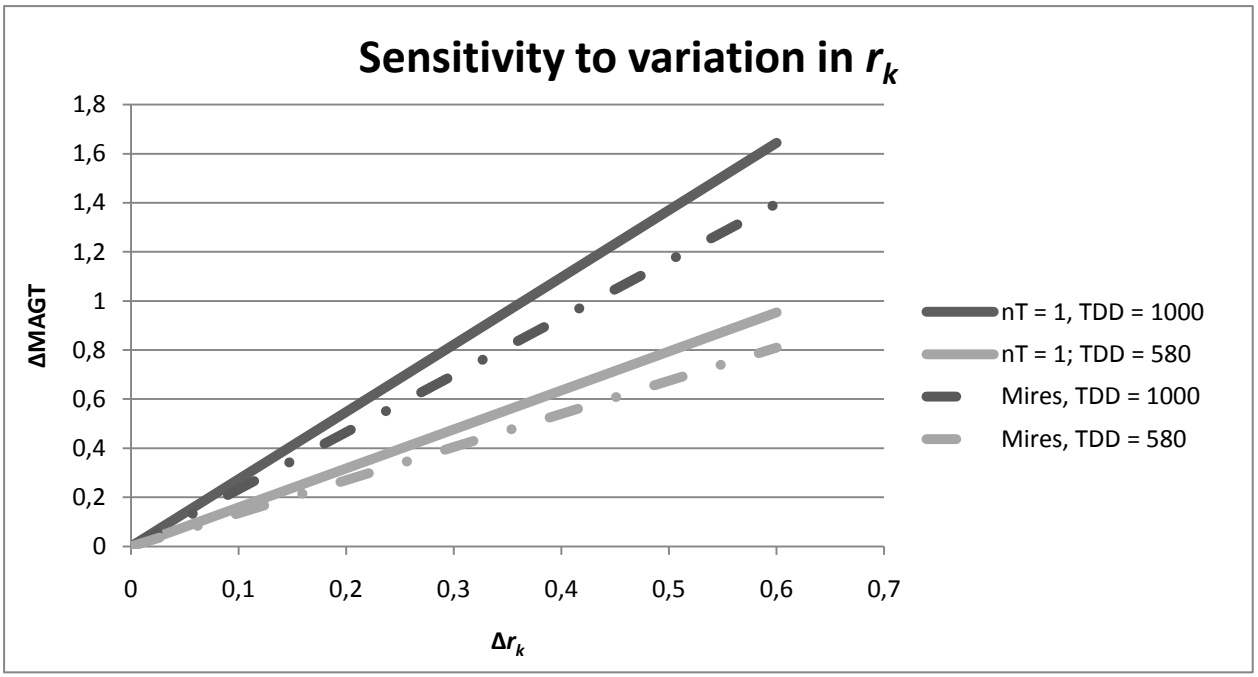

Figure 28: Sensitivity of MAGT due to change in rk when nT = 1 (hard lines) and nT = 0.85 (dotted lines). Dark colors are sensitivity in continental areas with 1000 TDD. Light grey line shows sensitivity when TDD = 580 °C day year^{-1}.

7. Examples of the application of CryoGRIDeq to past and future climate conditions

The TTOP-model is run based on reconstructed meteorological data for Holocene Climatic Optimum (HCO) and the Little Ice Age (LIA) (Chapter 7.1). A future climate scenario is also implemented, based on HIRHAM (downscaled Hadley A2 scenario) (Chapter 7.2). These scenarios are compared to today's permafrost distribution in the following chapter.

7.1 Holocene permafrost in Norway

The TTOP-model is forced with three Holocene scenarios; (1) last normal period (1980-2010), (2) LIA and (3) HCO. The LIA scenario is run with thawing and freezing degree days according to Lilleøren et al. (in prep). The snow model is run with 130% annual mean snow depth relative to the normal period 1960-1990 (Nesje et al. 2001, Matthews et al. 2005). The permafrost distribution for each period is illustrated in Figure 30.

LIA (250-500 B.P.) is the coldest period during Holocene, and according to Lilleøren et al. (in prep) the *MAAT* was 0.55°C compared to last normal period, and the temperature amplitude was 0.94°C and 1.1°C higher for southern and northern Norway respectively. The colder climate resulted in a pronounced glacier advance and a much lower altitudinal permafrost limit. According to the TTOP-model 47 024 km^2 was underlain by permafrost, corresponding to 14.5% of the total land area of mainland Norway. The increased glaciated area is not considered in these numbers. This is more than a doubling of present distribution.

HCO was the warm period ranging from roughly 8000 to 6000 B.P. According to Lilleøren (in prep) mean annual temperatures for southern Norway were +1.7°C and for northern Norway +1.9°C. Air temperature amplitudes were -1.8°C and -2.3°C for southern and northern Norway. An adjusted treeline map for HCO is produced based on reconstructed July temperatures, and included in the model run (Etzelmüller 2011). According to the model, the warmer climate resulted in a marked thaw of permafrost, with permafrost at only 1.1% of the total Norwegian mainland area, corresponding to 21.5% of present permafrost area. Permafrost that survived HCO is substantially older than the rest of the permafrost. The dating of permafrost on global scale has great relevance for emission projections of trapped

gasses in areas of degrading permafrost. Therefore, similar historical reconstruction would be of great impact if they can be implemented for larger areas beyond the Norwegian mainland.

Table 10: Climate adjustments for the little ice age and Holocene maximum based on Lilleøren et al. (in prep).

	LIA	Holocene max
Southern Norway		
***MAAT* (°C)**	-0.55	1.71
Amplitude (°C)	0.94	-1.84
DDT	-28	209
DDF	-173	484
AMSD	130%	
Northern Norway		
***MAAT* (°C)**	-0.55	1.91
Amplitude (°C)	1.1	-2.32
DDT	-40.15	209
DDF	-160.6	494.4

7.2 Future permafrost in Norway

A future permafrost scenario is run for the period 2071-2100. Downscaled gridded temperature data for 2071-2100 with same temporal and spatial resolution as the SeNorge data, are provided by the Norwegian meteorological institute (Engen-Skaugen et al. 2007). Maximum snow water equivalents (*maxSWE*) as single values averaged over the period 2071-2100 are provided by NVE (Beldring et al. 2006).

The temperature scenario is based on the regional climate model (RCM) HIRHAM (Engen-Skaugen et al. 2007, Engen-Skaugen et al. 2008) with lateral boundary forcing provided by HadAM3H from the Hadley centre. HadAM3H is a global medium resolution model, and is run with the IPCC emission scenario A2. The A2 scenario projects a 2.0 – 5.4°C temperature increase at 2090-2099 compared to 1980-1999, and is the second most extreme SRES scenario. Increase in winter temperatures in Norway varies from +3.0°C to +4.5°C and summer temperatures from +1.5 to +3.5°C (Engen-Skaugen et al. 2007). The HIRHAM downscaled for Norway is well documented in Engen-Skaugen et al. (2007).

Equivalent snow projections downscaled to 1km^2 do not exist for Norway, but a projection of annual *maxSWE* averaged over the period 2071 – 2100 is provided by NVE (Beldring et al. 2006). To utilize these data a relation between *maxSWE* and *nF* was established based on data from the air/ground and *i*-button stations. A relation between *maxSWE* and *nF* (Figure 5) was established by employing snow densities measured at the *i*-button stations in 2011 (described in Chapter 4.2.1). Discretized *maxSWE* and *nF*-values are shown in Table 11. Present treeline, blockfield distribution, vegetation cover and sediment cover are used in the future permafrost scenario.

According to the IPCC emission scenario A2 a pronounced warming is predicted for the coming century. This will have great impacts on the permafrost distribution, and according to the TTOP-model run for 2071-2100 permafrost will remain at only 0.2% of the total mainland area of Norway. Of this area 440km^2 is in mires, 75km^2 in blockfields and only 3km^2 in bedrock. Since the permafrost areas in mires probably are overestimated, it is likely that the total area of permafrost will be even smaller.

Table 11: nF-factors related to descretized maxSWE, based on the relationship in Figure 29.

max SWE	***nF***
< 0.05	1
0.05 - 0.1	0.7
0.1 - 0.15	0.55
0.15-0.2	0.45
0.2-0.25	0.38
0.25-0.3	0.35
0.3-0.35	0.32
0.35-0.45	0.31
> 0.45	0.3

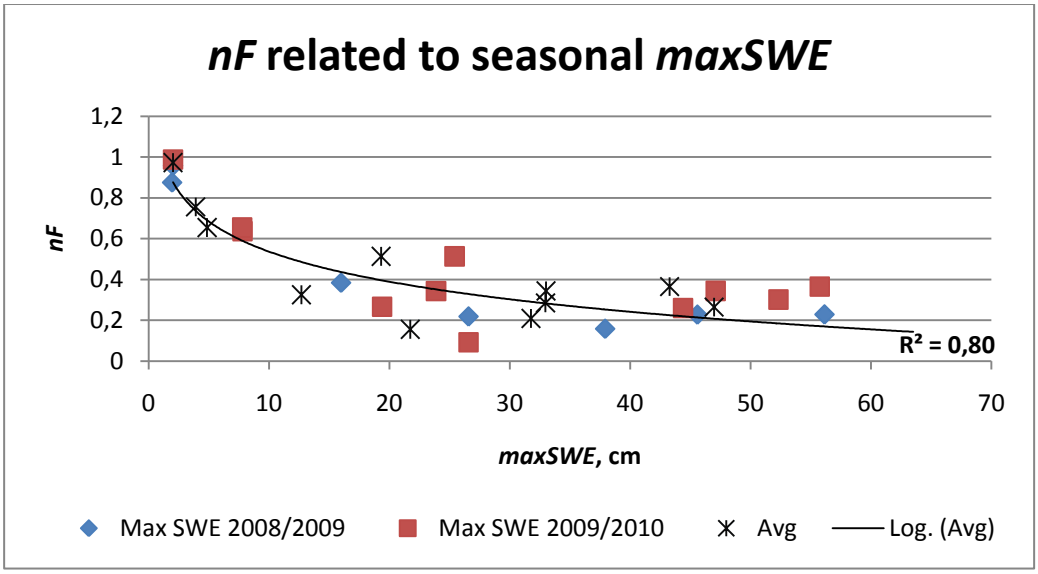

Figure 29: Relation between maximum snow water equivalent and freezing n-factors. The trend line is *y = 1,026 - 0,213ln(x).*

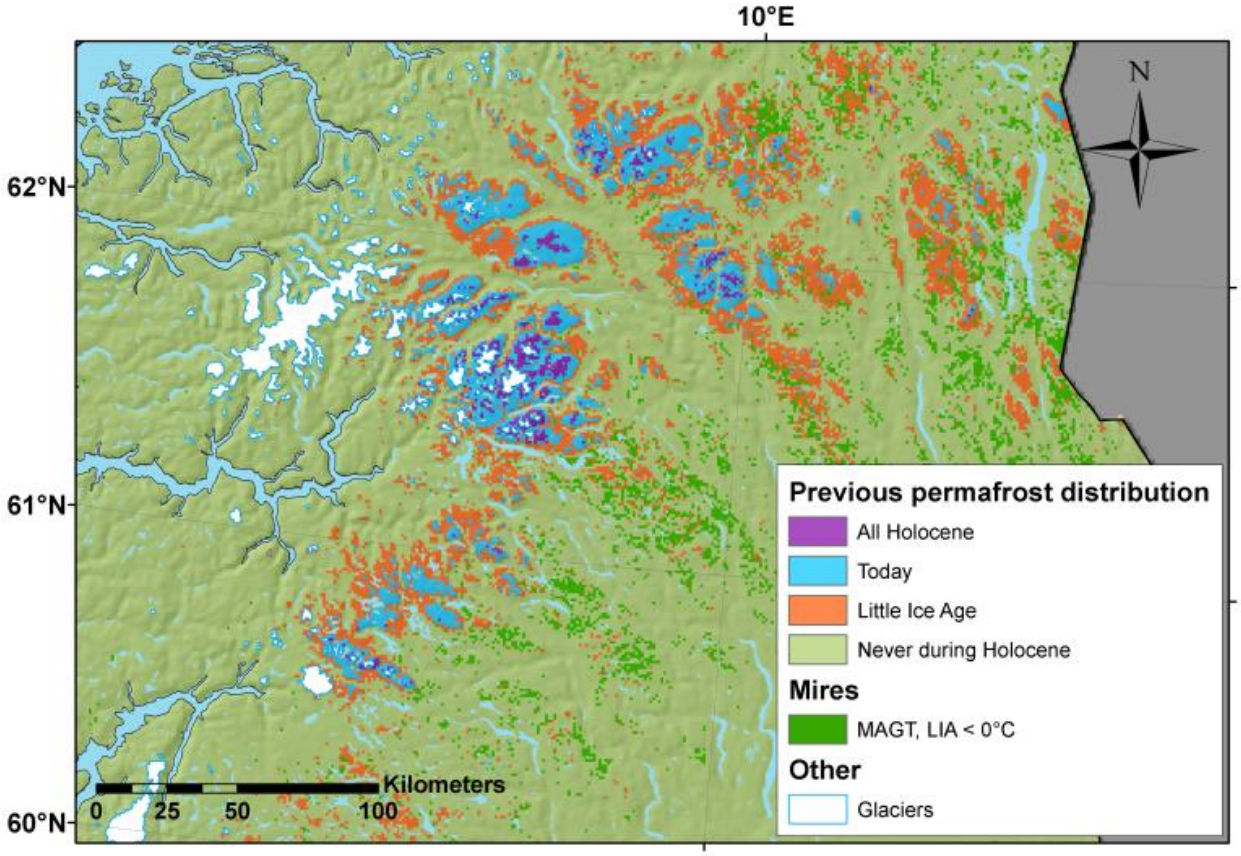

Figure 30: Paleo reconstruction of previous permafrost distributions in southern Norway during Holocene.

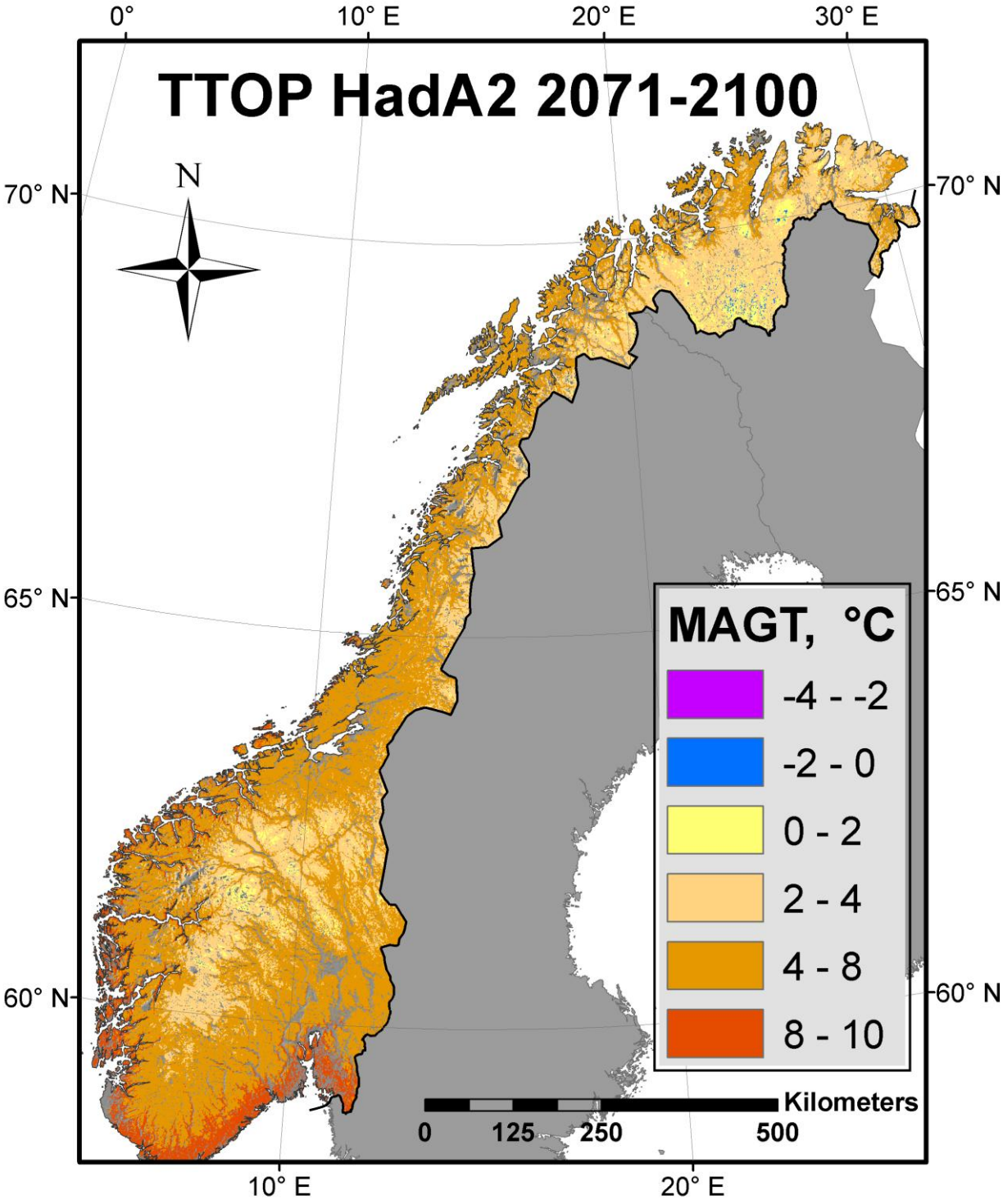

Figure 31: MAGT modelled with the TTOP-model for the future scenario 2071-2100, based on downscaled IPCC emission scenario A2 temperatures and maxSWE.

8. Discussion

This chapter gives a further discussion over model results and evaluation, and past, present and future permafrost distribution in Norway. Input data and parameterization of the models are discussed in the first two sections (8.1 and 8.2). The model results, mainly from the TTOP-model are evaluated in section 8.3, before a discussion of advantages and disadvantages with the two model approaches are given in section 8.4, and a discussion of sub-grid variability in section 8.5. An overview of the present permafrost distribution in Norway is outlined in section 8.6, before the historical and future scenarios are discussed in relation to future implications of a change in the permafrost thermal regime.

8.1 Input data

8.1.1 The SeNorge-data

CryoGRIDeq is run with daily air temperatures, snow depths and snow water equivalencies provided by SeNorge. The quality of the meteorological data is naturally related to the quality of the observations. The Norwegian topography is very complex and large parts of the area are at high elevations. Most of the population is located at lower elevations, along the coast or in the valleys. Since meteorological data is primarily recorded to predict weather in populated areas, there is a skew in the altitudinal distribution of stations compared to the altitudinal distribution of topography, as illustrated in Figure 32 (Tveito 2009). As shown, most stations are located below 400m a.s.l. while the majority of the topography is higher than 400m. This skew in altitudinal distribution results in a less accurate reproduction of temperature and precipitation data at higher elevations. Major inversion effects in the continental regions of Norway accentuate these errors (Tveito et al. 2000). The inversion effect is generally valid for areas above treeline, because these areas are above the unmixed cold air in the valley (Lewkowicz and Bonnaventure 2011). Situations with temperatures of -20°C in a valley located at 200m a.s.l. and temperature of -10°C at 1200m a.s.l. are frequently observed during cold winter periods in certain areas of Norway (met.no 2010b). The temperature routine will however produce a temperature of –26.5°C at 1200m a.s.l. This effect causes the negative deviation in modelled *MAGT* at Tron and Iskoras, the two most continental borehole sites.

Precipitation is a difficult parameter to reproduce spatially, since it can occur highly localized and is influenced by both proximity to water bodies and terrain (Engeset et al. 2004). Interpolated values will also lead to a smoothing of the data, and because of major underestimations of measured precipitation values in Norway, mainly because wind makes it difficult to collect the precipitation, extreme events will not be reproduced (Engeset et al. 2004). However, at weather stations measuring both precipitation and wind speed, the precipitation measurements are corrected for underestimations due to loss during wind events. This correction is for some stations thought to be too strong, and in combination with too steep precipitation gradients and inversion effects in many areas, this gives an overall overestimation of *swe* (Mohr and Tveito 2008, Dyrrdal 2010). This effect is enhanced at higher elevations. Analysis of the snow depth data shows a general underestimation of snow depth. Dyrrdal (2010) explains this with an excessive compaction of snow in the hydrological model used in the precipitation/degree-day snow model, resulting in too high snow densities. This compensates for the overestimation of *swe* in some areas, but this is probably not the case everywhere. When comparing three selected regions; Finnmarksvidda, Røros and Romerike, Finnmarksvidda shows the strongest underestimation in total number of snow days and total snow depth. Røros has the poorest reproduction of number of snow days, while the snow model gives best results for Romerike (Dyrrdal 2010). However, even if the total amount of snow in each grid cell is relatively well reproduced or even overestimated, the actual snow depth for most areas above treeline is much less because of wind drift. The snow typically blows over the edges of the mountain summits and accumulates in forested areas and in hollows. The result is substantial spatial variations in snow depth in response to topography. Therefore, snow depths in the models are reduced with 30% above treeline, and snow density is reduced in forested areas. This is a rough approximation, and it is likely that overestimation of snow above reline varies with precipitation and climate regions in Norway. Therefore, this topic needs further .

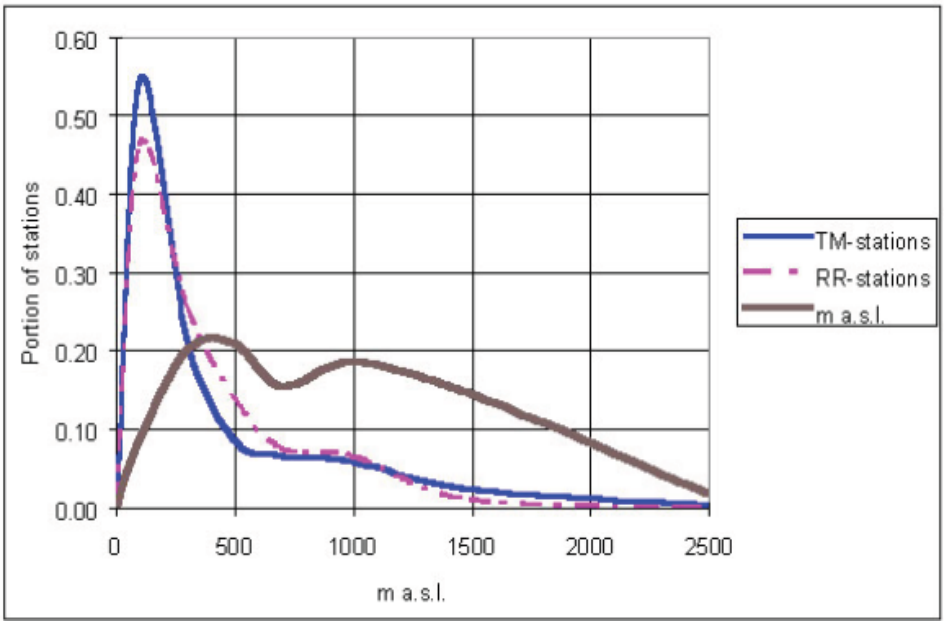

Figure 32: Meteorological stations distributed on height above sea level. TM is temperature stations, RR is precipitation stations. The brown line indicates the altitudinal distribution of topography (Tveito 2009).

8.1.2 Block field map

Blockfields are very important for the permafrost distribution in Norway, as they are normally found at higher elevations and are characterized by a negative thermal anomaly. However, blockfields are poorly mapped on existing maps of subsurface material of Norway, necessitating the construction of an improved map of Norwegian blockfields. This was done by classification of Landsat images based on spectral signature, and the results are very satisfactory (see Chapter 4.1.3). Most of the MTD-loggers placed in blockfields are correctly classified in the map (e.g. Figure 20). Only three boreholes are located in blockfield; Juvvass BH1 and 2, and Tron BH1. The boreholes at Juvvass are not classified as blockfield, but BH1 is correctly classified in the 240m resolution map. The area around BH2 at Juvvass cannot be considered as a typical openwork blockfield area, and may be better characterized as a ground moraine area. Additionally, Tronfjell and Tron-BH1 are correctly classified as blockfield also in the 1km resolution map.

The error sources of the blockfield map are mainly related to the quality of the Landsat images. The best image since 1984 for each area was chosen, but still the image quality for some areas is poor. This is particularly true of coastal areas, as these regions typically have

much cloud cover. In northwestern Norway, where the summers and snow free seasons are short and cloud cover persists for much of the year, cloud and snow free scenes was sometimes absent even when all scenes taken since 1984 was examined. Combinations of partly overlapping scenes are used, but the quality of the classification is still reduced in certain areas. However, none of these areas contain significant blockfields. This classification was done with 240 meters resolution, which also gives a lower limit for the size of blockfields included. When the map was reclassified to 1km resolution, some of the areas were lost. It might have been useful to expand the blockfields into larger clusters at 240 meters resolution, before reclassifying to 1km resolution to avoid "loosing" areas of scattered 240m pixels of blockfield. This is not done in this study, but should be considered in the future.

The great advantage with this method is that only openwork, active blockfields are classified, and vegetation covered blockfields are excluded. For thermal modelling purposes, mainly the non-vegetated blockfields are of importance, since these are the areas producing a pronounced negative thermal anomaly. The produced map constitutes a significant improvement compared to previous published blockfield mappings for Norway, and will also have implications for geomorphologic studies.

8.1.3 Geological and vegetation maps

The geological maps from NGU are considered as being of very good quality. Both the subsurface material and the bedrock map are digitized vector maps based on analogue Quaternary geological and bedrock maps of difference scales, mainly 1:50 000 and 1:250 000. Some of the classes are lost in the reclassifying to $1km^2$, and for the subsurface material map the sub grid variability is strong in some areas. However, the spatial geological data is not considered as a major source of error in the permafrost models. The vegetation map CORINE2000 is a general-purpose map, based upon much more detailed existing data sources. Small polygons less than 25ha were slightly enlarged, and if multiple data covered the same space, a priority list according to importance was used. Forested areas have the lowest priority, to make smaller areas visible. This might result in a slight decrease of the forested areas, but will not give any sever errors at $1km^2$ resolution. The classes in all these maps are however decided from the users need. Since the map is designed for a wide range of users, the classes are not optimized for modelling the thermal regime in the ground. Ideally

for this purpose there should have been better classifications of bedrock, blockfields and ground moraines, and also distinction between different types of mires.

8.2 Parameterization and *n*-factors

8.2.1 *n*-factors

Several studies have examined the controlling site characteristics of the surface offset. For *nT*-factors the main controlling characteristics are shading (Taylor 1995, Klene et al. 2001), albedo and soil moisture because of release of latent heat (Klene et al. 2001, Karunaratne and Burn 2004). During the winter season the *nF*-factors are primarily controlled by snow conditions, but mean annual air temperature (Smith and Riseborough 2002) and subsurface thermal conditions (Karunaratne and Burn 2004) also influence the thermal ground surface regime. Karunaratne and Burn (2004) found that the vegetation characteristics at a site has lower influence on the *n*-factors than the soils thermal properties in a boreal forest near Mayo, Yuko Territory. The impact of the insulating snow cover is larger with higher moisture contents in the subsurface material, but will also vary with active layer depth. However, Karunaratne and Burn (2004) also conclude that the influence of subsurface conditions is insignificant when *n*-factors are applied at continental scale. Most permafrost areas in Norway are above the treeline and located in well drained mountainous areas. The water content in these areas is very low, and the effect of latent heat due to soil moisture is less pronounced in most areas.

Due to different climatic conditions and land cover types, it is important to adjust the *n*-factors to Norwegian conditions. *n*-factors have previous been examined by Juliussen and Humlum (Juliussen and Humlum 2007), and the CRYOLINK project will improve the data basis on *n*-factors in Norway by installing air/ground stations and i-button stations at three key sites sites. In addition ground surface temperature (GST) from MTD-loggers were connected to gridded air temperature data (see Figure 27 and Table 8). The sensitivity due to inter and intra variation in the surface classes in addition to variation in r_k was examined in Chapter 6.3. Variation in measured *nT* is low for all classes. The summary below is based on degree day indexes from Tronfjell in Alvdal.

Inter-class variation - Due to snow cover, there is a large variation in measured *nF* for barren ground and blockfields, ranging from 0.2 to 0.9. Therefore *nF* for barren ground is

related to snow depth. 20cm variation in *AMSD* gives a Δ*MAGT* up to 0.5°C. *nF* for forest and mires are very consistent. Variation in the lower vegetation class in winter is fairly high, probably due to differences in the isolating effect of snow cover. Ideally there should be a finer classification of lower vegetation, where some of the classes are related to snow cover in winter. All surface types have fixed summer *nT*-factors, and the inter-class variation is low for all classes. These findings are supported by several other *n*-factor studies in Canada and Alaska (Jorgenson and Kreig 1988, Taylor 1995, Klene et al. 2001, Karunaratne and Burn 2004, Juliussen and Humlum 2007), see Appendix B.1.

Intra-class variation introduces an uncertainty of approximately 0.4°C (Chapter 6.3.2). There are some exceptions: change from the mire class to all other classes in maritime climates causes deviations up to 2°C, while change from forest in very continental climate gives deviations over 3°C. The model is in general more sensitive to surface class variations in continental climate. This is due to larger seasonal variations, and thus a higher seasonal energy exchange between air and ground. However, the topography is more homogeneous in the continental areas of Norway, reducing the variability of most parameters.

***nF*-factors** have previously been related to snow depth by Smith and Riseborough (2002), using a numerically ground thermal simulator. In Norway, a relation between *nF* and seasonal mean snow depth was established based on *i*-button stations. The two relationships are compared in Appendix B.2. The most prominent difference is that the Canadian developed *nF*–values decreases much more with increasing snow depth (considering similar *MAAT* ≈ -2°C). *nF* developed in Norway stabilizes at 0.25 at 50cm snow depth while the relation developed by Smith and Riseborough decreases gradually down to 0.1 at 1 meters depth. The comparison is difficult since Smith and Riseborough give no information about how snow cover is calculated. It is likely that the snow cover have higher thermal conductivities in the Canadian Arctic, and therefore gives lower *nF* because of a more continental climate and more water in the underlying ground. With higher water contents a larger amount of latent heat is released, and trapped under the snow cover. *i*-button sites in Norway are installed in a mountain environment, exclusively at dry sites with little sediment cover. If sediment types typical of the Mackenzie River Valley were used in the numerical simulations, this explains the difference.

Density measurements were taken at maximum snow depth at all i-button stations in March 2011, allowing for a relation between *nF* to snow water equivalent instead of snow depth.

The relation between *nF* and snow water equivalent is even more clear (Figure 16), and is assumed to improve the quality of the model. First of all because the snow depth maps are calculated from snow water equivalent based on a snow model, and therefore the snow water equivalent maps are more reliable. Secondly, *swe* and *nF* has a physically closer relation.

nT-factors - Areas of barren ground have normally no surface offset during summer season, giving an *nT* of 1 with only minor variations. These variations are just as attributed to different depths of the temperature logger as they are to real differences. It is difficult to get the real ground surface-air interface temperature using data loggers, and still have no direct sunlight on the logger. The *nT* for bedrock is sometimes up to 1.5 because of heating of the rocks. This is partly accounted for in the r_k-values in the model, but should rather be included in the *nT*-factors in future run. Forested areas are not examined in the CRYOLINK-project, but both MTD-loggers coupled to SeNorge air temperatures (Chapter 6.3.2), data collected by Juliussen and Humlum (Juliussen and Humlum 2007) and data from Canada and Alaska (Appendix B.1) shows *nT*-factors between 0.9 and 1, depending on the density and height of the vegetation. Since permafrost is believed not to occur in forested areas in Norway (Isaksen et al. 2008), the value of 1 for lower vegetation is the most important for permafrost modeling. *nT* for mires are based on MTD-loggers related to SeNorge data in addition to data from previous studies by Taylor (Taylor 1995) and Jorgenson and Krieg (Jorgenson and Kreig 1988) in Alaska. While *nT* for mires is dependent on the water content, values are typically around 0.85.

8.2.2 Thermal conductivity in the ground

The thermal offset is controlled by the ratio between thermal conductivity in the active layer in thawed and frozen states. The main control for the thermal offset is the water content of the ground. It is difficult to produce reliable water content data. Water content is also difficult to reproduce on regional scale, due to large small-scale variations. However, most of the permafrost areas in Norway are underlain by bedrock or blockfields, and the uncertainty is much reduced due to very low water contents in these areas. This is a big advantage for permafrost modeling in mountainous environment. In sediment covered areas conductivity data obtained from Alaska (GIPL-model, see Chapter 4.1.4) are assigned to Norwegian subsurface material classes. Since these data are developed for areas with different lithology and sediment types, they might not reflect Norwegian conditions. Sediments vary much more in moisture content, and consequently the uncertainty in the thermal offset is. Mires have

been discussed in detail in Chapter 8.3.3, and have much larger variation in water contents. However, the presence of an underlying silt layer is maybe even more important for a correct modeling of the surface offset in palsa mires.

Compared to the TONE-model (the TTOP-model implementation for the Mackenzie River Valley) presented in Table 12, the r_k-values used in the CryoGRID-models are relatively high. It is likely that the sediments in Norway in general are drier, and that the sediment cover is much thinner than in the Mackenzie River Valley. This will imply that the thermal offset for many sediment areas are a combination of sediments and bedrock. A higher r_k is in that case reasonable.

Table 12: Conductivity values applied in the TONE-model.

TONE DATA	K_t ($Wm^{-1} K^{-1}$) (TONE)	K_f ($Wm^{-1} K^{-1}$) (TONE)	r_k (TONE)	r_k (CryoGRID)	Subsurface material class
Colluvial complex	1.15 – 1.54	1.61 – 2.69	0.57 – 0.71	0.85-0.99	80-88
Glaciolacustrine	1.21 – 1.62	1.82 – 2.74	0.59 – 0.66	0.74	30
Aeolian deposits	1.39 – 1.60	1.63 – 2.47	0.65 – 0.85	0.99	60
Glaciofluvial	1.26 – 1.66	1.65 – 2.50	0.66 – 0.76	0.96	87
Alluvial deposits	1.3 0– 1.72	1.59 – 2.53	0.68 – 0.82	0.83	54
Glacial till	1.41 – 1.98	1.68 – 2.92	0.68 – 0.84	0.82	11
Organics (peatlands)	1.52	1.70	0.31	0.55	90

Two methods are used to calculate r_k at all TSP and CRYOLINK borholes in Norway. The TTOP-model is used to calculate r_k from measured *MAGST* and degree days at the ground surface for each borehole, presented under TTOP in Table 13. In addition a 1D-model are adjusted and run for 13 boreholes (Hipp et al. 2011), and r_k- values from this study are included in Table 13. The values are compared to r_k from the CryoGRIDeq-models for equivalent subsurface material class. r_k-values calculated from the TTOP-model are in general higher than the 1D model, and most boreholes have values higher than one. The TTOP-model describes the thermal offset in an equilibrium situation. Using the TTOP -model "backwards" to estimate r_k for the respective borehole will not necessarily give meaningful values in cases where the temperature regime is far from equilibrium. This can be seen from the r_k-values exceeding 1, which is physically impossible since K_t can never exceed K_f. In addition there may be local 3D-effects that the model is unable to account for. This might explain why very high r_k-values (exceeding 2.0) are observed at some of the boreholes (Juv-BH5 and Lavkavagge-BH2). However, the general trend for bedrock,

blockfield and moraine sites is r_k-values close to 1. The r_k-values estimated with the 1D-model do not vary much, ranging from 0.95 to 1 at most sites, and is in very good accordance with the CryoGRIDeq-models for bedrock and blockfields. It's surprising that the values for moraines in the 1D-model are also above 0.9 at most of the boreholes. For moraine sites the CryoGRIDeq-models have different values for thick and thin moraine cover, these values are 0.81 and 0.9, respectively. None of the moraine boreholes have r_k below 0.87 in the 1D-model. The r_k for moraines will vary with the proportions of coarse blocks and sediment, and it might be questioned whether the r_k of 0.81 for thick moraine cover in Norway in general is too low. Thick moraine cover (12) is the subsurface material class accounting for the largest area of permafrost. Indeed, the conductivity values for this class require further investigation.

Table 13: The table shows the r_k-values at each borehole estimated with the TTOP-model from borehole data, a 1D-model and the CryoGRID-models.

Borehole	Subsurface material class	TTOP (°C)	1D model(°C)	CryoGRIDeq(°C)
Abo BH1	Bedrock	1.39	1.00	1.05
Abo BH2	Bedrock	1.64		1.05
BH31/PACE31	Blockfield	1.27	0.95	0.95
Dovrepals	Peat	0.48		0.55
Guol BH1	Bedrock	1.27	0.99	1.05
Guol BH2	Bedrock	0.94	0.99	1.05
Guol BH3	Bedrock	1.19	0.99	1.05
IskBH1	Moraine	1.14	0.99	0.81
IskBH2	Sediment 1.5m - bedrock	1.06	0.97	1.05
Jet-BH1	Bedrock	0.94	0.99	1.05
Jet-BH2	Bedrock	1.02	0.99	1.05
Jet-BH3	Bedrock	1.83	0.99	1.05
Juv-BH1	Blockfield	1.41	0.88	0.95
Juv-BH2	Blockfield	0.64	0.95	0.95
Juv-BH3	Moraine	0.32	0.96	0.81
Juv-BH4	Bedrock	1.09	0.99	1.05
Juv-BH5	Moraine	2.69	0.96	0.81
Juv-BH6	Moraine	1.92	0.87	0.81
Kistefjellet	Bedrock	1.64	0.99	1.05
Lavka BH1	Moraine	1.68	1.00	0.90
Lavka BH2	Bedrock	2.21	1.00	1.05
Lavka BH3	Bedrock	1.13	0.99	1.05
NoBH1	Bedrock	0.93	0.99	1.05
NoBH2	Bedrock	1.28	1.00	1.05
NoBH3	Bedrock	1.16	0.99	1.05
Tro-BH1	Blockfield	0.78	0.96	0.95
Tro-BH2	Blockfield	1.07	0.96	0.95
Tro-BH3	Moraine	1.05	0.90	0.81

8.2.3 Parameterization of blockfields

Due to the negative thermal anomaly in blockfields, these features often correspond to the lower limit of permafrost (Harris and Pedersen 1998, Gruber and Haeberli 2007). The processes causing a negative thermal anomaly in blockfields have been described in detail in Chapter 2.2.1. Temperatures at the ground surface and also further down in the blockfields are highly connected to air density both in summer and winter. This process connects air temperatures to temperatures at and below the ground surface throughout the year, and consequently *n*-factors are high both in summer and winter. The reduced insulating effect of the snow cover is frequently attributed to discontinuities allowing for efficient heat conduction by rocks protruding the snow cover (Juliussen and Humlum 2008). The negative thermal anomaly in blockfields during winter is therefore assumed to be highly connected to the surface roughness as this property controls snow cover continuity. This implies that if a continuous snow-surface cover occurs, the effect of the snow cover will be similar to that observed at bedrock sites. Five of the CRYOLINK air/ground stations in addition to the PACE site at Juvvass are located in blockfields, and have been used to test this theory. Daily snow depth is measured at four of the stations (Juv-BH1,Juv-BH2, Tron-BH1 and Tron-LB6). Based on data from 2008-2010, *n*-factors and r_k values are calculated (Table 14). At all sites *nT* are close to 1, while there is a larger site-to-site variation in *nF*. The two bare blown sites at the top of Juvvass, PACE and Juv-BH1, have very high *nF* values of 0.76 and 0.93, while at the stations with thicker snow cover *nF* vary between 0.15 and 0.27. These findings support the theory that the effect of the snow cover is similar to bedrock sites with a discontinuous snow cover. The limit for a continuous snow cover is further dependent on the ratio of snow depth and surface roughness, and it is therefore hard to determine. At present, distributed data exists for blockfield roughness in Norway. In the dataset presented in Table 14 there is a limit between *AMSD* of 27cm and 40cm. *nF* in the model is therefore related to snow depth at *AMSD* over 35cm. Tron-LB5 has relatively shallow snow depths, but a *nF* of only 0.51. This station has only one year of measurements which might explain the deviation from the other data. Biases due to direct sunlight on the temperature logger, different depths of the ground surface measurement or rime collecting on at the *i*-buttons may occur at all stations. Differences in the start and end of the freezing season and the start and end of snow cover also serve to complicate the relationship between snow cover and *nF*. The *n*-factors presented in Table 14 are in good agreement with the measurements done by Juliussen and

Humlum (Juliussen and Humlum 2007) in Femundsmarka, southeastern Norway. However, this study did not contain measurements in blockfields with deep snow cover.

Gruber and Hoelzle (2008) explain the cooling effect in blockfields resulting from reduced effect of snow cover during winter somewhat differently. At a bedrock surface the heat conduction through the snow cover is very small, and the heat conduction from deeper ground layers dominates the temperature at the snow/ground surface interface. This effect is also the idea behind the BTS-method (Haeberli 1973). With a significantly lower thermal conductivity in the near-surface ground layer, the relative effect of the heat transfer through the snow cover increases. This result in ground surface temperatures responding more to atmospheric forcing, and implies that the *nF* should also be very high in blockfields with a thicker snow cover. Results in this thesis do not support this theory, as three of the stations have *nF* below 0.3. One explanation is that the blocks at the research sites in Norway are smaller with more debris in the spaces between the rocks, compared to the blockfields in the Alps. This will increase the thermal conductivity of the ground, and decrease the relative effect of the heat transfer through the snow cover.

Table 14: Data from the six CRYOLINK-sites located in blockfields, measuring air and ground surface temperatures, in addition to mean seasonal snow depth.

Site	Year	*AMSD*	*nF*	*nT*	r_k	r_k, 1D model
Pace-30	2008 - 2010	shallow	0.93	1.17	1.27	0.95
Juv-BH1	2008 - 2010	4.1	0.76	1.08	1.41	0.88
Juv-BH2	2008 - 2010	70.7	0.27	0.99	0.64	0.95
Tro-BH1	2008 - 2010	≈40	0.15	0.83	0.78	0.96
Tro-BH2	2008 - 2010	46.7	0.21	1.13	1.07	0.96
Tro-LB6	2009 - 2010	26.6	0.51	1.10		

The r_k-values representing the thermal offset are also used for blockfields, even though heat exchange in the upper part of the active layer is largely driven by convective forces, and not solely conductive. There is normally a gradually transition from larger blocks with large voids, to smaller blocks interlaced by sediments, to bedrock. The depth of this transition decides the conductive properties of frozen and thawed ground, and also varies between blockfields. However, Harris and Pedersen (1998) suggests that a thin cover of blocks produces a similar negative thermal anomaly for ground temperatures as does a thicker cover of blocks. For both varieties of blockfields the shape of the ground temperature envelope is as

an inverted cone rather than the bell-shape characteristic of fine-grained soils. Mean annual ground temperatures are just slightly warmer than mean annual ground surface temperatures. Converted to r_k this implies values close to 1, even though the effect is not due to low ground water contents. Based on data from the five boreholes drilled in blockfields (Table 14), r_k is calculated for each borehole using the TTOP-equation "backwards" (for further description, see Chapter 8.2.2). This results in r_k varying around 1. Calculated r_k for each borehole using a 1D-model are also considered and included in Table 14. These data indicates a lower r_k, varying from 0.88 to 0.95. r_k for blockfields in the model is fixed to 0.95, giving a slightly larger thermal offset than bedrock.

In the mKA-model blockfields are treated as bedrock in the surface offset, and similar to TTOP in the thermal offset. As a future improvement of the model the thermal effect of the snow cover should be adjusted for blockfields.

8.3 Evaluation of the CryoGRIDeq- models

8.3.1 Boreholes

The total root mean square error between measured and modelled ground temperatures at all borehole sites is 0.75°C (referring to the TTOP-model). This is a good result considering that the borehole data are compared to a cell size of 1km^2. Many of the mountains have transects of boreholes from the summit and down the mountain side. There is a tendency that the uppermost borehole is modelled too warm, while the lower boreholes are too cold. Examples are Abojavri, Guolosjavri, Jetta and Juvvass. This can be explained by the location of the uppermost borehole, normally situated on the coldest spot at the summit. The snow depth at the mountain summits are normally overestimated in the SeNorge data due to wind drift; this is particularly valid for the uppermost boreholes as they are all situated at bare blown spots and are consequently colder than the average temperature of the grid cell. In addition, the 3D cooling effect is greatest at the summit sites. The two most continental locations; Iskoras and Tronfjell show colder than actual *MAGT* in both models. This is attributed to inversion effects which are not reproduced by the SeNorge air temperature data (Tveito et al. 2000, Isaksen et al. 2008).

8.3.2 BTS-evaluation

Permafrost distribution from the TTOP-model coincides very well with the permafrost distribution modelled by BTS-probability maps for Jotunheimen and Dovre (Figure 21, a and c). The mKA-model presents anomalously low temperatures at both sites (Figure 21, b and d). In Femundsmarka (e-h) the TTOP-model does not reproduce permafrost in good accordance to the BTS-maps. Barely any permafrost is reproduced at Elgåhogna, and the area on Sølen is too small. However, the map indicates permafrost occurrence in the surrounding mires. The poor correlation is partly explained by the surface cover type. Both mountains are covered by blockfields, but are mapped as bedrock. This gives an *nT* of 1 instead of 0.9, and *nF* which is dependent on snow cover. This is the same case as the area along the road up to Juvvass in Jotunheimen, which is also partly covered by blockfield, but mapped as till. However, while the bedrock at Elgåhogna and Sølen has an r_k-value of 0.96, the till at Juvvass has an r_k of 0.81 producing somewhat lower *MAGT*. In addition the summers are longer and warmer resulting in a greater amount of thawing degree days in eastern Norway; 758 and 554 thawing degree days (*TDD*) at Elgåhogna and Sølen, respectively. The amount of *TDD* at Juv-BH2 is only 409 only. Both the *nT* and the r_k value modify the effect of the thawing degree days in the TTOP-model (see Chapter 2.3.3), and therefore the model is more sensitive to errors in these parameters in regions with warmer summers. Freezing degree days are more consistent between sites with 2198, 1991 and 2137 *FDD* observed at Juv-BH2, Elgåhogna and Sølen respectively. Since all sites have an *AMSD* above 60cm, equivalent to *nF* = 0.3, the cooling effect of the ground is similar. The sensitivity of the summer surface cover is probably the explanation for the poor reproduction of permafrost on Elgåhogna and Sølen. The mKA-model tends to have more extreme temperature increase with elevation, and is generally colder on the mountain tops and warmer in the valleys. In the scatter plots of measured and modelled *MAGST* in Figure 20 the mKA-model has more extreme ground surface temperatures, which implies that the model is closer to the air temperature variations, and that the effect of vegetation and snow cover is less than in the TTOP-model. This explains why the model fits best with the BTS-probability maps at the two mountains in Femundsmarka.

The BTS-probability maps are not real validation data as they are indirect evidence of permafrost. However, the maps are made in areas where several different permafrost investigations have been done, such as boreholes, a large number of MTD-loggers, BTS-

measurements and mappings of permafrost landforms. The maps, especially at the Jotunheimen-location are considered to be very reliable (Isaksen et al. 2002). Therefore, it can be concluded that the TTOP-model provides an acceptable reproduction of the permafrost limits in Jotunheimen.

8.3.3 Rock glaciers, ice-cored moraines and palsas

The distribution of potential palsa mires (areas mapped as mires with *MAGT* below 0°C) is in good accordance to the palsa bog map based on field observations in Figure 23. The TTOP-model indicates a large number of palsa mires also in southeastern Norway; a much larger area than observed. There might be a lack of field observations in certain areas of southern Norway, however, it is not likely that there are palsa mires at all locations mapped by the TTOP-model. Certain conditions are necessary to grow palsa bogs (Seppälä 1986); (1) continental climatic conditions of low temperatures and low precipitation rates, (2) a thick layer of peat exceeding 50cm, (3) underlying silty soil, (4) hydrological conditions causing a water-saturated peat and moving water in the underlying mineral soil and (5) wind drift giving a thin snow cover. Distribution of mires in the model is based on the subsurface material map, which has only one mire class including all areas with an organic layer thicker than 50 cm. Since a silt layer must be present in order to generate segregated ice which is a requisite to grow palsas (Sollid and Sørbel 1974, Williams and Smith 1989), the maps used here are not able to reproduce areas prone for palsa bogs. The areas in southeastern Norway where the TTOP-model reproduces potential palsa mires coincides with areas lacking fine sediments due to heavy glacial erosion and minor deposition, and explains why there are no palsas at many of the “cold mires” in southeastern Norway.

In Figure 24 *MAGT* for 1981-2010 is compared to the mapped distribution of permafrost landforms in Norway (Lilleøren and Etzelmüller in prep). The map shows a very good correlation between present permafrost and active rock glaciers and ice cored moraines. Rock glaciers and ice cored moraines forms in permafrost environments (examples of rock glaciers creeping out on unfrozen ground does exist), but is also controlled by lithology and ice, rock and debris supply (Barsch 1996, Haeberli et al. 2006). Rock glaciers in mountain environments outside the high Arctic are often found close to the lower limit of permafrost occurrence (Haeberli et al. 2006), and since rock glaciers are relatively small features compared to the spatial resolution of the permafrost map, they might be found outside the modelled permafrost areas in Norway. There are some examples of this in the map, but the

permafrost features are still very close to the permafrost limit. Relict rock glaciers, which developed in a colder climate, are also mapped. These are now retreating or are already totally free of ice. These landforms are very useful indicators of past climate and permafrost distribution (Barsch 1996). Many of the relict rock glaciers in Norway probably developed in periods of colder climate after Holocene Climatic Optimum, while some may also date from earlier periods.

8.4 TTOP vs. mKA

As pointed out in Chapter 5, the MAGT produce by the mKA-model is colder than those from the TTOP-model for most of the higher elevated areas and warmer in lower elevated areas. The difference between TTOP and mKA is included in the Appendix D.11. However, the difference is not only related to elevation. There are some exceptions where the TTOP-model is clearly colder than the mKA-model: the area around Bieggavakke and the area south of Børselva in Finnmark (Figure 18, a and b) and the area around Dærtahytta in the inner parts of Troms (Figure 18, c and d). These areas coincide with blockfield areas (Figure 14, b). This is not surprising since the mKA-model does not treat blockfields separately in the vegetation and snow model, but uses the same parameterization as for bedrock. Scatter plots of the TTOP-mKA difference related to elevation for each vegetation class (Appendix E.1) shows that the mKA-model actually gives a lower *MAGT* for most blockfields, but at lower elevated blockfields the TTOP-model is colder. For most areas with mires the TTOP-model is colder than the mKA-model. This correlates with the higher ground temperature in the mKA-model at the palsa borehole at Dovre (Table 6). For forested areas, the mKA is colder at lower elevations; this difference decreases with elevation. This reason for this is that forest is not modelled properly in the mKA-model. The vegetation model treats taller forests as lower vegetation because no diffusivity data are available for taller forests. The mKA is colder for almost all of these areas, and the difference is relatively stable with elevation. For barren ground and blockfields the mKA-model tends to get colder with higher elevation. The thermal offset is similarly produced in the two models, and the deviation is explained by differences in the surface offset models. This is also clear from the pronounced difference in *MAGST* (Figure 22). The fact that the mKA is clearly colder for barren ground and blockfields is probably not related to the vegetation model. *nT* for both classes are 1, and there is no dampening effect in the mKA-vegetation. It is more likely that the difference is due to dissimilar modelling of the snow cover.

While the TTOP-model uses *nF* related to snow depth, the snow model integrates the physical properties of snow cover, such as thermal conductivity and diffusivity. In addition the snow model includes a dimensionless factor (μ) related to the effect the underlying ground have on the thermal effects of the snow cover, as described in Chapter 2.3.4. One of the thermal parameters included here is the effective heat capacity of the underlying ground. This parameter reflects the ratio between sensible and latent heat. The amount of latent heat in bedrock and blockfields are negligible, so this ratio will go towards infinite and consequently the dampening effect of the snow cover goes towards zero. We see evidence for that in our data. Scatter plots of the difference between *MAGT* from the TTOP-model and the mKA-model for each subsurface material class are included in Appendix E.2. These plots deminstrates that the mKA-model is coldest for subsurface materials with very low water contents (class 12, 55, 88, 100 and 130), including blockfield and bedrock. The description and water contents for each subsurface material is given in Table 4. The difference is much less for other subsurface materials. To solve the bias in the snow model for very low water content, it is suggested to exclude the factor μ for these areas. This implies that the thermal effect of the snow cover will be calculated from thermal conductivity (K_{sn}), heat capacity (C_{sn}) and height (H_{sn}) as follows:

$$s = e^{2H_{sn}\sqrt{\frac{\pi C_{sn}}{\tau K_{sn}}}} \tag{5.1}$$

A test run of where this condition is included in the model is presented. The difference in MAGT between the two models, equivalent to Appendix D.11., is presented in Appendix D.12. The result is promising, and shows that the new run has much lower deviation from the TTOP-model results. However, further investigations are required before the mKA-model gives satisfactory results.

Use of physically based model results in more correct descriptions of the reality than those derived from purely empirically based models. However, much more data are also required, and it is more challenging to adjust the model for problems like the one described above. The big advantage of a purely empirically based model, such as the TTOP-model, is that limited field data is needed, and the model is more easily tuned for specific areas. At the same time, such models tend to generalize site characteristics since few parameters are included. Much fewer vegetation classes are used in the TTOP-model, and snow depths are discretized to

intervals for each *nF*-factor. This "smoothes" out the temperature variations in the ground compared to the mKA-model. The data availability for the study area should be considered when choosing between empirically and physically based models. It must be considered whether the physical properties used in the model can be generalized for the chosen spatial resolution. The access and quality of spatial distributed data such as meteorological data, petro-physical data, vegetation, subsurface material, ground heat flow and bedrock are very good for Norway. This allows for physically based models to be implemented. However, the mKA-model includes a series of parameters which have never been studied in Norway, such as vegetation diffusivity, and thermal heat capacity and conductivity of the subsurface material. Good datasets are provided from University in Fairbank, Alaska (*GIPL*), but these are developed in a different environment with different vegetation species and subsurface material types. Consequently it is not straightforward to assign these data for Norwegian conditions. More investigation should be done for certain parameters to improve the implementation of the mKA-model. Since field measurements of subsurface material properties and vegetation diffusivity is difficult, it is suggested to use temperature data for air, ground and subsurface material to adjust the model values in the future.

8.5 Subgrid variability

A main focus in this study is to address the question of whether or not equilibrium models provide better information at fine resolution compared to coarser models in a partly mountainous environment in Scandinavia. The CryoGRIDeq-models produce an average ground temperature value for each grid cell. The degree of variation within a grid cell, and thus the error of the model, will differ between homogeneous and more heterogeneous areas. Recent studies from the Alps (e.g.Gubler et al. 2011, Hasler et al. 2011) stress micro scale variations in ground surface temperatures in areas of mountain permafrost. Regional grid-based permafrost models will always have certain sub-grid variability depending on spatial resolution and local variation in the area. It is of large importance that the spatial resolution used for meteorological parameters, such as air temperature and precipitation, are not suitable for the representation of locally varying parameters, such as water content and *MAGST*. It is also a problem that point measurements of parameters with sub-grid variation are used to calibrate grid-based model data.

Gubler (2011) presents a study on ground surface temperatures measured at two different scales; intra-footprint within $10m^2$ and inter-footprint over $16km^2$. They observe *MAGST* variation up to 9°C over the whole area, and variation up to 2°C within a homogenous $100m^2$ field consisting of large boulders. *MAGST* vary much less in more homogenous grass sites and areas of fine material. The study concludes that *MAGST* are statistically related to elevation, slope, aspect and ground cover type, and can vary by more than 2.5°C at small scales ($<<1km^2$) at steep slopes or in areas of large coarse blocks. This highlights the importance of evaluating the variability of the modelled parameter in the area of interest.

No equivalent sub-grid variability study has been done in mainland Norway, however Hauck et al. (2004) have conducted a BTS-survey including 357 measurements in Jotunheimen. On large scales, altitude explained 91% of the BTS-temperature variation, and the BTS-measurements showed a clear transition between non-permafrost and permafrost areas. On local scales 150 measurements were taken in a 500 meters long transect going between permafrost to non-permafrost regions. Even with BTS-temperature variations between -1°C and -5°C, the data shows the transition from permafrost to probable permafrost to non-permafrost in very good accordance with the DC resistivity data.

The topography in Norway is much more homogenous than the very steep mountains in the Alps, and barely any area in Norway has an altitudinal difference of 1400 meters over 16 km^2, such as is characteristic of the Corvatsch area in the Swiss Alps (Gubler et al. 2011). There are a few alpine areas in Norway (Lyngsalpene, Horrungane, Romsdalen and Sunnmørsalpene) with comparable topography, but the rest of Norway is dominated by paleic surfaces with gentle slopes. Therefore the large variations due to steep slopes are less pronounced. Solar radiation is of less importance in Norway than in the Alps (Juliussen and Humlum 2007) due to northerly latitude resulting in lower average sun angle. The variation in ground cover type is small in the mountains of Norway and most areas consist of barren ground with only some mosses or bedrock with no sediment cover. These areas are highly connected to the air temperature in summer. Because of short and relatively cool summers, the thermal regime is also less sensitive to variation in aspect and vegetation. In winter the onset, duration and depth of the snow cover will play a critical role in the ground surface temperature regime in these areas. Even if the total volume of snow in one grid cell is satisfactory reproduced, there might be large sub-grid variations due to snow drift. Snow cover can vary from no snow at windblown sites to over two meters in hollows inside one grid cell, and for this reason snow is the most important factor for sub grid variability in the

mountains of Norway. Even if the snow cover is the critical factor to ground surface temperatures, the study of Hauck et al. (2004) shows that the general transition zones between permafrost and non-permafrost areas are reproduced with winter ground surface temperatures both at local and larger scale.

Blockfields are very a dominant surface type at higher elevations in Norway. As pointed out by Gubler et al. (2011) there are large variations over small distances in blocky terrain. This is of course a problem in a permafrost model with a spatial resolution of 1km^2. The depth and size of the block may vary over short distances, e.g. from the southern to the northern side of Tronfjell in Alvdal. A general negative thermal anomaly in blocky terrain is reproduced by the model, but since the size and depth of boulders is unknown the variation within blockfields at all scales is not reproduced. This does affect the insulating effect of the snow cover. In areas of small blocks a shallower snow cover is needed to produce an isolating effect, while in areas with a higher surface roughness much more snow is required to get a continuous snow cover. As long as the snow cover is discontinuous, cold air will circulate down in between the blocks, and the blocks penetrating the snow cover will conduct energy out from the ground efficiently (Juliussen and Humlum 2008). The deviation in *MAGST* at two of the blockfield sites is up to 2°C, while *MAGST* is relatively well reproduced at the other blockfield sites. At the borehole site located in blockfields (Juv-BH1, Juv-BH2 and Tron-BH1) the deviation at all sites is less than 1°C and not significantly larger than at other sites.

Both studies described above examine the variation in ground surface temperatures. *MAGST* are validated against a large number of MTD-loggers. The scatter plots show that 75% of the variation in mean annual ground surface temperature is reproduced by the models. This suggests that general ground surface patterns can also be reproduced at 1km^2 resolution. However, only MTD-loggers representing the general snow distribution of the surrounding area were included, and the total variation in ground surface temperatures will be somewhat larger due to variations in snow cover.

The main outcome from the CryoGRIDeq is however the *MAGT*-map. Even with a significant variation in ground surface temperatures due to snow cover variations, the degree of variation will decrease through the active layer. First of all, the general dampening of the temperature and temperature amplitude results in less variation in *MAGT*. Second, lateral heat fluxes will smooth out small-scale variations in *MAGST*, particularly in mountainous areas

with high thermal conductivity. Still, variations due to small-scale fluctuations in water content and snow cover will be present. This can also be seen in the deviations between borehole measurements and modelled temperatures (Table 6). At Juvvass BH1, 4 and 5 have barely any snow, BH2 and 6 have a thick snow cover (max snow depth (SD) >2m), while BH3 has a medium snow cover (max SD 0.3 - 0.7m). The model produces too cold temperatures at Juv-BH1 and -BH4, too warm at Juv-BH2 and -BH6 and very close to the measured *MAGT* temperature at Juv-BH3. Juv-BH5 is an exception, having a thin snow cover but is still 1.16°C too cold in the model. The location at a much lower elevation than BH3 and BH4, and in addition 3D effects due to a surrounding thicker snow cover might explain this deviation.

Most of the deviation between model and measurements at Juvvass can be explained by local variations in snow cover. A regional model with $1km^2$ is not expected to reproduce such variation, but should reproduce the average thermal condition in the grid cell. At Juvvass borehole 1 and 2, and borehole 3, 4 (and 5) are located within the same grid cells in the model. The average *MAGT* of Juv-BH1 and 2 is -1.25°C, while the model produces -0.95°C. The average condition in the grid cell of borehole 3, 4 and 5 is probably best reproduced by BH3, having a moderate snow cover. The temperature of this borehole is -0.36°C, while the modelled *MAGT* is -0.27°C. This shows that even when comparing the model to borehole data, the correlation is very good. This is supported by the good accordance to BTS-maps and permafrost landforms.

The results show that a $1km^2$ resolution equilibrium model can reproduce the altitudinal limits of regional scale permafrost patterns in mountainous environments. This indicates that such models are also useful in environments with heterogeneous topography. Regional scale modeling is considered more reliable in homogenous high Arctic environments. However, the problem in these areas is that a small deviation in modelled ground temperature might move the permafrost limit over large horizontal distances. In a mountain environment there is a sharper transition zones between permafrost and non-permafrost areas, and the same modelled deviation might move the altitudinal limit, but the horizontal limit is much more robust due to modeling errors.

8.6 Present permafrost distribution in Norway

Two equilibrium models have been implemented on a regional scale for mainland Norway and the results are presented in Chapter 5. The permafrost limits modelled with the TTOP-model is in good coherence with the previous known regional altitudinal permafrost limits both in southern and northern Norway. From the transects in Figure 19 it is a clear east-west gradient; in mountains in Troms and Finnmark there are continuous permafrost above 1200m a.s.l. on the west coast and down to 700m a.s.l. on the east side of the mountains. On Finnmarksvidda permafrost is widespread down to 400 meters a.s.l. In Jotunheimen, southern Norway, the lower limit of continuous permafrost ranges from 1450 meter a.s.l. on the western side to 1700m a.s.l. on the eastern side (Figure 19, upper). All of these altitudinal permafrost limits are in good coherence with observations (Isaksen et al. 2002, Sollid et al. 2003, Heggem et al. 2005, Farbrot et al. 2008, Isaksen et al. 2008). According to the TTOP-model for 1981-2010, 6.4% of the Norwegian mainland contains permafrost. The largest permafrost area is found at lower elevated plains in inner parts of Finnmark. These areas cannot be classified as mountain permafrost, but since permafrost is not found down to sea level it is still classified as altitudinal permafrost rather than latitudinal permafrost. 33.9% of the total permafrost area is found in till, and on Finnmarksvidda almost only in till. In southern Norway permafrost is mainly found in the mountains in bedrock and blockfields, but also in till. Most of the scattered permafrost occurrences coincide with areas of mires.

8.7 Scenarios – implications for future

The permafrost occurrence during Holocene was examined in Chapter 7.1. The coldest and warmest periods since last ice age: the Little Ice Age (LIA) and the Holocene Climatic Optimum (HCO) were run in the model. The model estimates a permafrost area of 14.5% of the total Norwegian mainland during LIA, indicating a pronounced degradation of permafrost the last 200 years. Permafrost have a well-documented stabilizing effect on rock walls (Gruber et al. 2004). Isaksen et al. (2011) shows that destabilized rock faces, where large volumes of rock moves several cm per year, often are found in areas of warm permafrost or right below the altitudinal limit of discontinuous permafrost. They suggest that there is a connection between degradation of permafrost and the destabilization of rock faces. Therefore permafrost areas in steep terrain that have thawed since the little ice age are of great importance. Table 15 shows the decrease in permafrost area since the LIA distributed

on subsurface material type. There has been a pronounced decrease in areas of bedrock, which is of relevance for destabilization of steep rock walls. The areas that have been degrading can be located from Figure 30. The resolution of the model is too coarse to show single rock faces, and the 3D effect that plays a great role in the thermal regime of steep rock walls are also not reproduced in the model. However, it indicates the permafrost areas that have thawed since the LIA (Figure 30), and also the areas of warm permafrost (Figure 17). Thus, the model gives valuable information that can be used to identify areas vulnerable for destabilization, and of interest for further investigations.

Table 15: The table shows permafrost occurrence during LIA and today distributed on subsurface material type.

	LIA (km^2)	Today (km^2)	Decrease (km^2)
Till (11,15,21)	19041	6990	**12051**
Blockfields	6152	4659	**1493**
Mires (90)	6907	4009	**2898**
Bedrock (12,72,130,140)	12025	3597	**8428**
Ablation morene (14)	1300	672	**628**
Weathering material (73,80,81,82,88)	1381	671	**710**
Marine deposits (30,41,42,43)	65	13	**52**
Organic material, thin (100)	153	3	**150**
	47024	**20614**	**26410**

For the HCO the model estimates a permafrost occurrence of 1.1% of the total mainland area. Future permafrost predictions are examined in Chapter 7.2, indicating that only 0.2% of the land area will be underlain by permafrost with the predicted climate for 2071-2100. This implies that areas of very old permafrost will thaw, and if these areas contain organic material the chance for greenhouse gas emissions (GHG) are present. Table 16 shows that the largest decrease in permafrost older than HCO will occur for the subsurface material types mire, till and bedrock. Due to great uncertainty in the modeling of ground temperatures in mires (discussion in Chapter 6.3 and 8.1.3) the extent of these areas is probably overestimated. However, it is still likely that areas of organic material and permafrost older than HCO will thaw if the IPCC scenario A2 prediction for the coming century is realized. The decrease in mires with “old” permafrost is of interest for GHG emission studies, even though the Norwegian contribution is insignificant on global scale. The permafrost areas in Norway are easy accessible compared to the large permafrost areas in the Siberian and Canadian arctic, and are very likely to thaw during the next century. Therefore these areas are potentially

suitable field sites for process studies, and it should be considered to initiate GHG-emission monitoring in e.g. Finnmark when permafrost is still present in the ground. The permafrost degradation is also of importance for landscape development and geomorphologic processes (Etzelmüller et al. 2003, Berthling and Etzelmüller 2011). The reconstruction of the LIA permafrost distribution compared to the prediction for future permafrost distribution indicates a major rise in the lower altitudinal permafrost limits in the mountains. The predicted permafrost degradation will possibly have increased impacts on geotechnical properties of rock walls and slope stability in the coming century.

Table 16: Area underlain by permafrost in Holocene Climatic Optimum and 2071-2100 distributed on subsurface material type. Values are km^2 area of permafrost.

	HCO (km^2)	2071-2100 (km^2)	Decrease (km^2)
Till (11,15,21)	698	0	698
Blockfields	209	75	134
Mires (90)	2191	440	1751
Bedrock (12,72,130,140)	246	3	243
Ablation morene (14)	177	0	177
Weathering material (73,81,82)	40	0	40
Marine deposits (30,41)	0	0	0
Organic material, thin (100)	0	0	0

9. Conclusions

In this thesis two permafrost equilibrium models, originally developed for low-Arctic environments, have been implemented on regional scale for Norway at 1km^2 resolution. The models are forced with daily gridded temperature and snow data for the period 1957-2010. *n*-factors, describing the surface cover, have been adjusted for Norway based on field measurements taken during the CRYOLINK project. A blockfield map has been produced from classification of Landsat images and is an improvement compared to the existing land cover data. The model results have been validated with a number of temperature loggers, boreholes, BTS-maps and maps of permafrost landforms. Reconstruction of paleo permafrost distributions have been made, including Holocene Climatic Optimum and the Little Ice Age. The model is also run for a future scenario (2071-2100), forced with climatic data from the SRES A2 scenario.

Model performance

- The results from the TTOP-model showed very good agreement for measured mean annual ground temperatures in boreholes, with a total RMS of 0.75°C for all boreholes. The model results conform to BTS-maps and maps of permafrost landforms.
- *nF* is the most sensitive parameter in mountainous areas, resulting in a deviation of modelled mean annual ground temperature (*MAGT*) of 0.5°C for a variation of ±10cm annual mean snow depth.
- Large variations in soil water content in mires result in great uncertainties in *MAGT* modelled for these areas. Therefore, all mires of *MAGT* < 0°C were marked as "possible permafrost areas".
- The sensitivity of *MAGT*, due to uncertainty in the *n*-factors, increases with the number of thawing and freezing degree days and consequently with continentality.
- The TTOP-model tends to smooth out the temperature variations due to few surface cover classes, and discretized snow depth classes. In addition to an increase in the number of surface cover classes, it is suggested that *nF*-factors should be related to snow water equivalent instead of snow depth in future model runs.
- The mKA-model produces too cold temperatures in the mountains of Norway, probably due to a bias in the snow model for areas of very low water contents.

- The mKA snow model is a more physically correct representation of the snow cover, and further development of the snow model and the vegetation parameters is expected to give a more accurate representation of the thermal regime than the TTOP-model.
- At present, the state of permafrost in blockfields is more poorly reproduced in the mKA-model than in the TTOP-model. It should be examined whether a blockfield can be treated similar to a vegetation layer with certain thermal properties.

Permafrost situation in Norway

- A strong east-west gradient in lower altitudinal permafrost limits is seen in the mountains, both in southern and northern Norway. In Jotunheimen, southern Norway, the limit ranges from approximately 1450 to 1700m a.s.l. In Femundsmarka, situated in the more continental southeastern part of Norway, permafrost occurs down to 900m a.s.l. when mires are excluded. In Troms, northern Norway, the east-west gradient of the lower altitudinal permafrost limit ranges from 700 to 1250m a.s.l. In the more continental and lower elevated mountain plateaus in Finnmark, permafrost is widespread down to 400m a.s.l.
- Currently, permafrost covers approximately 6.4% of the total area of mainland Norway according to the TTOP-model for 1981-2010. When mires are excluded, 5.1% of the land area is underlain by permafrost. The two estimates can be regarded as upper and lower bound for the real situation.
- Of the total permafrost area 34% is in till, 23% in blockfields and 17% in bedrock. The rest is in sediment and organic material. In northern Norway the major permafrost areas are in till, while in southern Norway a larger part is found in bedrock and blockfields.

Historical and future permafrost distribution

- Reconstruction of historical permafrost distribution indicates that the permafrost occupied 1.1% of the total mainland area in the Holocene Climatic Optimum, while in 14.5% of the total area was underlain by permafrost throughout the Little Ice Age. This implies that the present near-surface permafrost area is only half of the possible near-surface permafrost area in the Little Ice Age. The largest decrease in permafrost from the Little Ice Age to present situation is found in southern Norway, and there mainly in till and bedrock.

- The future scenario indicates that there will be severe permafrost degradation if climate parameters projected under the SRES A2 scenario for 2071-2100 are realized. In this case it is estimated that only 0.2% of mainland Norway will contain permafrost; most of the permafrost degradation will occur in mires.

Outlook

The projected major degradation of permafrost at higher elevations will probably have implications for the destabilization of rock faces and steep slopes. Results from this study can be used to locate areas vulnerable for permafrost degradation during the next century. A warming will also result in a degradation of permafrost in organic deposits. Some of these areas contain permafrost older than the Holocene Climatic Optimum, and are potentially suitable sites for process studies of green house gas emissions due to easy access and ground temperatures close to zero.

This study demonstrates that equilibrium models developed for low-land Arctic permafrost can be modified to model permafrost temperatures and distributions in mountainous environments. The thesis exploits the potential of SeNorge data sets for permafrost modeling, and demonstrates the benefit of utilizing a wide range of field installations for parameterization purposes. The CryoGRIDeq-model is a significant step towards a better understanding of the spatial distribution of permafrost in Norway, and an advancement of the knowledge of historical and future permafrost conditions.

10. References

Angst, G. 2010. *Report of GIS work, Cryolink project*. Oslo: University of Oslo.

Balch, E. 1900. *Glacières or Freezing Caverns*, Philadelphia: Allen, Lane & Scott. 377 pp.

Barsch, D. 1996. *Rockglaciers: indicators for the present and former geoecology in high mountain environments*: Springer Verlag, Heidelberg. 331 pp.

Beldring, S., Andréasson, J., Bergström, S., Engen-Skaugen, T., Førland, E., Jónsdóttir, J., Roald, L., Rosberg, J., Suomalainen, M., Tonning, T. and al., e. 2006. *Hydrological Climate Change Maps of the Nordic Countries: Based on RegClim HIRHAM and Rossby Centre RCAO Regional Climate Model Results.* Norwegian Water Resources and Energy Directorate, Report no 4/2006.

Berge, S. 2011. *Terrengmodell med 50 meters grid.* Statens Kartverk 2009 [Accsessed: 19.05 2011]. Available at http://www.statkart.no/Terrengmodell+med+50+meters+grid.d25-SwtLY27.ips.

Berthling, I. and Etzelmüller, B. 2011. The concept of cryo-conditioning in landscape evolution. *Quaternary Research* 75, 378-384.

Blikra, L., Longva, O., Harbitz, C. and Løvholt, F. 2005. Quantification of rock-avalanche and tsunami hazard in Storfjorden, western Norway. *in: Landslides and Avalanches: ICFL 2005 Norway*, Norway, 57-64.

Braathen, A., Blikra, L., Berg, S. and Karlsen, F. 2004. Rock-slope failures of Norway, type, geometry deformation mechanisms and stability. *Norsk geologisk tidsskrift* 84, 67-88.

Brown, J., Ferrians, O.J.J., Heginbottom, J.A. and Melnikov, E.S. 1997. *International Permafrost Association Circum-Arctic Map of Permafrost and Ground Ice Conditions.* U.S. Geological Survey.

Burn, C. and Smith, C. 1988. Observations of the" thermal offset" in near-surface mean annual ground temperatures at several sites near Mayo, Yukon Territory, Canada. *Arctic* 41, 99-104.

Carlson, H. 1952. Calculation of depth of thaw in frozen ground. *Frost action in soils Highway Research Board Special Report Number 2*, 192–223.

Christiansen, H., Etzelmüller, B., Isaksen, K., Juliussen, H., Farbrot, H., Humlum, O., Johansson, M., Ingeman Nielsen, T., Kristensen, L. and Hjort, J. 2010. The thermal state of permafrost in the nordic area during the international polar year 2007–2009. *Permafrost and Periglacial Processes* 21, 156-181.

Comiso, J.C., Parkinson, C.L., Gersten, R. and Stock, L. 2008. Accelerated decline in the Arctic sea ice cover. *Geophys Res Lett* 35, L01703.

Davies, M.C.R., Hamza, O. and Harris, C. 2001. The effect of rise in mean annual temperature on the stability of rock slopes containing ice-filled discontinuities. *Permafrost and Periglacial Processes* 12, 137-144.

Dingman, S.L. and Koutz, F.R. 1974. Relations among Vegetation, Permafrost, and Potential Insolation in Central Alaska. *Arctic and Alpine Research* 6, 37-47.

Dingman, S.L. 2002. *Physical hydrology*, Upper Saddle River, N.J.: Prentice Hall. X, 646 s. pp.

Dyrrdal, A.V. 2010. An evaluation of Norwegian snow maps: simulation results versus observations. *Hydrology Research* 41, 27-37.

Ekman, S. 1957. *Die Gewæsser des Abisko-Gebietes und ihre Bedingungen (In German)*. Handlingar, 4 serien. 6:6, Stockholm: Almqvist & Wiksell. 172 s. pp.

Engen-Skaugen, T., Haugen, J.E. and Tveito, O.E. 2007. Temperature scenarios for Norway: from regional to local scale. *Climate Dynamics* 29, 441-453.

Engen-Skaugen, T., Haugen, J.E. and Hanssen-Bauer, I. 2008. *Dynamically downscaled climate scenarios available at the Norwegian Meteorological Institute - per December 2008*. Oslo, Norway. Norwegian Meteorological Institute (met.no). Report 24/08. Section: Climate.

Engeset, R., Tveito, O.E., Udnæs, H., Alfnes, E., Mengistu, Z. and Isaksen, K. 2004. Snow Map Validation for Norway. *XXIII Nordic Hydrological Conference, 8-12 Aug*, Tallin, Estonia: NHP report, 122-131.

Etzelmüller, B., Berthling, I. and Sollid, J. 1998. The distribution of permafrost in Southern Norway; a GIS approach, 251–257.

Etzelmüller, B., Hoelzle, M., Heggem, E.S.F., Isaksen, K., Mittaz, C., Mühll, D.V., Ødegård, R.S., Haeberli, W. and Sollid, J.L. 2001a. Mapping and modelling the occurrence and distribution of mountain permafrost. *Norsk Geografisk Tidsskrift-Norwegian Journal of Geography* 55, 186-194.

Etzelmüller, B., Ødegård, R.S., Berthling, I. and Sollid, J.L. 2001b. Terrain parameters and remote sensing data in the analysis of permafrost distribution and periglacial processes: principles and examples from southern Norway. *Permafrost and Periglacial Processes* 12, 79-92.

Etzelmüller, B., Berthling, I. and Sollid, J.L. 2003. Aspects and concepts on the geomorphological significance of Holocene permafrost in southern Norway. *Geomorphology* 52, 87-104.

Etzelmüller, B., Farbrot, H., Humlum, O., Christiansen, H., Juliussen, H., Isaksen, K., Schuler, T., Ødegård, R. and Ridefelt, H. 2008. Mapping and Modeling the Distribution of Permafrost in the Nordic Countries. Paper read at Ninth International Conference on Permafrost, University of Alaska, Fairbanks, June 29-July 3, 2008, at Fairbanks, Alaska.

Etzelmüller, B. and Frauenfelder, R. 2009. Factors Controlling the Distribution of Mountain Permafrost in the Northern Hemisphere and Their Influence on Sediment Transfer. *Arctic, Antarctic, and Alpine Research* 41, 48-58.

Etzelmüller, B. 2011. Treeline map for Holocene Optimum, Norway. Oslo, 17.02.2011.

Farbrot, H., Isaksen, K. and Etzelmüller, B. 2008. Present and past distribution of mountain permafrost in Gaissane Mountains, Northern Norway. *In: Proceeding of the Ninth International Conference on Permafrost, Fairbanks, Alaska, June 29-July 3, 2008*, Fairbanks, Alaska, 427–432.

Farbrot, H., Hipp, T., Etzelmuller, B., Isaksen, K., Ødegård, R.S. and Humlum, O. submitted. Air and ground temperature variations observed along elevation and continentality gradients in Southern Norway. *Permafrost and Periglacial Processes*.

French, H. 2007. *The Periglacial Environment*. 3. ed, Chichester, UK: John Wiley and Sons Ltd. 458 pp.

Fukui, K., Sone, T., Yamagata, K., Otsuki, Y., Sawada, Y., Vetrova, V. and Vyatkina, M. 2008. Relationships between permafrost distribution and surface organic layers near Esso, central Kamchatka, Russian Far East. *Permafrost and Periglacial Processes* 19, 85-92.

Førland, E.J. and Hanssen-Bauer, I. 2003. Past and future climate variations in the Norwegian Arctic: overview and novel analyses. *Polar Research* 22, 113-124.

Goodrich, L.E. 1978. Some results of a numerical study of ground thermal regimes. *Proceedings, Third International Conference on Permafrost, Edmonton, Canada*, Edmonton, Canada., 30-34.

Gruber, S., Hoelzle, M. and Haeberli, W. 2004. Permafrost thaw and destabilization of Alpine rock walls in the hot summer of 2003. *Geophysical Research Letters* 31, L13504.

Gruber, S. and Haeberli, W. 2007. Permafrost in steep bedrock slopes and its temperature-related destabilization following climate change. *Journal of Geophysical Research* 112, F02S18.

Gruber, S. and Hoelzle, M. 2008. The cooling effect of coarse blocks revisited—a modeling study of a purely conductive mechanism. *In: Proceedings of the Ninth International Conference on Permafrost 2008*, Fairbanks, Alaska, USA., 557–561.

Gruber, S. and Haeberli, W. 2009. Mountain Permafrost. *In* Margesin, R. (ed). *Permafrost Soils*. Soil Biology: Springer Berlin Heidelberg, 16, 33-44.

Gubler, H., Fiddes, J., Gruber, S. and Keller, M. 2011. Scale-dependent measurement and analysis of ground surface temperature variability in alpine terrain. *The Cryosphere Discuss* 5, 307-338.

Haeberli, W. 1973. Die Basis-Temperatur der winterlichen Schneedecke als möglicher Indikator für die Verbreitung von Permafrost in den Alpen. *Zeitschrift für Gletscherkunde und Glazialgeologie* 9, 221-227.

Haeberli, W. 1992. Construction, environmental problems and natural hazards in periglacial mountain belts. *Permafrost and Periglacial Processes* 3, 111-124.

Haeberli, W., Guodong, C., Gorbunov, A. and Harris, S. 1993. Mountain permafrost and climatic change. *Permafrost and Periglacial Processes* 4, 165-174.

Haeberli, W., Wegmann, M. and Vonder Muhll, D. 1997. Slope stability problems related to glacier shrinkage and permafrost degradation in the Alps. *Eclogae Geologicae Helvetiae* 90, 407-414.

Haeberli, W., Hallet, B., Arenson, L., Elconin, R., Humlun, O., Kaab, A., Kaufmann, V., Ladanyi, B., Matsuoka, N., Springman, S. and Vonder Muhll, D. 2006. Permafrost creep and rock glacier dynamics. *Permafrost and Periglacial Processes* 17, 189-214.

Hanssen-Bauer, I. and Førland, E. 1998. Long-term trends in precipitation and temperature in the Norwegian Arctic: Can they be explained by changes in atmospheric circulation patterns? *Climate Research* 10, 143-153.

Harris, C., Davies, M. and Etzelmüller, B. 2001a. The assessment of potential geotechnical hazards associated with mountain permafrost in a warming global climate. *Permafrost and Periglacial Processes* 12, 145-156.

Harris, C., Haeberli, W., Mühll, D. and King, L. 2001b. Permafrost monitoring in the high mountains of Europe: the PACE project in its global context. *Permafrost and Periglacial Processes* 12, 3-11.

Harris, C., Vonder Mühll, D., Isaksen, K., Haeberli, W., Sollid, J.L., King, L., Holmlund, P., Dramis, F., Guglielmin, M. and Palacios, D. 2003. Warming permafrost in European mountains. *Global and Planetary Change* 39, 215-225.

Harris, C., Arenson, L., Christiansen, H., Etzelmüller, B., Frauenfelder, R., Gruber, S., Haeberli, W., Hauck, C., Hölzle, M. and Humlum, O. 2009. Permafrost and climate in Europe: Monitoring and modelling thermal, geomorphological and geotechnical responses. *Earth Science Reviews* 92, 117-171.

Harris, S. and Pedersen, D. 1998. Thermal regimes beneath coarse blocky materials. *Permafrost and Periglacial Processes* 9, 107-120.

Hasler, A., Gruber, S. and Haeberli, W. 2011. Temperature variability and thermal offset in steep alpine rock and ice faces. *The Cryosphere Discuss* 5, 721-753.

Hauck, C., Vonder Mühll, D., Russill, N. and Isaksen, K. 2000. An integrated geophysical study to map mountain permafrost: A case study from Norway.

Hauck, C., Isaksen, K., Mühll, D. and Sollid, J. 2004. Geophysical surveys designed to delineate the altitudinal limit of mountain permafrost: an example from Jotunheimen, Norway. *Permafrost and Periglacial Processes* 15, 191-205.

Heggem, E., Juliussen, H. and Etzelmüller, B. 2005. Mountain permafrost in central-eastern Norway. *Norsk Geografisk Tidsskrift-Norwegian Journal of Geography* 59, 94-108.

Heggem, E.S.E., Etzenmuller, B., Anarmaa, S., Sharkhuu, N., Goulden, C.E. and Nandinsetseg, B. 2006. Spatial distribution of ground surface temperatures and active layer depths in the Hovsgol area, northern Mongolia. *Permafrost and Periglacial Processes* 17, 357-369.

Hinzman, L., Bettez, N., Bolton, W., Chapin, F., Dyurgerov, M., Fastie, C., Griffith, B., Hollister, R., Hope, A., Huntington, H., Jensen, A., Jia, G., Jorgenson, T., Kane, D., Klein, D., Kofinas, G., Lynch, A., Lloyd, A., McGuire, A., Nelson, F., Oechel, W., Osterkamp, T., Racine, C., Romanovsky, V., Stone, R., Stow, D., Sturm, M., Tweedie, C., Vourlitis, G., Walker, M., Walker, D., Webber, P., Welker, J., Winker, K. and Yoshikawa, K. 2005. Evidence and Implications of Recent Climate Change in Northern Alaska and Other Arctic Regions. *Climatic Change* 72, 251-298.

Hipp, T. 2010. i-button stations in Norway. *EUCOP2010*, Longyearbyen, Svalbard.

Hipp, T., Etzelmüller, B., Farbrot, H. and Schuler, T. 2011. Modelling the temperature evolution of permafrost and seasonal frost in southern Norway during the 20th and 21st century. *The Cryosphere Discussions* 5, 811-854.

Hock, R. 2005. Glacier melt: a review of processes and their modelling. *Progress in Physical Geography* 29, 362-391.

Hoelzle, M. 1996. Mapping and modelling of mountain permafrost distribution in the Alps. *Norsk Geografisk Tidsskrift-Norwegian Journal of Geography* 50, 11-15.

Hofgaard, A. 2003. *Effects of climate change on the distribution and development of palsa peatlands: background and suggestions for a national monitoring project.* Trondheim. NINA Norwegian Institute for Nature Research. 32 pp.

IPCC, ed. 2007. *Climate Change 2007: Synthesis Report. Contribution of Working Groups I, II and III to the Fourth Assessment Report of the Intergovernmental Panel on Climate Change.* Ed. Core Writing Team, P., R.K and Reisinger, A. Geneva, Switzerland: IPCC.

Isaksen, K., Holmlund, P., Sollid, J. and Harris, C. 2001. Three deep alpine-permafrost boreholes in Svalbard and Scandinavia. *Permafrost and Periglacial Processes* 12, 13-25.

Isaksen, K., Hauck, C., Gudevang, E., Ødegård, R. and Sollid, J. 2002. Mountain permafrost distribution in Dovrefjell and Jotunheimen, southern Norway, based on BTS and DC resistivity tomography data. *Norsk Geografisk Tidsskrift-Norwegian Journal of Geography* 56, 122-136.

Isaksen, K., Sollid, J.L., Holmlund, P. and Harris, C. 2007. Recent warming of mountain permafrost in Svalbard and Scandinavia. *J Geophys Res* 112, F02S04.

Isaksen, K., Farbrot, H., Blikra, L., Johansen, B., Sollid, J. and Eiken, T. 2008. Five year ground surface temperature measurements in Finnmark, Northern Norway. *In: Proceedings of the Ninth International Conference on Permafrost, University of Alaska, Fairbanks, June 29-July 3, 2008,* Fairbanks, Alaska, 789–794.

Isaksen, K., Blikra Lars, H. and Eiken, T. 2011. The existence of warm permafrost in unstable rock slopes in western and northern Norway. *EGU General Assembly 2011,* Vienna, Austria 3 - 8 April 2011.

Isaksen, K., met.no. 2007. Endring i permafrost. *In* Førland, E., Amundsen, H. and Hovelsrud, G. (eds). *Utviklingen av naturulykker som følge av klimaendringer*. Oslo, Norway: CICERO, 2007/3.

Jorgenson, M. and Kreig, R. 1988. A model for mapping permafrost distribution based on landscape component maps and climatic variables. *Proceedings, Fifth International Conference on Permafrost, Trondheim, Norway,* Trondheim, Norway, 176-182.

Juliussen, H. and Humlum, O. 2007. Towards a TTOP ground temperature model for mountainous terrain in central-eastern Norway. *Permafrost and Periglacial Processes* 18, 161-184.

Juliussen, H. and Humlum, O. 2008. Thermal regime of openwork block fields on the mountains Elgåhogna and Sølen, central-eastern Norway. *Permafrost and Periglacial Processes* 19, 1-18.

Karunaratne, K. and Burn, C. 2004. Relations between air and surface temperature in discontinuous permafrost terrain near Mayo, Yukon Territory. *Canadian Journal of Earth Sciences* 41, 1437-1451.

Kattsov, V.M. and Källén, E. 2005. *Arctic climate impact assessment. Chapter 4: Future Climate Change: Modeling and Scenarios for the Arctic.* Edited by Symon, C., Arris, L. and Heal, B., Cambridge: Cambridge University Press. 1042 pp.

King, L. 1986. Zonation and ecology of high mountain permafrost in Scandinavia. *Geografiska Annaler Series A Physical Geography,* 131-139.

Klene, A., Nelson, F., Shiklomanov, N. and Hinkel, K. 2001. The N-factor in natural landscapes: variability of air and soil-surface temperatures, Kuparuk River basin, Alaska, USA. *Arctic, Antarctic, and Alpine Research* 33, 140-148.

Kudryavtsev , V.A., Kondrat'yeva, K.A., Garagulya, L.S. and Melamed, V.G. 1974. *Fundamentals of frost forecasting in geological engineering investigations.* Edited by Kudryavtsev , V.A. and Kondrat'yeva, K.A. CRREL Draft Translation 606, 1977, 489pp., Hanover, New Hampshire.: U.S. Army Cold Regions Research and Engineering Laboratory. Original edition, Osnovy Merzlotnogo prognoza pri inzhenerno-geologicheskikh issledovantyakh (in Russian). 431 pp.

Kudryavtsev , V.A., ed. 1981. *Permafrost (short edition) (in Russian)*: Moscow State University Press.

Lawrence, D.M. and Slater, A.G. 2005. A projection of severe near-surface permafrost degradation during the 21st century. *Geophysical Research Letters* 32.

Lawrence, D.M., Slater, A.G., Romanovsky, V.E. and Nicolsky, D.J. 2008. Sensitivity of a model projection of near-surface permafrost degradation to soil column depth and representation of soil organic matter. *Journal of Geophysical Research-Earth Surface* 113.

Lewkowicz, A.G. and Bonnaventure, P.P. 2011. Equivalent Elevation: A New Method to Incorporate Variable Surface Lapse Rates into Mountain Permafrost Modelling. *Permafrost and Periglacial Processes* 22, n/a.

Lied, K. and Kristensen, K. 2003. *Snøskred: håndbok om snøskred*, Nesbru: I samarbeid med NGI, Norges geotekniske institutt. 200 s. pp.

Lillesand, T.M., Kiefer, R.W. and Chipman, J.W. 2008. *Remote sensing and image interpretation*, Hoboken, N.J.: Wiley. XII, 756 s. pp.

Lilleøren, K.S., Etzelmuller, B., Gisnås, K. and Humlum, O. in prep. The relative age of mountain permafrost - estimation of Holocene permafrost limits in Norway.

Lilleøren, K.S. and Etzelmüller, B. in prep. A regional inventory of rock glaciers and ice-cored moraines in Norway. *Geografiska Annaler Series a-Physical Geography*.

Lunardini, V. 1978. Theory of n-factors and correlation of data. *In: Proceedings of the Third International Conference on Permafrost*, 40–46.

Lunardini, V. 1981. *Heat transfer in cold climates*, New York: Van Nostrand Reinhold. 731 pp.

Matthews, J.A., Berrisford, M.S., Dresser, P.Q., Nesje, A., Dahl, S.O., Bjune, A.E., Bakke, J., John, H., Birks, B., Lie, O., Dumayne-Peaty, L. and Barnett, C. 2005. Holocene glacier history of Bjornbreen and climatic reconstruction in central Jotunheimen, Norway, based on proximal glaciofluvial stream-bank mires. *Quaternary Science Reviews* 24, 67-90.

met.no. 2010. *Observasjoner fra Land* The Norwegian Meteorological Institute 2010a [Accsessed: 25.10.10 2010]. Available at http://met.no/Meteorologi/A_male_varet/Observasjoner_fra_land/.

met.no. 2010. *Klimaet i Norge* met.no 2010b [Accsessed: 12/10 2010]. Available at http://met.no/Klima/Natidsklima/?module=Articles;action=ArticleFolder.publicOpenFolder;ID=639.

met.no. 2010. *Köppens klimaklassifikasjon* met.no, 07/01/2010 2010c [Accsessed: 12/10 2010]. Available at http://metlex.met.no/wiki/K%C3%B6ppens_klimaklassifikasjon.

Mohr, M. and Tveito, O. 2008. Daily temperature and precipitation maps with 1 km resolution derived from Norwegian weather observations. *URL http://ams confex com/ams/13MontMet17AP/techprogram/paper* 141069.

Mohr, M. 2009. *Comparison of Versions 1.1 and 1.0 of Gridded Temperature and Precipitation Data for Norway*. Oslo. Norwegian Meteorological Institute. pp. 46 pp.

Nelson, F.E. and Outcalt, S.I. 1987. A Computational Method for Prediction and Regionalization of Permafrost. *Arctic and Alpine Research* 19, 279-288.

Nelson, F.E., Shiklomanov, N.I., Mueller, G.R., Hinkel, K.M., Walker, D.A. and Bockheim, J.G. 1997. Estimating active-layer thickness over a large region: Kuparuk River Basin, Alaska, USA. *Arctic and Alpine Research* 29, 367-378.

Nesje, A., Matthews, J.A., Dahl, S.O., Berrisford, M.S. and Andersson, C. 2001. Holocene glacier fluctuations of Flatebreen and winter-precipitation changes in the Jostedalsbreen region, western Norway, based on glaciolacustrine sediment records. *Holocene* 11, 267-280.

Nicolsky, D.J., Romanovsky, V.E., Alexeev, V.A. and Lawrence, D.M. 2007. Improved modeling of permafrost dynamics in a GCM land-surface scheme. *Geophysical Research Letters* 34.

Olesen, O., Brönner, J., Ebbing, J., Gellein, J., Gernigon, L., Koziel, J., Lauritsen, T., Myklebust, R., Pascal, C., Sand, M., Solheim, D. and Usov, S. 2010. New aeromagnetic and gravity compilations from Norway and adjacent areas: methods and applications. Paper read at Petroleum Geology Conference series 2010; .

Osterkamp, T.E. 2005. The recent warming of permafrost in Alaska. *Global and Planetary Change* 49, 187-202.

Overland, J.E., Wang, M. and Salo, S. 2008. The recent Arctic warm period. *Tellus A* 60, 589-597.

Pèwè, T.L. 1966. *Permafrost and its effect on life in the North*, Corvallis: Oregon State University Press. 40 s. pp.

Pomeroy, J. and Gray, D. 1995. *Snow Accumulation, Relocation and Management*. NHRI Science Report No. 7, Saskatoon, Saskatchewan.: National Hydrology Research Institute, Supply and Services Canada. 144 pp.

Pomeroy, J.W., Marsh, P. and Gray, D.M. 1997. Application of a distributed blowing snow model to the Arctic. *Hydrological Processes* 11, 1451-1464.

Riseborough, D. 2004. *Exploring the parameters of a simple model of the permafrost–climate relationship.* PhD Dissertation, Department of Geography and Environmental Studies, Carleton University, Ottawa. 330.

Riseborough, D. 2007. The effect of transient conditions on an equilibrium permafrost-climate model. *Permafrost and Periglacial Processes* 18, 21-32.

Riseborough, D., Shiklomanov, N., Etzelmüller, B., Gruber, S. and Marchenko, S. 2008. Recent advances in permafrost modelling. *Permafrost and Periglacial Processes* 19, 137-156.

Romanovsky, V.E. and Osterkamp, T.E. 1995. Interannual variations of the thermal regime of the active layer and near-surface permafrost in Northern Alaska. *Permafrost and Periglacial Processes* 6, 313-335.

Romanovsky, V.E. and Osterkamp, T.E. 1997. Thawing of the active layer on the coastal plain of the Alaskan Arctic. *Permafrost and Periglacial Processes* 8, 1-22.

Sazonova, T. and Romanovsky, V. 2003. A model for regional scale estimation of temporal and spatial variability of active layer thickness and mean annual ground temperatures. *Permafrost and Periglacial Processes* 14, 125-139.

Schuur, E.A.G., Bockheim, J., Canadell, J.G., Euskirchen, E., Field, C.B., Goryachkin, S.V., Hagemann, S., Kuhry, P., Lafleur, P.M., Lee, H., Mazhitova, G., Nelson, F.E., Rinke, A., Romanovsky, V.E., Shiklomanov, N., Tarnocai, C., Venevsky, S., Vogel, J.G. and Zimov, S.A. 2008. Vulnerability of Permafrost Carbon to Climate Change: Implications for the Global Carbon Cycle. *BioScience* 58, 701-714.

senorge.no. 2010. *Climate* Norwegian Water and Energy Directorate (NVE), Norwegian Meteorological Institute (met.no) and Norwegian Mapping Authorities (SK) 2010 [Accsessed: 12/10 2010].

Seppälä, M. 1986. The Origin of Palsas. *Geografiska Annaler Series A, Physical Geography* 68, 141-147.

Shiklomanov, N. and Nelson, F. 2003. Statistical representation of landscape-specific active-layer variability, 1039–1044.

Sigmond, E.M.O. 2002. *Geologisk kart over land- og havområder i Nord-Europa, målestokk 1:4 millioner.* Norges geologiske undersøkelse.

Smith, M.W. and Riseborough, D.W. 1996. Permafrost monitoring and detection of climate change. *Permafrost and Periglacial Processes* 7, 301-309.

Smith, M.W. and Riseborough, D.W. 2002. Climate and the limits of permafrost: a zonal analysis. *Permafrost and Periglacial Processes* 13, 1-15.

Sollid, J. and Sørbel, L. 1974. Palsa bogs at Haugtjørnin, Dovrefjell, South Norway. *Norsk Geografisk Tidsskrift-Norwegian Journal of Geography* 28, 53-60.

Sollid, J., Isaksen, K., Eiken, T. and Ødegård, R. 2003. The transition zone of mountain permafrost on Dovrefjell, southern Norway, 21–25.

Sollid, J.L., Carlson, A.B. and Torp, B. 1980. *Trollheimen - Sunndalsfjella - Oppdal. Kvartærgeologisk kart 1:100 000.* Geografisk Institutt, Universitetet i Oslo.

Sollid, J.L. and Sørbel, L. 1998. Palsa Bogs as a Climate Indicator: Examples from Dovrefjell, Southern Norway. *Ambio* 27, 287-291.

Stendel, M. and Christensen, J.H. 2002. Impact of global warming on permafrost conditions in a coupled GCM. *Geophysical Research Letters* 29.

Sturm, M., Holmgren, J., Konig, M. and Morris, K. 1997. The thermal conductivity of seasonal snow. *Journal of Glaciology* 43, 26-41.

Sushama, L., Laprise, R. and Allard, M. 2006. Modeled current and future soil thermal regime for northeast Canada. *Journal of Geophysical Research-Atmospheres* 111.

Taylor, A. 1995. *Field measurements of n-factors for natural forest areas, Mackenzie Valley, Northwest Territories.* in Current Research 1995-B, Geological Survey of Canada. 89-98 pp.

Thoresen, M.K. 1991. *Kvartærgeologisk kart over Norge, tema jordarter*. Norges geologiske undersøkelse.

Tveito, O.E., Førland, E.J., Heino, R., Hanssen-Bauer, I., Alexandersson, H., Dahlström, B., Drebs, A., Kern-Hansen, C., Jónsson, T., Laursen, E.V. and Westman, Y. 2000. *Nordic temperature maps (Nordklim)*. DNMI KLIMA Report 09/00.

Tveito, O.E. 2009. *Gridda vær- og klimadata*, from http://met.no/filestore/B3-Tveito.pdf. Oslo.

UNEP/GRID-Arendal. *Norway topography and bathymetry.* In UNEP/GRID-Arendal Maps and Graphics Library. 2001 [Accsessed: 18:26, April 26, 2011]. Available at http://maps.grida.no/go/graphic/norway_topography_and_bathymetry.

UNEP/GRID-Arendal 2007. *Permafrost extent in the Northern Hemisphere*. In UNEP/GRID-Arendal Maps and Graphics Library.

Vonder Muhll, D., Hauck, C. and Gubler, H. 2002. Mapping of mountain permafrost using geophysical methods. *Progress in Physical Geography* 26, 643.

Vorren, T.O. and Mangerud, J. 2007. Istider kommer og går. Sein-pliocen og pleistocen (kvartær); 2,7 millioner - 11 500 år. *In* Ramberg, I.B., Bryhni, I. and Nøttvedt, A. (eds). *Landet blir til Norges geologi*. Trondheim: Norsk Geologisk Forening (NGF), 2, 478-531.

Williams, P.J. and Smith, M.W. 1989. *The frozen earth: fundamentals of geocryology*, Cambridge: Cambridge University Press. xvi, 306 s. pp.

Wright, J., Duchesne, C. and Côté, M. 2003. Regional-scale permafrost mapping using the TTOP ground temperature model. *In: Permafrost: proceedings of the eighth International Conference on Permafrost, 21-25 July 2003, Zurich, Switzerland*, Lisse, 1241–1246.

Zhang, T., Heginbottom, J.A., Barry, R.G. and Brown, J. 2000. Further statistics on the distribution of permafrost and ground ice in the Northern Hemisphere. *Polar Geography* 24, 126 - 131.

Zhang, T., Barry, R.G., Knowles, K., Heginbottom, J.A. and Brown, J. 2008a. Statistics and characteristics of permafrost and ground-ice distribution in the Northern Hemisphere. *Polar Geography* 31, 47 - 68.

Zhang, Y., Chen, W.J. and Riseborough, D.W. 2008b. Transient projections of permafrost distribution in Canada during the 21st century under scenarios of climate change. *Global and Planetary Change* 60, 443-456.

11. Appendix contents

Appendix A: Publications III

A.1 Poster at EUCOP 2010 III

A.2 Oral presentation at EGU 2011 IV

Appendix B: Data for parameterization of *n*-factors VI

B.1 Litterature review of previous *n*-factor studies VI

B.2 *nF* - snow depth relation IX

B.3 Snow density data from field work 4th – 7th March 2011 X

Appendix C: Blockfield classification from satellite images XI

C.1 Landsat images used for blockfield classification XI

C.2 Matlab routine used for classification of satellite images – CD XI

C.3 Validation of blockfield map – CD XI

C.4 Blockfield map northern Norway – CD XI

C.5 Blockfield map southern Norway – CD XI

Appendix D: Maps – CD XII

D.1 *MAGT* 1961-1990, TTOP XII

D.2 *MAGT* 1971-2000, TTOP XII

D.3 *MAGT* 1981-2010, TTOP XII

D.4 *MAGT* 1981 – 2010, mKA XII

D.5 *nF*-map,1981-2010 XII

D.6 *nT*-map XII

D.7 r_k-map XII

D.8 Subsurface material map, NGU XII

D.9 Ground heat flow map, NGU XII

D.10 *AMSD* 1981-2010 (cm) XII

D.11 Difference TTOP – mKA (1981-2010) XII

D.12 Difference TTOP – mKA (version 2) (1981-2010) XII

Appendix E: Further examination of the mKA-model XIII

E.1 Difference in MAGT between the models for surface cover classes. XIII

E.2 Difference in MAGT between the models for subsurface material classes. XIV

Appendix F: The CryoGRIDeq - model routine – CD XVI

Appendix A: Publications

A.1 Poster at EUCOP 2010

Gisnås K., H. Farbrot, B. Etzelmüller & T.V. Schuler. *Regional scale mapping of permafrost distribution in Norway using the TTOP model*. Third European Conference on Permafrost 13th-17th June 2010, Svalbard. **Poster.**

Abstract and poster also available on an attached CD.

Regional scale mapping of permafrost distribution in Norway using the TTOP model

K. Gisnås, H. Farbrot, B. Etzelmüller & T.V. Schuler

Department of Geosciences, University of Oslo, Oslo, Norway

Introduction

Previous regional permafrost mapping in Norway has been based exclusively on mean annual air temperatures (*MAAT*). However, many other factors have a decisive importance for the ground temperature regime, as the distribution and duration of snow cover, vegetation and thermal properties in the active layer. The TTOP-model originally developed in Canada by *Smith & Riseborough (1996)* defines the temperature at top of the permafrost, based on annual freezing- and thawing degree days, seasonal n-factors parameterizing the vegetation and snow cover, and the conductivity ratio between frozen and thawed states in the active layer. A first implementation using the TTOP-model is now made with 1km resolution for a 100x100km area in central southern Norway.

The area has a complex topography, with alpine mountains up to 2500 m a.s.l. The regional lower limit of mountain permafrost is situated above 1400-1700 meters (east-west gradient; Etzelmüller et al. 2003), but palsas are also found at lower elevations. The model is based on operationally gridded temperature- and snow data from the period 1970-2000, provided by senorge.no.

First results

The TTOP results in this study agrees relatively well with observations. Compared to estimates based on *MAAT* only, the TTOP-model shows a better representation of the observed east-west gradient mostly due to taking the snow distribution into account. Sporadic permafrost which is absent in previous regional modelling is now reproduced, mainly resulting from the integration of sediment conductivity data. However, the varying topography introduces challenges

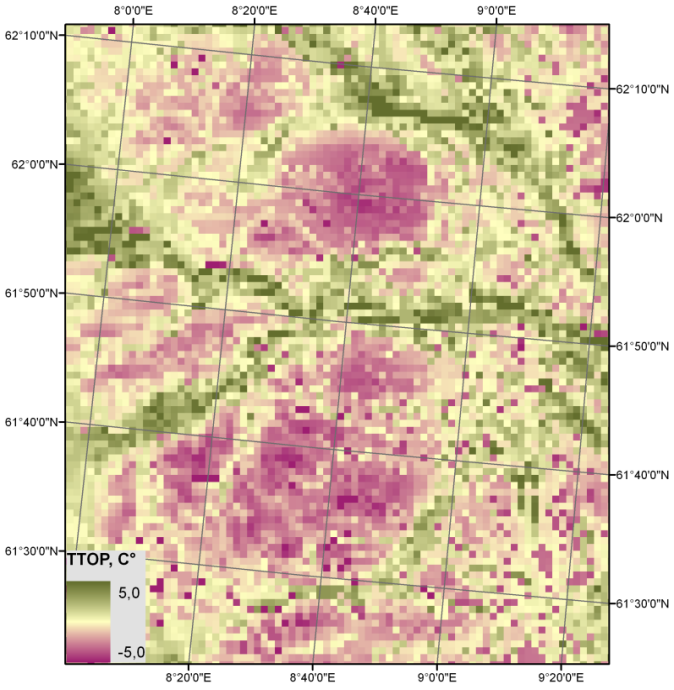

1: TTOP for an area of 100x100 km in central southern Norway.

related to snow distribution and ground thermal properties. The largest error sources are n-factors for snow (nf-factors) and the thermal regime in block field areas. Nf-factors varying with annual average snow depth are not transferable from Canada, mainly because the climatic conditions and associated snow properties are different. Nf-factors based on Norwegian measurements are currently under development. Large parts of the permafrost areas in Norway are covered by block fields. However, current available digital sediment maps do not cover block fields sufficiently well. New classifications are currently under development. Better models for the temperature regime in block fields are also necessary. Despite the above mentioned challenges the TTOP model shows promising results for simple regional scale mapping of permafrost in Norway.

References

Etzelmüller, B., Berthling, I. & Sollid, J.L. 2003. Aspects and Concepts on the Geomorphological Significance of Holocene Permafrost in Southern Norway. *Geomorphology* 52: 87-104

Smith, M., & Riseborough, D. 1996. Permafrost Monitoring and Climate Change. *Permafrost and Periglacial Processes* (7). 301-309.

A.2 Oral presentation at EGU 2011

Gisnås K., H. Farbrot, B. Etzelmüller & T.V. Schuler. *Regional scale distribution of permafrost in Norway based on two equilibrium models*. European Geoscience Union. General Assembly 2011, 3rd-8th April 2011. Vienna, Austria. **Oral presentation, presenting author K.Gisnås.**

Abstract and presentation available on an attached CD.

Regional scale distribution of permafrost in Norway based on two equilibrium models

K. Gisnås, H. Farbrot, B. Etzelmüller & T.V. Schuler

Department of Geosciences, University of Oslo, Oslo, Norway

Previous regional permafrost mapping in Norway has exclusively been based on mean annual air temperature (*MAAT*). While *MAAT* is important when considering the climatic limitations and thus macro-scale distribution of permafrost, many other factors such as the timing and thickness of the snow cover, vegetation and thermal properties in the active layer are of decisive importance when considering regional/discontinuous (meso-scale) permafrost presence. Two established equilibrium models are used to determine the permafrost distribution in mainland Norway: (1) the empirically based TTOP-model (temperature at top of permafrost), by *Smith & Riseborough (1996)*, and (2) the Kudryavtsev approach, implemented in the GIPL-model (Geophysical Institute Permafrost Laboratory, University of Alaska, Fairbanks, *Sazonova & Romanovsky* (2003)). While both models define the top of permafrost from air temperatures, the TTOP-model includes seasonal *n*-factors derived from vegetation and snow cover distribution, and the conductivity ratio between frozen and thawed states in the active layer. Correspondingly, the Kudryavtsev approach utilizes a physical parameterization of snow- and vegetation cover and the soil in the active layer.

Block fields are known to represent a negative thermal anomaly. While these features are widespread in Norway, currently available digital sediment maps do not accurately represent observed block-field distribution. Therefore, block fields have been identified from Landsat images and have been considered in the models presented above. Petro-physical data such as bedrock density and thermal conductivity have been kindly provided by the Norwegian Geological Survey. Both models are implemented at 1km resolution for mainland Norway, and forced with operationally gridded temperature and snowdepth data from the period 1960-2010, provided by Norwegian Meteorological Institute and Norwegian Water and Energy Directorate.

The model results are validated against: (1) ground surface temperature from 140 miniature temperature data loggers distributed throughout Norway; (2) vertical temperature profiles measured in 20 boreholes; and (3) maps of palsa- and rock glacier distribution. The modelled permafrost distribution agrees relatively well with observations, and reproduces regional permafrost patterns. Compared to estimates based solely on *MAAT*, both the TTOP- and GIPL-models present a more accurate representation of the observed east-west gradient due to the consideration of snowdepth . Sporadic permafrost, which was not represented in previous regional modelling, is now reproduced, due to the incorporation of sediment conductivity data. Despite these improvements, topographic variation introduces challenges related to snow distribution and ground thermal properties. The largest sources of error in the TTOP-model relate to the freezing factors (n_f) for snow and the thermal regime in block field areas which is controlled by both convective and conductive heat transfer.

Sazonova, T and Romanovsky, V. 2003. A model for regional scale estimation of temporal and spatial variability of active layer thickness and mean annual ground temperatures. *Permafrost and Periglacial Processes* 14, 125-139.

Smith, M., & Riseborough, D. 1996. Permafrost Monitoring and Climate Change. *Permafrost and Periglacial Processes* (7). 301-301.

Appendix B: Data for parameterization of *n*-factors

B.1 Litterature review of previous *n*-factor studies

Forest type	*nT*	*nF*	Location	Reference
Mixed birch-spruce	0,85	0,35	Fairbanks	Jorgenson & Kreig 1978
Closed aspen	1	0,3	Fairbanks	Jorgenson & Kreig 1978
Closed birch	0,9	0,35	Fairbanks	Jorgenson & Kreig 1978
Closed white spruce	0,9	0,35	Fairbanks	Jorgenson & Kreig 1978
Open black spruce	0,6	0,3	Fairbanks	Jorgenson & Kreig 1978
Closed black spruce	0,5	0,3	Fairbanks	Jorgenson & Kreig 1978
Tall spruce, birch, hardwoods	0,59	0,31	Ochre River	Taylor 1995
Aspen, spruce, hardwood & feathermoss	0,61	0,41	Manners Creek	Taylor 1995
Upland hardwood, spruce	0,3	0,2	Wrigley Hwy	Taylor 1995
Upland spruce, hardwoods	0,64	0,3	Ochre River	Taylor 1995
Open spruce with hardwoods	0,42	0,23	Saline River	Taylor 1995
Tall open hardwood, spruce	0,44	0,36	River Between Twp Mtns	Taylor 1995
Open spruce hardwoods	0,55	0,3	Mountain River	Taylor 1995
Open black spruce hardwoods	0,34	0,13	Norman Wells	Taylor 1995
Open black spruce hardwoods	0,34	0,28	Norman Wells	Taylor 1995
Open spruce, hardwood	0,74	0,48	Willowlake River	Taylor 1995

Open mixed w/ willow thickets	0,38	0,32	Francis Creek	Taylor 1995
Open upland hardwood	0,59	0,37	Manners Creek	Taylor 1995
Aspen grove	0,72	0,28	Saline River	Taylor 1995
Spruce/feathermoss	0,66	0,43	Martin River	Taylor 1995
Larch	0,33	0,44	Norman Wells	Taylor 1995
Closed white spruce	-	0,54	Takhini Valley	Karunaratne & Burn 2003
Mature white spruce	0,82	0,51	Mayo	Karunaratne & Burn 2004
Birch and spruce	0,75	0,24	Mayo	Karunaratne & Burn 2004
Mature poplar & spruce	-	0,22	Mayo	Karunaratne & Burn 2004
Mature spruce	0,91	0,37	Mayo	Karunaratne & Burn 2004

Vegetated	***nT***	***nF***	**Location**	**Reference**
Grassland (meadow)	-	0,47	Takhini Valley	Karunaratne & Burn 2003
Mixed willows	1,07	0,15	Mayo	Karunaratne & Burn 2004
Low shrubland 1	0,97	-	North slope Alaska	Klene et al. 2001
Low shrubland 2	0,73	-	North slope Alaska	Klene et al. 2001
Grassy area	0,72	0,13	Norman Wells	Taylor 1995
Low shrub scrub	0,85	0,30	Fairbanks	Jorgenson & Kreig 1978

Barren ground	*nT*	Location	Reference
Barren ground	1,25	North slope, Alaska	Klene et al. 2001
Moist tundra (acidic)	0,81	North slope, Alaska	Klene et al. 2001
Moist tundra (non-acidic)	0,95	North slope, Alaska	Klene et al. 2001
Wet tundra 1	1,00	North slope, Alaska	Klene et al. 2001
Wet tundra 2	0,92	North slope, Alaska	Klene et al. 2001

Organic	*nT*	*nF*	Location	Reference
Tussock bog	0,90	0,30	Fairbanks, Alaska	Jorgenson & Kreig 1978
Small bog	0,66	0,12	Wrigley Hwy MRV	Taylor 1995
Fen	0,26	0,29	River Between Two Mtns, MRV	Taylor 1995
Fen	0,80	0,12	Ochre River, MRV	Taylor 1995

B.2 *nF* - snow depth relation

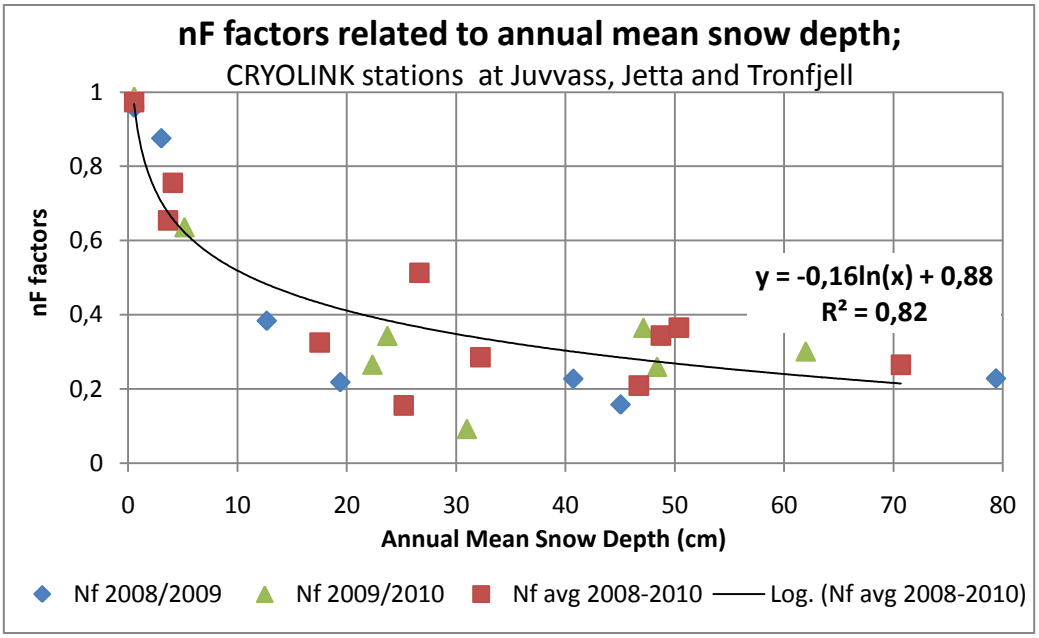

Figure 33: nF-snow depth relation developed from CRYOLINK i-button and air/ground stations.

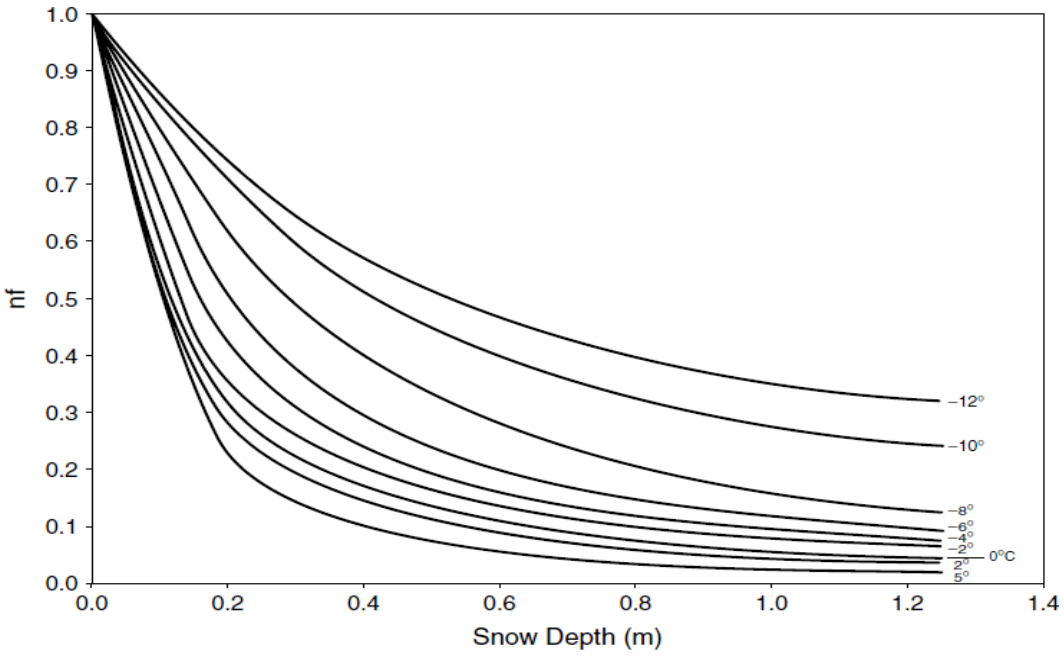

Figure 34: nF-snow depth relation developed from numerical simulations by Smith and Riseborough(2002).

B.3 Snow density data from field work 4th – 7th March 2011

Table 17: Average snow densities and snow depths measured during the CRYOLINK foeld work 4th to 7th of March 2011. The data are used to relate nF-factors to snow water equivalent.

Site	Date	Station ID	Avg snow density (kg m^{-3})	Snow depth (cm)
Tronfjell	4. March 2011	Tron-LB2	324	35-45
		Tron-LB3	---	0
		Tron-LB4	345	35
		Tron-LB5	344	50-60
		Tron-LB6	330	35-45
Juvvass	6. March 2011	Juv-LB1	390	20
		Juv-LB2	382	85-105
		Juv-LB4	350	10
		Juv-LB5	388	95
		Juv-LB6	310	10
Jetta	7. March 2011	Jetta-LB1	407	45
		Jetta-LB2	402	150
		Jetta-LB3	---	0

Appendix C: Blockfield classification from satellite images

C.1 Landsat images used for blockfield classification

Satellite scenes
L4200018_01819900719
L5192010_01020100726
L5194010_01020090806
L5194011_01120060729
L5195011_01120040730
L5196010_01020060828
L5196011_01120060727
L5196012_01220100908
L5197011_01120090912
L5198016_01620100906
L5198017_01720090919
L5199016_01620030809
L5199017_01720030809
L5199018_01820030809
L5199019_01920060716
L5200016_01620100904
L5200017_01720100904
L5201017_01720100927

C.2 Matlab routine used for classification of satellite images – CD

Run file: RUN_classification.m

C.3 Validation of blockfield map – CD

The map shows the 99 validation points in yellow, and the digitized blockfield areas in pink. Areas classified as blockfields are in green. The blockfield classification is at 240 meter resolution.

C.4 Blockfield map northern Norway – CD

C.5 Blockfield map southern Norway – CD

Appendix D: Maps – included on the CD

D.1 *MAGT* 1961-1990, TTOP

D.2 *MAGT* 1971-2000, TTOP

D.3 *MAGT* 1981-2010, TTOP

D.4 *MAGT* 1981 – 2010, mKA

D.5 *nF*-map,1981-2010

D.6 *nT*-map

D.7 r_k-map

D.8 Subsurface material map, NGU

D.9 Ground heat flow map, NGU

D.10 *AMSD* 1981-2010 (cm)

D.11 Difference TTOP – mKA (1981-2010)

D.12 Difference TTOP – mKA (version 2) (1981-2010)

Appendix E: Further examination of the mKA-model

E.1 Difference in MAGT between the models for surface cover classes.

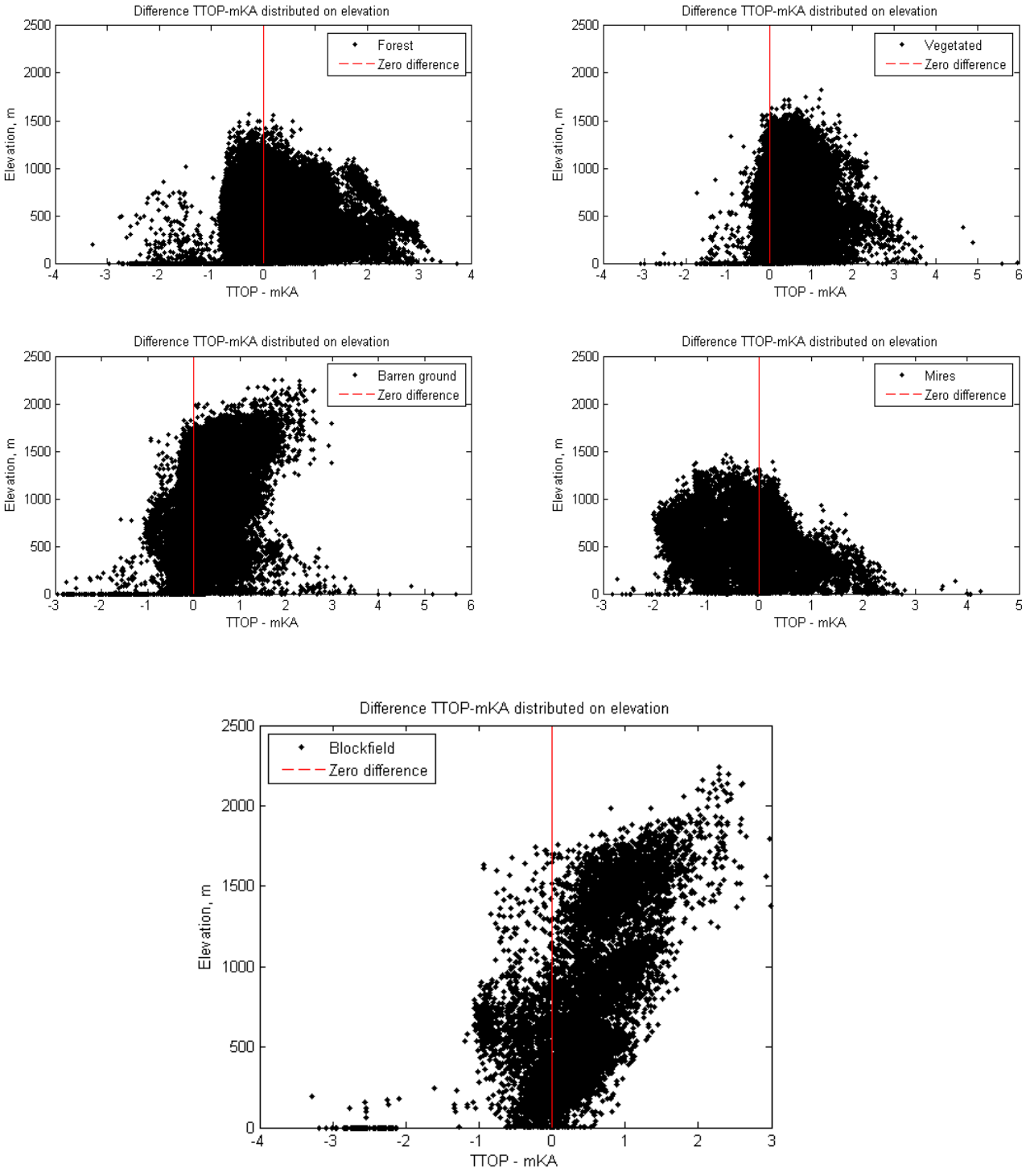

Figure 35: The plots show the difference in MAGT between the two models distributed on altitude. Each surface cover class is plotted individually.

E.2 Difference in MAGT between the models for subsurface material classes.

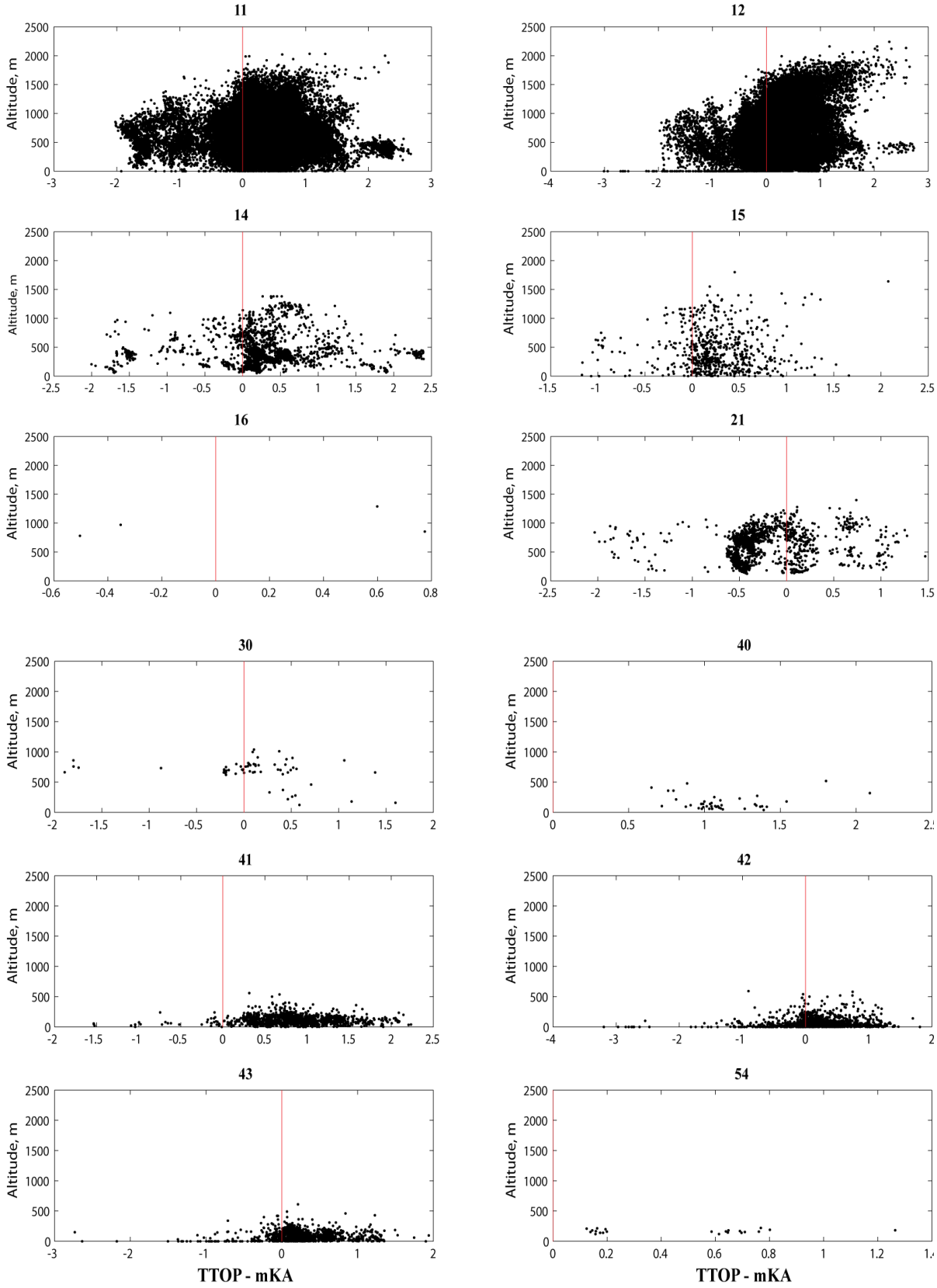

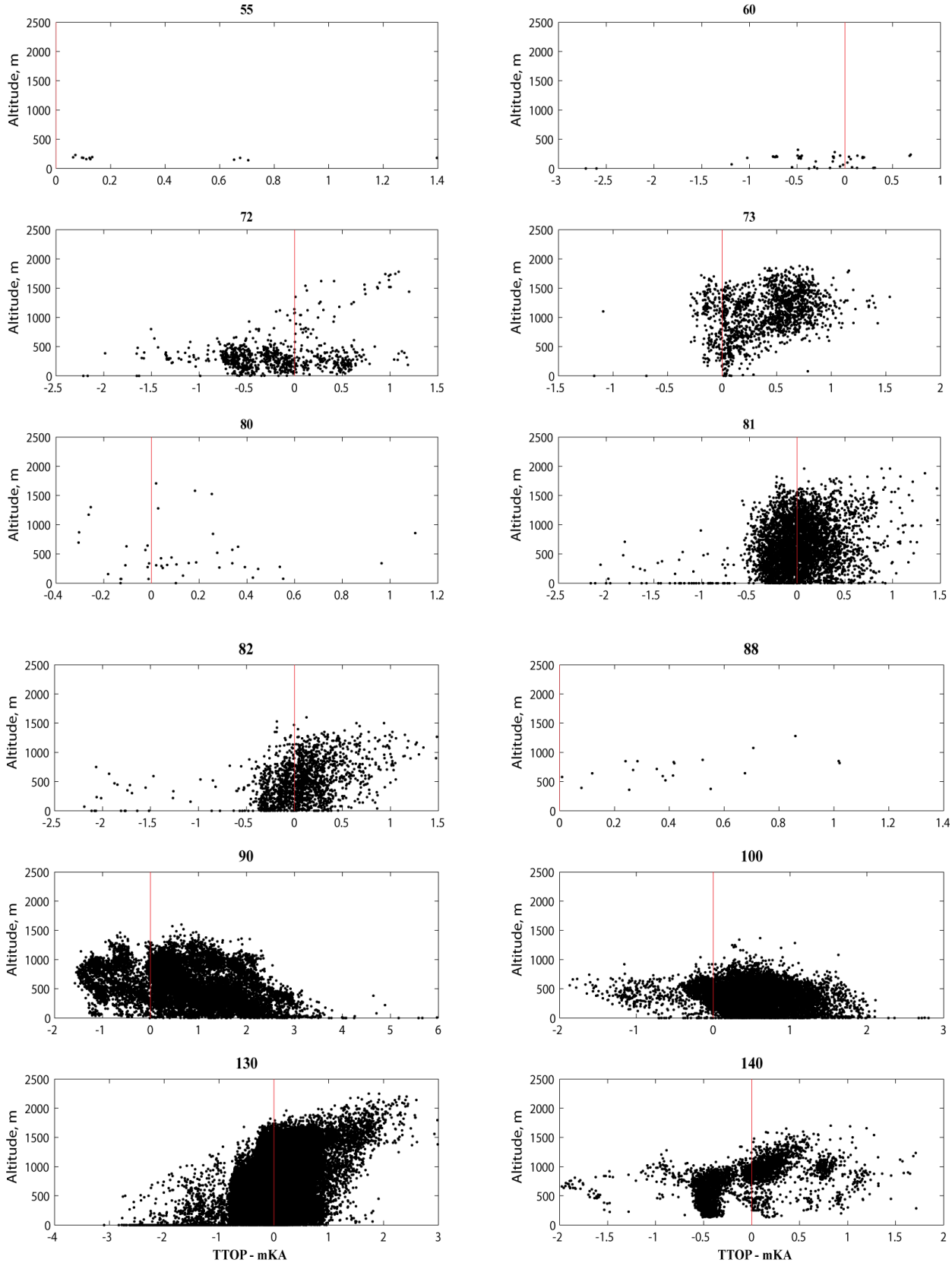

Figure 36: Difference in MAGT between the two models is distributed on altitude and subsurface material class. The plots are numbered with respect to subsurface material classes from Table 4.

Appendix F: The CryoGRIDeq - model routine – CD

The model run is scripted in MATLAB, and a graphical user interface (GUI) can be opened by typing **CryoGRIDeq** in the MATLAB command window.

Select model: The TTOP-model can be run for all three scenarios; while the mKA-model can only be run with historical and present data.

Select model run:

- **Present model run for the period 1957 - 2010.**

  This run requires admission to the Cryolink server, and that the //terra/felles-server is mapped as K:. The model run is computationally demanding, and requires long processing time. One year of the TTOP-model takes approximately 11min on a fast computer. The mKA-model takes approximately 16min.

- **Holocene reconstruction (0 - 10 000 B.P.)**
  The Holocene run is in intervals of 250 years since 10 000 years B.P. The processing time is less than 30 sek.
- **Future model run (2071 - 2100)**
  The future model run is available for the period 2071-2100. The processing time is approximately 2min.

Export and plot maps: Select the maps you want to export or plot as a MATLAB figure. Exported maps are saved as text-files to a subfolder of the "Output"-folder, named by date and time. All maps are saved in the UTM33 coordinate system. MATLAB-figures pop up automatically, and the colorbar can be adjusted as desired.

Validation with boreholes should be done for the last normal period, while validation with MAGST from MTD-loggers should be done for 2007-2009, which is the period of data collection.

Statistics: Total permafrost area is given in km^2 in addition to permafrost distributed on subsurface material classes. These are given as codes for each class, according to Table 4.

Most of the input data to the models are saved as mat-files to decrease the processing time. The scripts for parameterization of *nT* (find_nt.m), diffusivity and height of vegetation, and

soil property data (soil_properties.m) are included in the folder “Other functions”, but are not run from the CryoGRIDeq-GUI (class_veg.m). Input maps are included in the folder Input.